NAZARBAYEV UNIVERSITY

Modification of nanomaterials with Intense Pulsed Ion Beams for photocatalytic applications

A thesis presented

by

Alshyn Abduvalov, MSc

to

The School of Sciences and Humanities

in partial fulfillment of the requirements

for the degree of

Doctor of Philosophy in Physics

Nazarbayev University

Astana, Kazakhstan

December 2023

Acknowledgments

I would like to express my truthful gratitude to the individuals who have played a critical role in the successful completion of my doctoral research work.

First and foremost, I am deeply thankful to my supervisor, Prof. Alexander Tikhonov, for his solid guidance, helpful insights, and continuous care throughout this research journey. His mentorship has been influential in shaping the direction of my work and has enriched my understanding of the subject matter.

I am similarly grateful to my co-supervisor, Prof. Timur Atabaev, whose expertise and thoughtful feedback have significantly contributed to the depth and rigor of this thesis and manuscripts I published. His commitment to academic excellence and encouragement have been a constant source of motivation.

My heartfelt thanks extend to my co-author, Prof. Marat Kaikanov. Collaborating with you has been a rewarding experience, and I appreciate the shared dedication to advancing our research. Your contributions have enhanced the quality and impact of our collective work.

I would like to express my deepest appreciation to my family for their untiring support, understanding, and encouragement throughout this challenging yet fulfilling academic journey. Their love and belief in my capabilities have been a driving force, and I am truly grateful for the sacrifices they have made to make this endeavor possible.

Finally, I extend my gratitude to all my friends and colleagues, who have been a foundation of inspiration, enthusiasm, and solidarity. Your intellectual debates and shared experiences have improved my academic and personal growth.

Abstract

The world energy problem has been facing harsh challenges in the last few decades due to the increase in energy consumption of the growing world population and decreasing reserves of traditional carbon-based energy resources. Photoelectrochemistry (PEC) based solar water splitting is one of the potential paths for transforming renewable solar energy into green hydrogen fuel to meet energy expectations. In PEC water splitting, hydrogen is generated using semiconductor materials that can absorb sunlight and decompose water molecules into hydrogen and oxygen gases. *Fabrication of highly effective, stable, and economically viable semiconductor photoelectrode materials, to increase their performance, and enhancing their photocatalytic activity has been proved to be a vital task for PEC solar water decomposition.*

Among all the suitable materials, WO_3 has been reputed as a promising photoelectrode in the last decade due to the many criteria that it fits. The main current problems in WO_3, based PEC water splitting systems are their low *solar to hydrogen* efficiencies and poor photocatalytic properties. Developing and applying new methods of surface modifications and engineering are favorable strategies to enhance photocatalytic properties of WO_3.

This thesis work is devoted to the study of surface modification of WO_3 photoelectrodes with intense pulsed ion beam (IPIB) irradiation for photocatalytic properties enhancement and studying the effect of IPIB irradiation on solid state dewetting shape formation of plasmonic Ag nanoparticles (NPs). The thesis also reports strategies of combining plasmonic nanoparticles and downshifting photoluminescent NPs with WO_3.

IPIB irradiation is a method for modification of surfaces of materials with few hundreds keV energetic ions that penetrate deep into 1-2 micrometers.

The outcomes of experiments show that surface engineering of WO_3 photoelectrode with IPIB can enhance its photocatalytic properties and promote charge-carrier characteristics. The IPIB also gives opportunity to study shape formations of silver NPs and results exhibit huge influence of super-fast annealing on sphericity of the silver NPs. Simultaneous use of plasmonic NPs and fluorescent materials also proven to be effective method of photoactivity enhancement of WO_3 thin films.

In **Chapter 1,** the current situation in energy perspectives as well as future energy problems are discussed. Energy shortage resulting from a scarcity of traditional fossil resources and caused by an increase in global population and increased energy consumption is considered and potential

solutions to close that by using solar energy are identified. Additionally, the chapter gives insight into the current state of synthesis of solar-generated hydrogen.

In **Chapter 2**, the text is devoted to discussion of theoretical concepts of PEC solar water splitting and photoactivity of photoelectrodes, working principles of three electrode cells and role of plasmonic NPs in photoactivity enhancement. Additionally, operational principles of the accelerator for IPIB irradiation are broadly discussed. In addition to discussing the most recent developments in the synthesis of new composite materials and compositions of WO_3, other tactics for improving photocatalytic performance of photoelectrodes are also covered.

In **Chapter 3**, experimental equipment and modification tools used in current work are reviewed. Mostly used techniques for examining photoelectrode performance and various types of efficiency measurements are also considered in this chapter.

In **Chapter 4**, magnetron sputtered double-layered WO_3 photoelectrode is modified with IPIB irradiation to increase its photocatalytic property. Irradiation effect on morphology and induced sponge-like microstructure of WO_3 with increased absorbance are investigated.

In **Chapter 5**, shape formation of plasmonic Ag NPs on fused silica are examined after irradiating with IPIB. Creation of NPs with more sphericity because of super-fast heating and cooling is broadly reviewed in terms of ion beam current density, number of ion beam pulses, and substrate roughness.

In **Chapter 6**, a new composite material consisting of WO_3 photoelectrode combined with Au NPs, and down conversion $Y_2O_3:Eu^{3+}$ NPs is obtained and examined for PEC performance. Main reasons of light trapping mechanism as well as light absorbance enhancement is thoroughly investigated.

The **Chapter 7** covers the case when WO_3 thin film without FTO substrate irradiated with IPIB. Decreasing substrate effect gives more information how the pulsed intense ion beam influences the structural and morphological properties of thin WO_3 films on TEM membranes.

Contents

List of Abbreviations

AC	Alternating Current
AFM	Atomic Force Microscopy
ALD	Atomic Layer Deposition
CVD	Chemical Vapor Deposition
CB	Conduction Band
CE	Counter Electrode
DC	Direct Current
EIS	Electrochemical Impedance Spectroscopy
FIB	Focused Ion Beam
GIXRD	Grazing Incidence X-Ray Diffraction
GLAD	Glancing angle deposition
HER	Hydrogen evolution reaction
HRTEM	High Resolution Transmission Electron Microscopy
IPIB	Intense Pulsed Ion Beam
LSV	Linear Sweep Voltammetry

NPs	Nanoparticles
NSs	Nanostructures
NHE	Normal Hydrogen Electrode
MOS	Metal Oxide Semiconductor
MS	Magnetron sputtering
OER	Oxygen evolution reaction
PEC	Photoelectrochemistry
PLD	Pulsed laser deposition
PVD	Physical Vapor Deposition
RPM	Revolutions Per Minute
RE	Reference Electrode
RHE	Reversible Hydrogen Electrode
RTA	Rapid Thermal Annealing
SEM	Scanning Electron Microscopy
STH	Solar to hydrogen
TEM	Transmission Electron Microscopy
VB	Valence Band
WE	Working Electrode
XPS	X-Ray Photoemission Spectroscopy
XRD	X-Ray Diffraction

List of Figures

List of Tables

1. Introduction

1.1 Global energy overview and solar energy utilization

Global energy overview. Energy is the most essential resource for sustaining human life on Earth. The breakthroughs in science, technology, medicine, and industry within the last century resulted in an increase of human life quality and led to population growth on Earth. Those advancements in life standards are often accompanied by increased demand for energy. Such rapid rise in energy requirements and consequent growth in supply lead to the depletion of existing oil and gas reserves of the world and seeking an alternate route for energy production.

There is another effect from carbon-based energy sources: pollution. Fossil fuel based traditional energy sources are the main causes of greenhouse gas emissions in the world. They rapidly increase air pollution by worsening air quality. The greenhouse effect arising from greenhouse gas emissions has an enormous impact on global climate change (Santos et al., 2022). It causes temperature increase on Earth by preventing reflection of solar energy. Carbon dioxide (CO_2) gas, that is produced from burning fossil fuels, traps solar energy in the atmosphere by contributing to the planet's heating. Vehicles, planes, and ships involved in manufacturing, logistics, air transportation, and waterways are big contributors of the greenhouse effect as well as city heating systems. There is a consonance between rise of global average surface temperature and increase in fossil fuel consumption of the world (Al-Ghussain, 2019; Hannah Ritchie et al., 2022; Hansen et al., 2006). In 2020, world fossil fuel consumption is estimated as 128,800 TWh as seen in Figure 1.1. It is much higher compared to a century ago (10,955 TWh in 1920). Air pollution, water contamination, and lessening of flora and fauna are the major challenges caused by fossil fuel-based power .

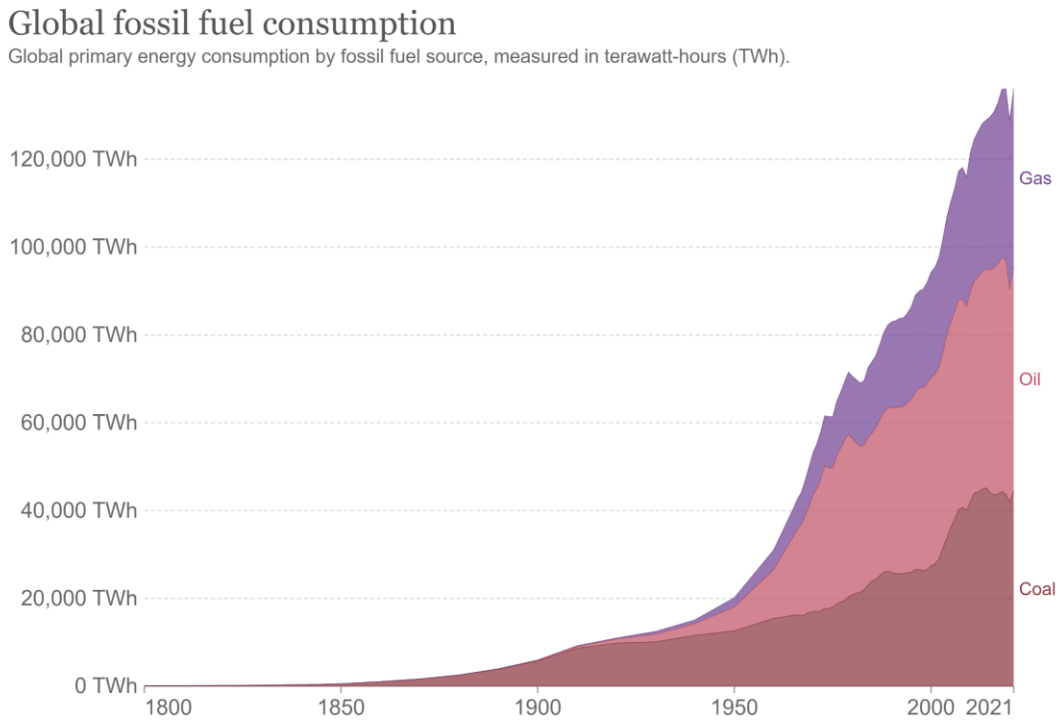

Figure 1.1. Global fossil fuel consumption. The figure is adapted from (Hannah Ritchie et al., 2022).

To solve the above-mentioned major issues, world countries have signed agreements and launched common activities to decrease global average temperature by shifting to renewable sources of energies, etc. (Agreement, 2015; Crowley-Vigneau et al., 2023).

Renewable energy sources include hydropower, wind, tides, geothermal, and solar, etc. have promising potential to meet discussed expectations in energy consumption within the foreseeable future (Uğurlu, 2022). Hydropower production is the conversion of potential energy stored in running water into electricity (Wagner & Mathur, 2011). Wind power generation is energy production in the form of electricity from wind turbines (Nazir et al., 2020). The tidal energy is an everlasting source obtained by the movement of tides in oceans, seas, and rivers resulting from the centrifugal and gravitational interactions of the Earth, Moon and the Sun (Shetty & Priyam, 2022). An increasing heat gradient towards the Earth center and release of this heat to the surface via natural underground water lines allows the production of geothermal energy (Stober & Bucher, 2021). Solar energy, as the name indicates, energy obtained from the Sun (Hayat et al., 2019). It is broadly studied, and new technologies based on that are being developed. World strategies to mitigate CO_2 emission induce increasing interest in research on alternating energy sources mentioned previously. Most of those renewable energy sources have been

commercialized and demonstrate increasing market share in energy supply in recent years (L. Li et al., 2022). It can be seen from Figure 1.2 that renewable energy consumption shows rapid increase in the last century (Hannah Ritchie et al., 2022).

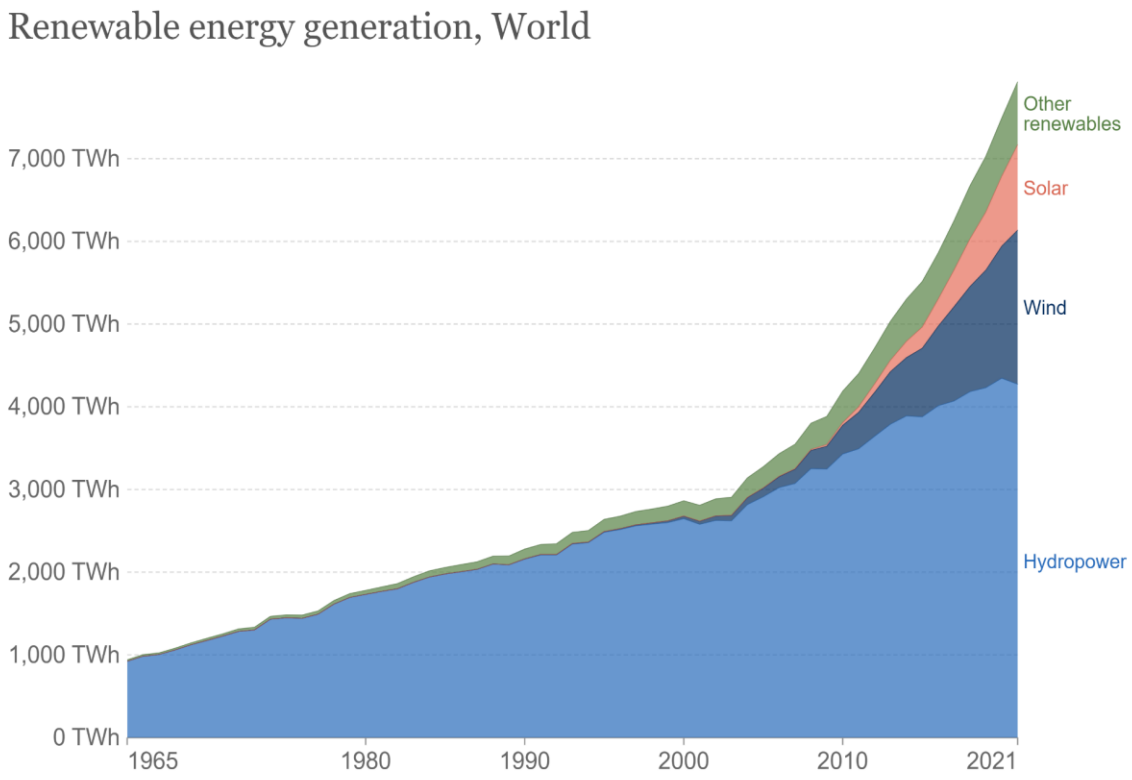

Figure 1.2. Global renewable energy consumption. The figure is adapted from (Hannah Ritchie et al., 2022).

Solar energy utilization. The Sun has a paramount amount of energy for the entire ecosystem on earth to exist. Capturing and storing the sun's energy are fundamental steps for the replacement of conventional power resources.

The energy that the sun generates may be captured in a variety of ways. Firstly, using solar photovoltaic cells, it is possible to generate energy from sunshine. High efficiency of contemporary solar cells made them possible to employ in large scale commercial industry. Despite such progress in solar cells, other approaches for solar energy collection are being developed.

Secondly, using mirrors or lenses to focus sunlight onto a specific region to create heat that may be converted into energy is known as concentrated solar power. Another type, solar water heating is the process of heating water for usage in houses and other structures using solar panels.

Thirdly, solar energy can be collected by semiconductor thin films or powders to help split water and generate hydrogen or oxygen gas; to eliminate organic wastes such as dye, pesticides, etc. Solar water splitting is one of the potential clean types of hydrogen fuel generation.

1.2 The solar hydrogen generation

The hydrogen generation. Hydrogen is high quality fuel that may create and transfer heat and energy. It shows huge potential to be used instead of all other energy sources. However, it is limited due to complicated and expensive production processes (Abohamzeh et al., 2021). Additionally, storing and transporting hydrogen fuel are big issues due to high safety requirements (Abohamzeh et al., 2021). It shows low ignition energy and high flame velocity as well as fast diffusion property (Abohamzeh et al., 2021). Considering energy production performance, hydrogen shows the uppermost energy producing per unit mass (Akal et al., 2020; Gupta, 2008; Hassanpouryouzband et al., 2020). To deal with above mentioned major challenges, the production process should be well controlled, and costs should be decreased.

Currently, industry hydrogen production is carried out by burning petrochemical products and using the process of water electrolysis. However, producing hydrogen in such a way does not fulfill expectations in global air pollution. Instead, it is viable to use alternative methods with less damage to the environment. Hydrogen which is produced using renewable energy is called green hydrogen. Green hydrogen production encompasses the techniques where alternative energy sources such as geothermal, wind and solar are used to produce hydrogen. Such productions are still under development and has not been considered yet as a potential option for widespread industrial applications (Ayodele et al., 2020; Raka et al., 2020).

The solar hydrogen producing methods. Currently, in the laboratory environment, hydrogen production is being developed using various above-mentioned renewable energy sources including sunlight. Hydrogen can be produced by photoelectrochemical (PEC), photochemical (PC), and photovoltaic – electrolysis (PV + E) techniques as seen in Figure 1.3.

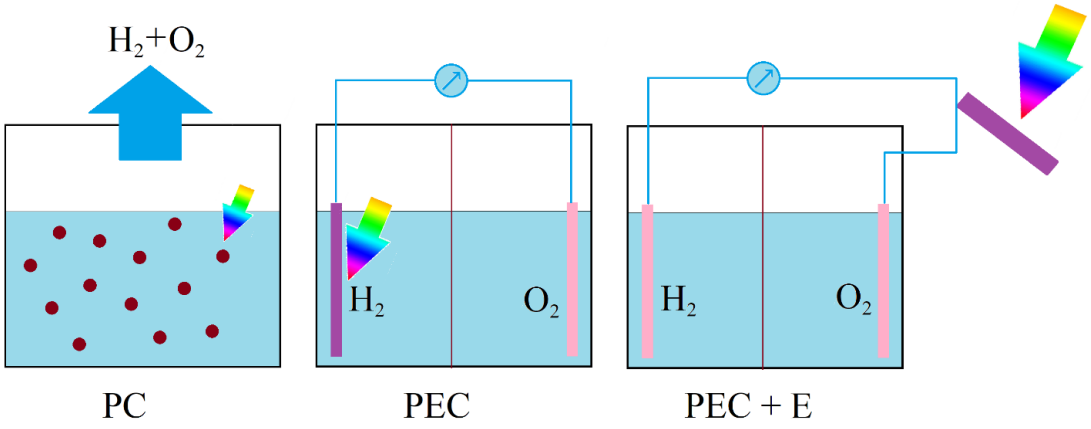

Figure 1.3. Schematic design of solar hydrogen production methods.

In the PC method, water reduction and oxidation take place in a single photocatalytic material. This material should possess good stability against photodegradation, should have an appropriate narrow band gap and suitable band alignment with water redox potentials for the prevention of electrons and holes from recombining. In the literature, PC systems are considered to be one-step photoexcitation systems, while PEC is a two-step system or Z-scheme due to the involvement of two different photocatalytic materials (Bin Adnan et al., 2018).

The PEC water splitting is a method where a semiconductor material absorbs solar light and consequently generates electron-hole pairs to oxidize or reduce water. Hydrogen production in PEC allows easy separation of generated gases due to its suitable configuration. Such water decomposition via photocatalysis using three-electrode cells was firstly reported by Akira Fujishima and Kenichi Honda in 1972, in their work devoted to study PEC properties of TiO_2 (Fujishima & Honda, 1972). Since then, many good photocatalyst materials have been discovered and developed. They offer a cheap and clean way of producing hydrogen fuel. However, PEC water splitting is far away from being used on a commercial scale due to low solar to hydrogen (STH) efficiency. It was predicted that if STH efficiency surpasses 10 % estimation, solar hydrogen generation might be a robust competitor of solar cells in commercial renewable energy enterprises (Sankir, N. D & Sankir, M. (Eds.), 2018).

The current state of semiconductor photoelectrode preparation for solar hydrogen generation requires further development. Up to now, many strategies have been implemented: surface engineering, making composite materials, creating heterostructures, and doped nanomaterial preparation, etc. Surface engineering includes several surface treatments to modify nanomaterial surfaces. Implementation of modifications with ion beam irradiation and plasmonic nanoparticles in this thesis work are well known surface treatments for PEC photoelectrodes to enhance

photocatalytic efficiency. The PEC water splitting process can be facilitated using various catalytic strategies and co-catalysts.

1.3 Thesis scopes: key objectives and novelty

The main tasks of the thesis work:

1. Synthesis and optimization of the WO_3 photoelectrode for PEC applications.
2. Implementing surface engineering by means of ion beam irradiation to WO_3 photoelectrodes to boost photocatalytic activity. Developing strategies to successfully use pulsed ion beam irradiation to modify WO_3 photoelectrodes.
3. Studying pulsed ion beam irradiation induced noble metal thin films solid state dewetting.
4. Developing new strategies for photocatalytic enhancement of WO_3 photoelectrode using plasmonic nanoparticles and downconversion materials.
5. Defect generation studies in WO_3 thin films without substrate as result of pulsed ion beam irradiation.

The novelty of the thesis work:

1. Crystalline WO_3 thin films successfully synthesized with magnetron sputtering method by optimizing deposition parameters and annealing conditions (thickness, oxygen partial pressure, deposition power, annealing environment, and temperature) for further usage in PEC photocatalysis.
2. Investigation of the effect of intense pulsed ion beam irradiation on morphology, PEC activity and crystalline structure of amorphous and crystalline WO_3 thin films.
3. Development of new strategy for PEC enhancement of double-layer architecture WO_3 thin films photoanodes with IPIB irradiation.
4. Studying generation of plasmonic nanoparticles by solid state dewetting induced by intense pulsed ion beam irradiation.
5. Developing light management strategies for PEC enhancement of WO_3 using plasmonic nanoparticles and photoluminescent materials.
6. Studying the intense pulsed ion beam irradiation effect on the WO_3 thin films with decreased substrate effect.

Thesis outputs.

Journal papers:

1. **Abduvalov,** A.; Kaikanov, M.; Atabaev, T.S.; Tikhonov, A. Improving Photoelectrochemical Activity of Magnetron-Sputtered Double-Layer Tungsten Trioxide Photoanodes by Irradiation with Intense Pulsed Ion Beams. *Nanomaterials* **2022**, *12*, 2639. https://doi.org/10.3390/nano12152639. **(IF 5.7).**
2. **Alshyn Abduvalov**, Marat Kaikanov, and Alexander Tikhonov. Solid-State Dewetting of Thin Silver Films into Spherical Nanoparticles under High-Current Pulsed Ion Beam Irradiation. *ACS Omega* **2023** *8* (35), 31954-31961. DOI: 10.1021/acsomega.3c03743. **(IF 4.132).**
3. **Alshyn Abduvalov**, Kamila Zhumanova, Marat Kaikanov, Timur Atabaev, and Alexander Tikhonov. The photoactivity enhancement of WO3 photoanodes using combined effect of plasmonic Au and photoluminescent Eu^{3+} doped Y_2O_3 NPs. **(Submitted).**
4. Kaikanov, M., Nauruzbayev, D., **Abduvalov, A.,** & Baigarin, K. (2023). Investigation of intense pulsed ion beam generation by a magnetically insulated ion diode at a reduced impedance. Vacuum, 217, 112496. https://doi.org/10.1016/j.vacuum.2023.112496. **(IF 4.11).**
5. M Kaikanov, **A Abduvalov**. Improvement of Conductivity and Adhesion of AgNW Flexible Transparent Conductive Coatings by the Capillary Forces Effect and Polyvinyl Alcohol. Advanced Electronic Materials, 2024, 2300876. **(IF 6.2).**

2. WO_3 thin films as photoelectrode materials for PEC photocatalysis and their modifications intense pulsed ion beam and plasmonic nanoparticles.

2.1 PEC water decomposition.

2.1.1 Theoretical concept.

PEC as a concept involves electrochemical processes triggered by solar light. Those processes occur as a result of absorbance of light by photoelectrode material, when electrons undergo excitation from normally occupied levels to higher energy states by absorbing light photons. Some portion of absorbed energy might be transferred into lattice vibrations in the form of heat due to strong interaction between electrons themselves with lattice ions. Materials band gap defines absorbent photon energy.

Electrochemical water splitting is a process in which water molecules can be decomposed by semiconductor material as a result of solar light absorption. Solar energy absorption provokes generation of electron-hole pairs inside the semiconductor material. Generated charge carriers diffuse through the semiconductor material and reach the semiconductor surface/interface to run chemical processes. Depending on the material's nature of being p or n type, holes or electrons separate and move to the surface of photoelectrode to oxidize or reduce water.

In our work, we use three electrode PEC cells which are composed of a working electrode (semiconductor), Pt as a counter electrode, and reference electrode. Such configuration of cells

for studying PEC water splitting was firstly offered by Fujishima and Honda (Fujishima & Honda, 1972). It is suitable for driving oxygen or hydrogen evolution half-reactions on separate interfaces. Schematic illustration for n type material is given in Figure 2.1. There are other configurations where two half reactions may occur at two sides of the same semiconductor material.

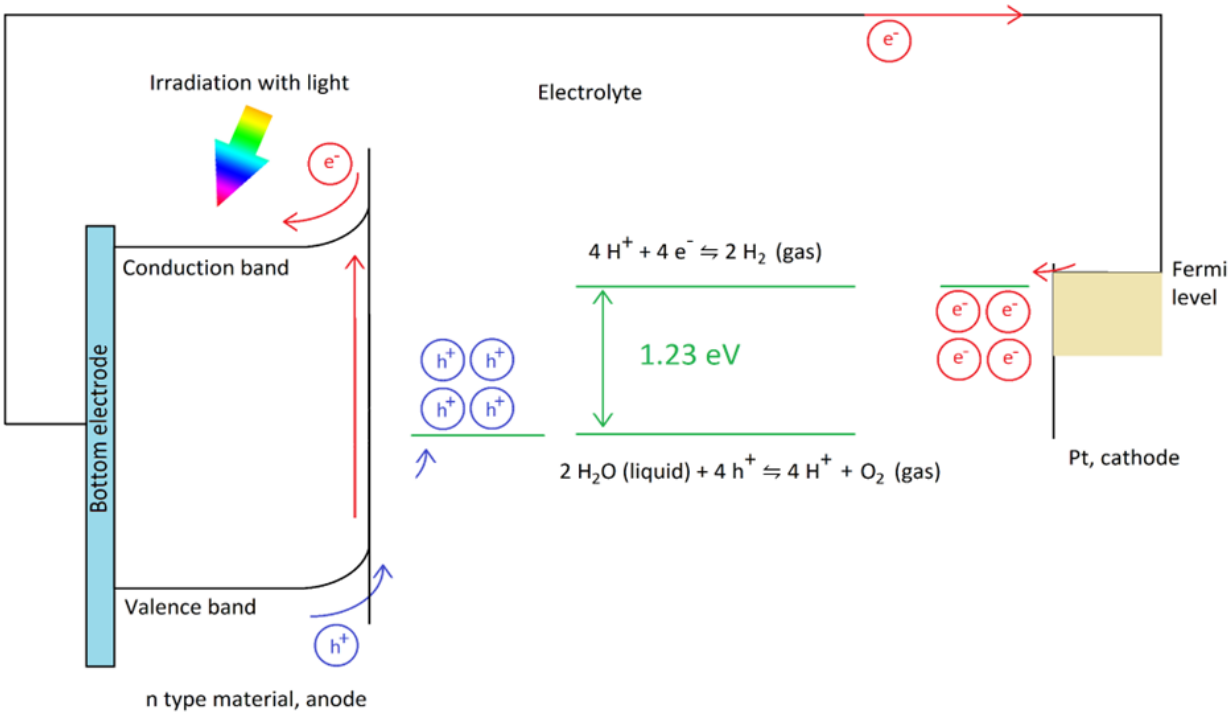

Figure 2.1. Schematic design of the PEC water splitting in a simple cell consisting of a) photoanode and b) photocathode with metal Pt contact.

Electron-hole pair separation can occur due to pn junction if photoelectrode consists of more than one layer of materials. Also, it can happen when external bias is applied to the circuit. After reaching the surface of an electrode, electrons or holes induce the reaction in electrolyte (acidic electrolyte, pH = 0) shown in Equations 2.1 - 2.3, to produce oxygen or hydrogen gas (Bard & Fox, 1995).

Anodic reaction at pH = 0, E^0_{red} =1.229 V vs NHE:

$$2H_2O\ (liquid) + 4h^+ \leftrightharpoons 4H^+ + O_2\ (gas) \qquad \text{Equation 2.1}$$

Cathodic reaction at pH =0, E^0_{red} =0.00 V vs NHE:

$$4H^+ + 4e^- \leftrightharpoons 2H_2\,(gas)$$ Equation 2.2

Overall reaction at pH=0, E^0 =0.00 V vs NHE:

$$H_2O + 2hv \rightarrow H_2 + \frac{1}{2}O_2\,(gas)$$ Equation 2.3

If the electrolyte is basic (pH = 14), means concentration of the ions in solution is lower, OH^- ions have more activity than H^+ ions, while opposite can be observed in acidic media undergoing reactions shown in Equations 2.1 - 2.3.

To define the impact of pH of the solution on standard potential E^0, Nernst equation is used:

$$E = E^0 + \frac{RT}{nF} ln\, ln \left(\frac{a_{Ox}}{a_{Red}}\right)$$ Equation 2.4

where, E is reaction potential, E^0 is standard potential, R is universal gas constant, T is temperature in kelvin, n is number of transferred electrons per ion, F is Faraday constant and a_{Ox}/a_{Red} is reaction quotient, e.g. activity of oxidized and reduced species (Rajeshwar et al., 2008). If we use Nernst equation for standard conditions when T is room temperature (298 K), then threshold potential for the water splitting varies at Nernst rate of - 0.059 V per pH (Rajeshwar et al., 2008). Considering this, photocatalytic activity measurements can be compared for various materials in electrolytes in reversible hydrogen electrode (RHE) scale, with pH influence counted:

$$E_{RHE} = E^0_{Ag/AgCl} + 0.059 * pH$$ Equation 2.5

where, $E^0_{Ag/AgCl}$ is 0.205 V at room temperature (Ag/AgCl reference electrode in 3.5 KCl solution).

If material is n type, e.g., photoanode, holes go to the surface and oxidize water and electrons go to Pt contact as shown in Figure 2.1. If material is p type, e.g., photocathode, electrons diffuse to reach surface and reduce water, holes go to Pt contact.

2.1.2 Requirements for materials to be used as photocatalytic materials in water splitting.

There are many materials that show photoactivity, but only few of them can be used for PEC water splitting applications. Suitable semiconductor materials should possess several properties to be used as water decomposition materials.

Firstly, the required material should have a suitable band gap that is larger than minimum water splitting energy (1.23 eV) to absorb more photons from the solar irradiation and properly aligned band gap edges relative to water decomposition potentials. Material's CB minimum should have more negative value than HER potential and VB maximum should have more positive value than OER potential. 1.23 eV is minimum energy to water decomposition to happen at normal hydrogen electrode scale, but real-case process needs semiconductor material with band gap of at least 1.6-1.7 eV due to different losses.

Secondly, less defects and favorable electrical conductivity of photoelectrodes are crucial properties that allow photo-induced charge carriers to be extracted and transferred.

Thirdly, stability of photoelectrode materials in the aqueous environment is one of the big issues that scientists must be concerned about. Often many materials have poor stability against photo corrosion and photodegradation. To overcome this issue, protective and passivation layers should be investigated and used (Paracchino et al., 2011). Lastly, semiconductor materials for PEC water splitting should be robust and economically viable.

Since the majority of n or p type materials do not meet all the requirements, it has been extremely challenging to identify viable water-splitting photoelectrodes due to these tight restrictions. Anyway, a long journey is expected to find a future material for being a potential photoanode that satisfies all those criteria. Materials must be thoroughly examined in terms of their atomic structure, electronic nature and must show better functional performance as photoelectrode in PEC cells.

Metal oxide semiconductors (MOS) are a class of materials with weak electronic and optical properties compared to such photovoltaic materials as perovskites (Xu et al., 2019), dye sensitized solar cells (Sarkar et al., 2018), etc. However, abundance and prominent stability of MOS make them advantageous for usage as photoelectrode semiconductors in water splitting. Late developments in PEC solar water splitting encompass a variety of metal oxide materials. Recently, TiO_2, WO_3, $BiVO_4$, CuO_2, and their combinations with other materials have made the most progress among the most investigated materials in solar water splitting (Hamdani & Bhaskarwar, 2021). Materials including MOS with proper band gap and alignments are shown in Figure 2.2. It is seen that p type materials such as MoS_2, CuO, Cu_2O, etc. are suitable for

hydrogen evolution and n type materials including $BiVO_4$, WO_3, Fe_2O_3, etc. are best suited for oxygen evolution process.

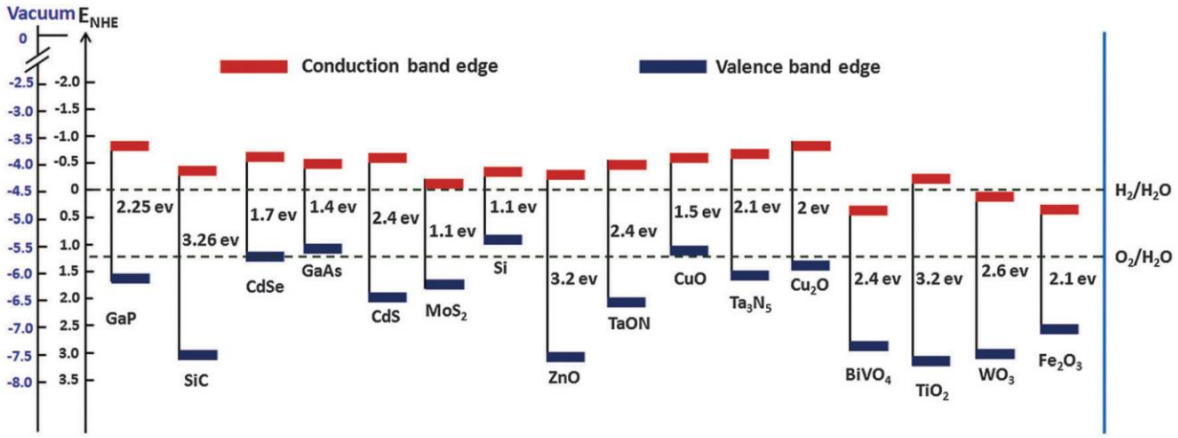

Figure 2.2. Band edges of semiconductor materials while contacting electrolyte of pH = 0 relative to vacuum level and NHE scale. Reprinted with permission from RSC. Ref. (Tamirat et al., 2016).

Recent strategies for photocatalytic property enhancement of MOS.

Some of the most recent approaches rely on using 2D materials in conjunction with TiO_2, WO_3, $BiVO_4$, and CuO_2 photoelectrodes (Masoumi et al., 2022; Rahmani et al., 2017). The main work should be devoted to decreasing the band gap from 2.6-2.8 to 2.4 eV using various strategies and shifting band gap edges to HER potential. Increasing electrical conductivity, improving charge separation via combining with other materials in tandem might considerably enhance STH efficiency. Band gap shifting or changing could be achieved by doping (Kalanur et al., 2020), surface modification (Markhabayeva et al., 2020; Y. Wang et al., 2013) and by making composites with other materials (G. Zheng et al., 2019).

2.2 WO_3 as photoelectrode for PEC water oxidation

2.2.1 WO_3 and its forms

Pure WO_3. Among MOS WO_3 has undergone significant research studies for improving its structural, morphological, optical, electrical, and catalytic properties to be used as photoelectrode in solar water splitting (Costa et al., 2022). Pure WO_3 has a band gap around 2.6 eV (H. Zheng et al., 2011), comparable stability (Costa et al., 2022; Dias et al., 2016; Sarnowska et al., 2016) and

cheaper synthesis cost to utilize in PEC. Band gap structure represents difference of valence maximum (mostly filled with O2p orbitals) and conduction band minimum (empty W5d orbitals) (Hjelm et al., 1996, p. 3). Nevertheless, such a wide band gap, poor charge transport/separation characteristics, and far low position of valence band edge from OER potential substantially limit extensive implementation in effective production of oxygen gas (Shandilya et al., 2022; Y. Wang et al., 2019).

The photocatalytic property of WO_3 was first published by Gary H et al. in 1976 by measuring photocurrent generation on illumination of photoelectrode (Hodes et al., 1976). The stoichiometry of WO_3 is constructed from corner and edge allocation of WO_6 octahedra. Depending on distortion (tilt angle and rotation direction) from WO_6 octahedra it might possess polymorphism in crystalline structure and exhibit the following phase structures: cubic (c-WO_3), hexagonal (h-WO_3), triclinic (δ-WO_3), orthorhombic (β-WO_3), tetragonal (α-WO_3), monoclinic II (ε-WO_3) (Gutpa et al., 2022; X. Liu et al., 2012; Migas et al., 2010, p. 3; Ramana et al., 2006; H. Yang et al., 2019) and the most favorable for catalytic reactions is monoclinic I (γ-WO_3) (de Respinis et al., 2013; Fàbrega et al., 2016; Shabdan et al., 2020). Phase transitions are dependent mostly on annealing and cooling conditions as well as surface morphology treatments (Righettoni & Pratsinis, 2014). Optoelectronic properties and photocatalytic activities of WO_3-based photoelectrodes are significantly affected by oxygen-deficiency (non-stoichiometric) (Bandi & Srivastav, 2021; Huang et al., 2015; Song et al., 2015; Yan et al., 2015), crystallographic grain size distribution (Gullapalli et al., 2010; Vemuri et al., 2012), coating thickness (Apolinário et al., 2019), phase structure and impurities of other elements (doping) (Kalanur et al., 2020; Zych et al., 2022b).

Optical features of WO_3 can be tuned if exposed to various physical and chemical stimulations: thermal treatments, light irradiation, applied electric bias, and various reducing gases (Boateng et al., 2022; S. Wang et al., 2018). Based on those facts, WO_3 and its non-stoichiometric forms (WO_x) are widely involved for the preparation of multifunctional materials with chromism effects (Lee et al., 2006; Y. Zhao et al., 2022), and gas sensing properties (Hwan Cho et al., 2022; Mirzaei et al., 2019). Its chromism property gives opportunity to implement it in a range of applications as light filter windows, segmented or pixel displays, etc. in industry and for household needs (Gu et al., 2022; Y. Li et al., 2018; L. Wang et al., 2023).

Physical, chemical characterizations and photocatalytic activity of WO_3-based photoanodes can also be modified by doping, e.g., by ion intercalation. The eventual condition of the ultimate photoanode material can be affected by numerous doping-related parameters. Doping brings

about complex phase alterations that are not monitored in stoichiometric WO_3. Intercalation of ions causes origination of additional impurity states in WO_3 and leads to the shifting of the material's conduction and valence edges (Kalanur, 2019, p. 3; Kalanur et al., 2020). Nevertheless, many reports maintain crystalline phase stability of WO_3 for induced oxygen vacancies and crystalline structure defects (Kalanur et al., 2019; Song et al., 2015). Sometimes, WO_3 might have a single stable pure phase or a mix of monoclinic-hexagonal phases after doping (Kalanur et al., 2020). Locations of doped impurities within the lattice structure inside the host material also depend on dopants being either transition metal ions, alkali metal ions or alkaline earth metal ions. For instance, transition or post-transition metal dopants undergo substitution at lattice positions (Chandrasekaran et al., 2019; Kalanur et al., 2017, 2018, 2021; Kalanur & Seo, 2018), whereas alkali metal ions like Li^+, Na^+ and alkaline earth metal such as Ba^{2+} also take positions in interstitial cavity (Hjelm et al., 1996, p. 3; Kalanur & Seo, 2019). Most latter mentioned works confirm that introduced impurity inside the WO_3 may induce additional oxygen vacancies, may contribute additional electrons to the conduction band of WO_3 and may change crystalline phases depending on the dopant element radius.

Oxygen deficient WO_{3-x}. As mentioned before, WO_3 lattice can bear an abundant number of oxygen vacancies. This feature allows fabrication of non-stoichiometric, oxygen deficient WO_{3-x} thin films. The presence of oxygen vacancies can boost photocatalytic properties of photoelectrode by increasing conductivity and decreasing photoelectrode band gap (Bandi & Srivastav, 2021; Bao et al., 2017; Yoon et al., 2011). Visual appearance of WO_{3-x} thin films differs from pure WO_3 in the sense that they possess enhanced absorbance for the wavelengths longer than 480 nm in visible range of light (Yan et al., 2015). Such enhanced absorbance on WO_{3-x} materials is assigned to the creation of additional states by oxygen vacancies right under the conduction band of semiconductor and furthermore, assigned to LSPR effect induced by oscillation of excess free electrons in conduction band of oxygen deficient WO_x (Yan et al., 2015). However, they have a transmission slot in the blue-green region of the spectrum which makes them light-green or olive grab in appearance (Woodward et al., 1997; H. Zheng et al., 2011).

WO_3 Hydrates. Recently, hydrated WO_3 photoelectrodes have been broadly implemented in photocatalysis for their better charge transfer and splitting properties and unique structure with water intercalation ($WO_3 \cdot nH_2O$) (Jaiswal & Choudhury, 2022). There are several most studied types of hydrated WO_3 with various phase structures and different bonding of water molecules

with WO_3 lattice positions: $WO_3 \cdot 2H_2O$ (dihydrate), $WO_3 \cdot H_2O$ (monohydrate), $WO_3 \cdot 0.5H_2O$ (hemihydrate), and $WO_3 \cdot 0.33H_2O$ (H. Zheng et al., 2011).

2.2.2 Synthesis of WO_3

Solution-phase synthesis. WO_3 and its oxygen deficient counterparts can be obtained by uncomplicated and fast solution-phase methods such as hydrothermal, sol-gel, and solvothermal (Azam et al., 2018; Ghazal et al., 2022; Hu et al., 2020; Y. Wang et al., 2021; M. Yang et al., 2021). They allow to synthesize nanostructures with diverse shapes: nanorods (Nakate et al., 2021), nanoparticles (D. Zhang et al., 2019), nanosheets (Yu et al., 2022), plate-like (Jamali & Shariatmadar Tehrani, 2020), hollow-microspheres (Y. Wang et al., 2021), nanoflowers (L. Zhao et al., 2020).

Among all, the sol-gel spin-coating method gives scalable straightforward deposition of homogeneous, ultrathin thin films for usage as photoanode in PEC (Chen et al., 2018; Sang & Kim, 2022). B. Chen et al. deposited thin film thickness of as thin as 10-15 nm from one layer sol-gel spin-coating of prepared solution (Chen et al., 2018). Spin-coating parameters such as rotational speed, rotation time, rotation increasing ramp, and number of layers can be justified to deposit thin film with desired thickness and homogeneity. It's interesting to note that the coupling of the sol gel spin-coating method with a subsequent solvothermal procedure creates a path for the fabrication of nanorods and tilted nanocolumns as well as other heterojunctions onto the spin-coated seed layer (Su et al., 2011; J. Zhang et al., 2015). Such nanostructures boost light trapping by increasing light pass through the material by scattering, increase surface area at electrode-electrolyte interface, facilitate charge separation by creating junctions, and ultimately promote photocurrent conversion efficiencies in PEC.

Vapor-phase synthesis. Vapor-phase deposition techniques are divided into two categories in this context: chemical vapor deposition (CVD) and physical vapor deposition (PVD). Those methods cover sputter deposition, electron beam evaporation (pulsed e-beam), laser beam evaporation (pulsed-laser), molecular beam epitaxial growth method, etc. CVD methods have long scale usage in semiconductor preparation and include atomic layer deposition (ALD), CVD tube furnace deposition, etc. Overall, the advantages of vapor-phase synthesis include complete control over film growth during deposition, wide area thin film synthesis, ideal homogeneity and good adhesion of films, possibility of low temperature deposition, reproducibility of films,

minimization of human interaction (Guerin & Hayden, 2006; Reichelt & Jiang, 1990; Shishkovsky & Lebedev, 2011).

PVD vapor-phase synthesis often requires a high or ultra-high vacuum environment that prevents collisions of evaporated or sputtered ions with chamber atmosphere constituents, to reduce thin film contaminations during the growth. Consequently, the cost of such equipment, supporting facilities, supplementary components and maintenance services make it economically inadequate. Despite this, numerous papers report $WO_{3\leq x}$ photoelectrodes obtained by PVD methods with good quality and superior performance for miscellaneous applications (Gutpa et al., 2022; Najafi-Ashtiani, 2019). Most of the time, during the PVD operations, the substrate temperature has a significant impact on the thin film properties (Chaabouni et al., 2004). Each PVD method can be divided into subclasses where they differ from one another with distinguishable characteristics. For instance, magnetron sputtering with direct current (DC-MS), magnetron sputtering with radio frequency (RF-MS), dual MS, magnetron sputtering with high power impulse (HiPIMS) (Lou et al., 2022), unbalanced-balanced MS (Svadkovski et al., 2002), etc.

DC-MS allows to fabricate $WO_{3\leq x}$ coatings reactively from a tungsten target. Reactive DC-MS deposition means employment of reactive gas for the process. Our results in the following chapters show that room temperature DC-MS coatings of $WO_{3\leq x}$ exhibit homogeneous thin films with amorphous nature. The coating of $WO_{3\leq x}$ thin film with DC-MS method begins in a chamber (initially high-vacuum) which contains an atmosphere of non-reactive noble gas such as argon. Then, reactive gas, oxygen, is sent into the chamber. Schematic representation is given in Figure 2.3-a. As a result of applied bias voltage, electrons start to escape the target material (cathode) and move through the generated electric field to reach the second electrode (anode). However, as in most planar magnetrons, magnetic fields near the target material and its perpendicular arrangement with electric fields force electrons to undergo cycloidal drift and be confined in the vicinity of the surface of target material (Figure 2.3-b). Confined electrons collide with gas molecules by ionizing them and creating plasma (Figure 2.3-c). Heavy gas ions affected by electric fields begin bombardment of the target material surface and enter target material (tungsten) by making collision cascades inside. Accordingly, three particle types alter their momentum with impending gas ions: target material ions, secondary electrons, and neutral atoms of target material. Target material ions cannot escape proximity to the surface due to the electric field and come back to punch the target. Secondary electrons are also imprisoned near the surface and participate further in ionization of gas molecules. Neutral atoms of target material will not be affected by anything and go through the schematically arranged path to land on

substrate material. Despite such harmony, contamination of target material surface and substrate is inevitable, and it is called target poisoning. Target poisoning often happens when the reactive gases are involved and to avoid this effect, target plasma cleaning is needed before each process or a pulsed regime should be used.

The sputtering process regime in which incident material ions land onto a substrate under specific angle (angle between substrate and its normal is less than 90°) is called glancing angle deposition (GLAD) regime. GLAD is a versatile method for controlling the growth shape of WO_3 by means of shadowing effect (Ai & Zhao, 2018). Regulating substrate holder rotation under the GLAD regime helps to produce columnar (Ollitrault et al., 2015), nanorod (Pihosh et al., 2015), helix (Figueroa et al., 2007), etc. shaped WO_3 nanostructures. For the confirmation, recent work of S. Limwichean et al. reports precise control of morphology and influence of GLAD angle on PEC performance of WO_3 photoelectrode (Limwichean et al., 2021).

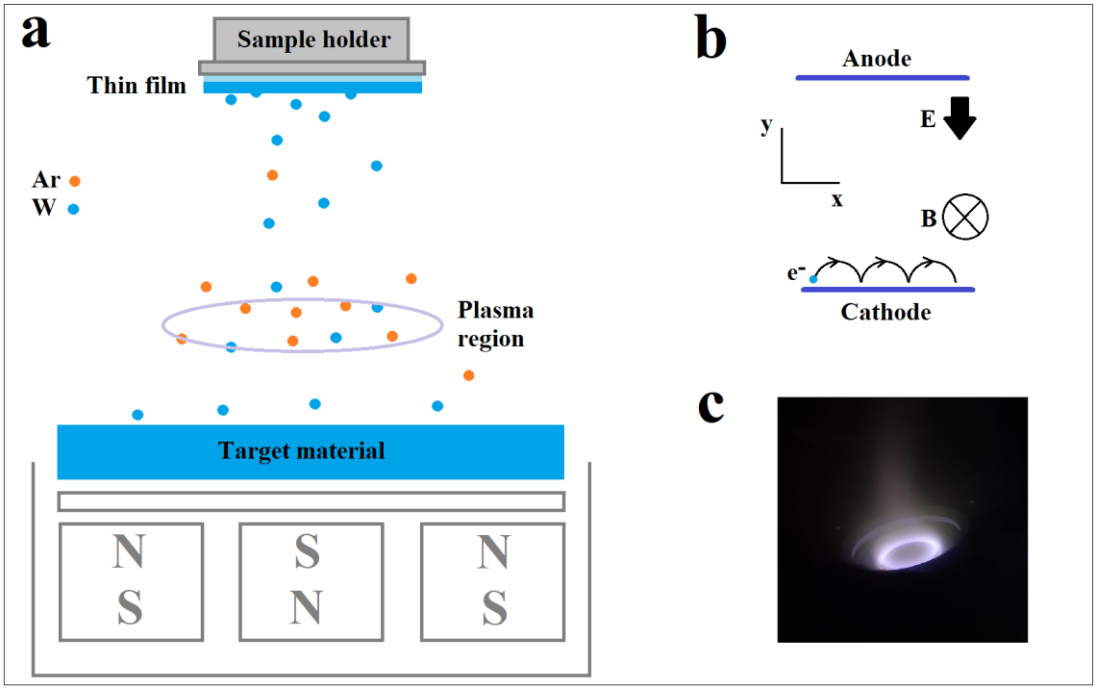

Figure 2.3. Schematic diagram of a) DC-MS process, b) cycloidal drift of electron and c) plasma created by sputter deposition.

Other synthesis methods. There are other ways to create WO_3-based materials: electrochemical methods, using templates, meshes or pre-treated substrates.

Anodization and electrodeposition are two electrochemical methods widely used for $WO_{3\leq x}$ synthesis. Anodization is performed in an electrochemical cell system by applying bias between

two electrodes, which one is anodic metal that oxidizes to create pure and non-stoichiometric tungsten-based oxides (Fernández-Domene et al., 2023; Zhu et al., 2014). Mohammad B. R. and co-workers fabricated WO_3 hydrogen gas sensors from pre-sputtered W film on quartz substrates by anodization (Rahmani et al., 2017). Marta Zych et al. investigated that anodization allows co-doping of WO_3 with C, N and opens a way to tune its photocatalytic activity by managing applied bias voltage and electrolyte ion concentration (Zych et al., 2022b). Report by Tao Zhang et al. also confirms significance of anodization temperature and voltage on changing porosity of created thin films (T. Zhang et al., 2020). Hydrated monoclinic $WO_3 \cdot 2H_2O$ nano platelets as powders were successfully obtained by Shizhao Wu et al. using ethylene glycol (EG) in electrolyte (Wu et al., 2019).

As for electrodeposition, WO_3-based materials are produced by gathering tungsten ions on substrate acting as working electrodes in three electrode cell systems, and in the electrolytes that contain sodium tungstate (Demir, 2020), tungstic acid (Mandlekar et al., 2023), and other precursors. In electrodeposition, as in last cited references, the process time, substrates contribute significantly to film properties.

Utilization of pre-prepared templates, differently shaped meshes, and pre-texturing for WO3 synthesis gives additional opportunity for light management (Martins et al., 2022), thin film porosity (Yanagishita et al., 2022). Recently, Xueming Dang et al. discussed synthesis methods , importance, and future application perspectives of WO_3-based inverse opal photonic crystals (Dang et al., 2021). Such porous material with unique characteristics is prepared by filling specially designed templates with relevant precursors and subsequently removing templates with dissolving process or chemical corrosion.

Ultimate synthesis pathways for industrial scale should be economically viable, fast and should support preparation of photoanodes of large area.

2.3 Modification methods of $WO_{3\leq x}$ for PEC photocatalysis.

Overall, $WO_{3\leq x}$ structures and their composites might have amorphous or crystalline nature after synthesis. For PEC applications it is favorable to utilize crystalline phased $WO_{3\leq x}$ due to their narrow band gap. Amorphous or crystalline $WO_{3\leq x}$ photoelectrodes are often subjected to diverse annealing, irradiation approaches and composite making strategies for the photocatalytic application purposes.

2.3.1 Modifications with annealing

Post-synthesis annealing leads to crystallization to a particular lattice phase by $WO_{3\leq x}$. Important to note that annealing temperature, atmosphere, temperature ramp, annealing time, cooling rate and time considerably influence consecutive material's photocatalytic nature (C. Ng et al., 2013; Roselló-Márquez et al., 2020). Additionally, texturing can be carried out by different annealing scenarios to make high-performance photoactive single crystal $WO_{3\leq x}$, or to induce more stable facets for photocatalytic activity (M. Yang et al., 2021; J. Zhang et al., 2015). Up to now, most annealing methods include annealing in ordinary furnace, rapid thermal annealing, annealing with flash lamp, and hot plate annealing (Efkere et al., 2021; Jiang et al., 2020).

2.3.2 Modifications and synthesis with laser-based technology.

Laser beam synthesis and modifications in pulsed or continuous regimes might be performed to synthesize $WO_{3\leq x}$ thin films or alter their properties after fabrication (Di Fonzo et al., 2006). Pulsed laser deposition (PLD) approach involves exposing metallic tungsten to laser beams of pulse duration of 10-15 ns or7ns in chambers with different atmospheric conditions in order to induce $WO_{3\leq x}$ phases (Besozzi et al., 2019; Dellasega et al., 2015). Photoactivity of most PLD created nanomaterials, as in DC-MS, is dependent on oxygen partial pressure, for instance, Sun Shin et al. created tree-like WO_3 photoanodes at 100 mTorr chamber O_2 partial pressure that showed better photocatalytic performance after subsequent annealing (Shin et al., 2015). In 2012, Chao Zhang et al. studied $WO_{3\leq x}$ by exposure to laser irradiation for the improvement of gas sensing properties (C. Zhang et al., 2012). Recently, Sainan Ma and co-workers used laser beams for drilling of WS_2/WO_3 heterostructure to create porous structured electrodes for photocatalysis (S. Ma et al., 2017).

2.3.3 Modification with ion beam irradiations.

Synthesis or annealing can be followed by ion beam irradiations to modify surface or bulk nature of nanomaterials. Previous reports show the possibilities of using ion beam irradiations for the modification of $WO_{3\leq x}$ for studying photocatalytic activity (Kozlovskiy et al., 2021), ferromagnetic properties (X. Zheng et al., 2021), gas sensing properties (Ram et al., 2020), etc.

Overall, modifications with ion beam irradiation can be divided into several types depending on ion-nanomaterial interactions: ion implantation, annealing, sputtering, defect generation and engineering (X. Wang et al., 2020). Those modifications make it possible to create heterostructures, various type nanostructures, and band gap tuning and change of opto-electronic properties of materials.

Particularly, ion beam irradiation is used for the implantation of element atoms into a host material to alter its properties. Implanted elements induce additional electronic states in the host material and change its electronic, optical, etc. properties and tunes band gaps (Anpo et al., 2001; Yamashita et al., 2003, p. 2). Ion implantation via irradiation is an easy and efficient doping method compared to chemical doping since chemical doping needs suitable precursors and has other limits.

Sputtering processes take place on ion beam irradiation of material along with annealing or implantation. It may be used to clean up or modify the surface of the material for further integration into various applications.

Defect generation and engineering can be done using irradiation methods with ion beams. Ion beam induces point defects, dislocations, vacancy creations or amorphization processes in the relevant material. In the most oxide-based materials, ion beam irradiation leads to oxygen vacancy generation, which is the most widespread point defect favorable for many applications. Oxygen vacancy creation occurs when energetic ions go deep into the WO_3 material and penetrating ions knock out O or W atoms from their equilibrium lattice locations. This provokes creation of vacancies inside the material. Ion energy, fluence and type can be governed to induce a proper type or number of vacancies. Very recent study by Yuki Nakagawa et al. revealed that irradiation by He^+ and Ar^+ ions with fluence of 10^{16} ions/cm^2 (100 keV) induces oxygen vacancies in $WO_{3\leq x}$ (Nakagawa et al., 2022, p. 3). Oxygen vacancy creation was also confirmed by Xudong Zheng et al. in their work on irradiation WO_3 with Ar^+ ions (130 keV) (X. Zheng et al., 2021). As mentioned previously, optimum concentrations of oxygen vacancies in PEC photoelectrodes have a positive effect on photocatalytic activity (Tan et al., 2014). Artem L. Kozlovskiy et al. studied low-energy helium ion irradiation of WO_3 microparticles for usage as catalyst in the decomposition of Rhodamine B and it was revealed that He^+ irradiation increases photocatalytic activity (Kozlovskiy et al., 2021). Non-optimized, excess number of oxygen vacancies might act as recombination centers for electrons and holes in PEC.

Annealing via ion beam irradiation occurs while energetic ions strike the material surface and give their kinetic energy to the surface layer by increasing temperature. Using high-current ion

beams, it is possible to achieve annealing temperature rise by hundreds or thousands of degrees (Remnev et al., 1999). Annealing in such a way may induce phases recrystallization in the material.

Ion beam irradiation with relatively low ion beam intensity is extensively used to modify WO_3 for PEC applications, while effects of IPIB irradiation, to the best of our knowledge, were not yet studied Theoretical concepts, interactions and subsequent consequences of ion beam irradiations are broadly discussed in the next section.

2.4 Modification of materials with Ion beam irradiation

Ion beam irradiation. In general, ion beam irradiation of materials can be categorized into low-energy (several keV), medium-energy (from 10 to MeV), and high-energy (more than MeV) irradiations depending on energy per nucleon (Xiang et al., 2021). In addition, ion beams can be of relatively low current, resulting in the rise of annealing temperature by just a few degrees, or the high current ion beams – leading to the temperature rise of hundreds or thousands of degrees. During the irradiation process, upcoming ions having specific energy undergo electromagnetic interaction (Coulomb interaction) with each atom of the nanomaterial lattice (X. Wang et al., 2020). As a result of interaction, elastic or inelastic collisions and energy exchange may occur between incident ions and lattice atoms or electrons. Consequently, penetrating ions induce several modifications in material lattice by making collision cascades as demonstrated in Figure 2.4: doping, vacancy creation, interstitial exchange as well as substitutional location exchange between ions and lattice constituents. All of those modifications alter material's optoelectronic, structural and morphological properties.

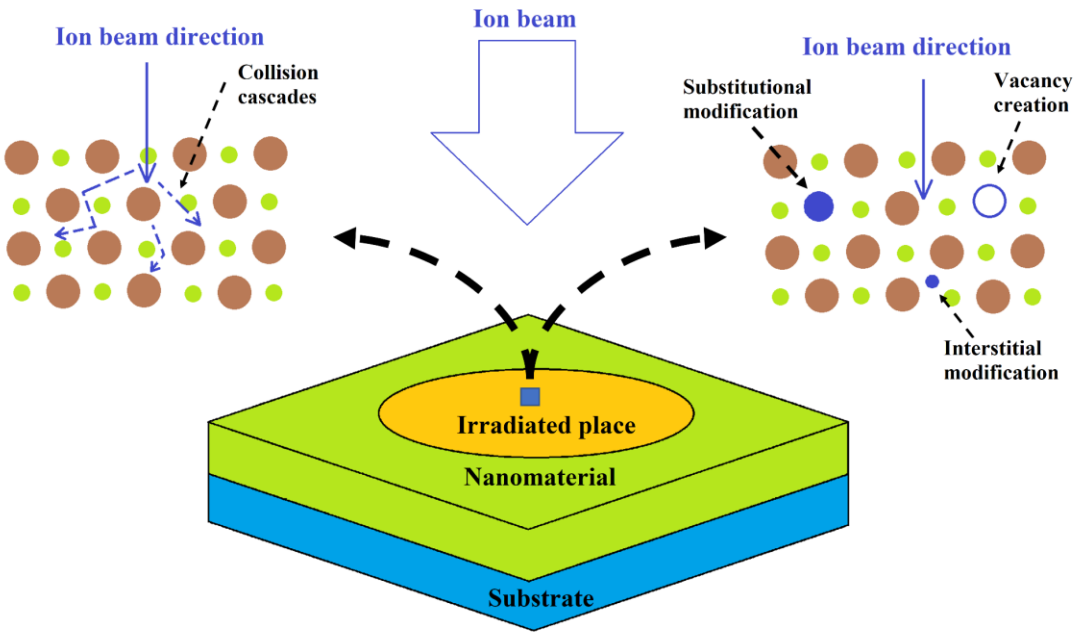

Figure 2.4. Schematic demonstration of collision cascades and lattice modifications induced by ion irradiation.

Furthermore, point defects in the form of vacancies or interstitial dopants may diffuse through the material lattice structure and cause generation of lattice distortions and dislocations. Creation of dislocation-defects (dislocation -loops, -lines) often arise from formation, accumulation, and again breaking up of vacancies and interstitial defects as ion interacts with the material constituents (Sivakumar et al., 2007). Lattice dislocations can be type of edge dislocations and screw dislocations or mix (*Introduction to Dislocations*, 2011). Depending on concentration of such dislocations, photoactivity of photoanode can be tuned. In the very recent work of Sihan Ma et al. BiOI nanosheets were obtained and irradiated with N^+ ions, after which they observed high-concentration of lattice line dislocations in BiOI nanosheets that caused photocatalytic property enhancement ($2.5*10^{15}$ ions/cm^2, 300 keV) (S. Ma et al., 2023). In our experiments on WO_3 thin films, we observed the dislocation presence after IPIB irradiation of WO_3 under TEM imaging which we broadly discussed in upcoming chapters. Ion induced clustering and migration of point defects may further lead to the creation of dislocation loops or voids (Hwang et al., 2016). Fast temperature increase/decrease and ion beam action induce various morphological and structural alterations in WO_3.

Intense Pulsed Ion Beam Irradiations. IPIB irradiation is one-pulse high current ion beam irradiation process in which energy is transferred within the time slot of 10-100 nanoseconds inducing ultra-fast annealing of irradiated materials.

Three main phenomena or their combinations may arise in the vicinity of the surface of solid material while it is irradiated with short intense ion beams: thermal influence, thermal influence with mass transport, and shock wave creation (Piekoszewski & Langner, 1991). During the thermal influence, one- pulse ion irradiation delivered energy converted into the heat by raising temperature to the several hundred Celcius degrees. For the second case, the ion beam thermal effect is combined with mass transport and should have an ion beam dose from 10^{14} to 10^{18} ions/cm^2. Therefore, those doses are enough to make doping, create vacancies and dislocations or change structural composition in the host material. Shock wave creation leads to rebound or evaporation of irradiated part of material from the surface because of newly generated pressure pulses. Occasionally, generation of pressure pulses by shock waves may occur with only quick expansion of irradiated parts of material without evaporation (Piekoszewski & Langner, 1991). There are several uses for pulsed ion beam irradiation, including nuclear fusion and plasma physics research, semiconductor manufacturing, and materials science. It may be used to alter the surface characteristics of materials, make nanostructures, thin films, and research how materials behave in harsh environments (Solovan et al., 2023).

2.5 Plasmonic NPs and their applications in PEC

Incorporation of co-catalysts into PEC photoanodes is a one of the good strategies to increase efficiency of water splitting (Rosman et al., 2022). Briefly, the main function of co-catalysts is supply of more catalytically active sites that need lower activation energy for chemical processes than bare photoelectrodes. Plasmonic nanoparticles as the one of co-catalysts, might be directly deposited onto semiconductors or incorporated within semiconductors and take part in many processes.

Nanoscale particles of noble metals such as gold, copper or silver have unique properties due to their plasmonic effect while interacting with incident ultraviolet (UV) and visible (VIS) electromagnetic waves. Surface plasmon resonance (SPR) or localized surface plasmon resonance (LSPR) occurs when valence electrons of noble metals oscillate collectively in

resonance with the frequency of incident photons. Resonant photon wavelengths strongly depend on noble metal nature, size, and shape (Marhaba, 2018). By managing the shape, size and type of metal nanoparticles, it is possible to fabricate nanoparticles with plasmonic effects that cover the whole solar spectrum (Jain et al., 2008) for further usage in solar cells, water splitting, etc.
SPR happens frequently on the surface of thin metal films, whereas LSPR is induced in metallic nanoparticles of various shapes as shown in Figure 2.5. SPR or LSPR is described by a non-uniform, intensive and oscillating electric field in the vicinity of thin films or NPs.

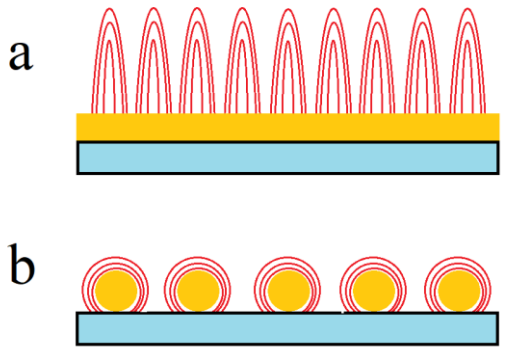

Figure 2.5. Schematic illustration of the a) SPR and b) LSPR effects around metallic NP as it interacts with light.

Interest in using plasmonic NP co-catalysts with photoelectrodes is shown due to the SPR properties of plasmonic nanostructures that enhance light absorbance of electrodes in visible range. A variety of mechanisms in which plasmonic nanoparticles might interact with semiconductor materials are well discussed in many reports and include hot electron supply, surface plasmon resonance effect for electron-hole creation (near field mechanism) and scattering of incident light and its concentration for trapping inside the material (Abouelela et al., 2021; Atabaev, 2018; J. Li et al., 2021).

Direct charge injection or hot electron supply mechanism. In this mechanism, plasmonic metal nanoparticles embedded in semiconductors absorb photon energy from light irradiation and directly transfers energetic charge carriers to the semiconductor (Gomes Silva et al., 2011; Hou et al., 2017). This electron transfer mechanism works if plasmonic NPs and photoelectrodes are in touch with each other supporting quick transfer of electrons. For the process to occur, electrons should possess enough energy to overcome the energy barrier (Schottky barrier) that is present at plasmonic metal NP/semiconductor interface (B.-T. Zhang et al., 2017).

Near field mechanism. There have been increases in photocatalytic properties of photoelectrodes while having plasmonic NPs located in the vicinity that are not in direct contact. SPR induced photocatalytic boost arises in cases of plasmonic NPs/photoelectrode separation with thin film of other materials or dielectric spacers. In these cases, photocatalytic enhancement occurs due to near field mechanisms or light scattering. The near field mechanism is described by the generation of spatially non-homogeneous electric fields around plasmonic NPs by oscillating free electrons in plasmonic metal NPs due to interaction with light. The intensity of these fields decays exponentially as distance from NP increases. The highest intensity of these fields is present at the surface of plasmonic NPs. When photoelectrode material is brought into the vicinity of plasmonic NPs it encounters these intense fields. It is known that electron-hole generation rate for a semiconductor material is dependent on the local power of the electric fields (Z. Liu et al., 2011). Consequently, extreme presence of built-up electric fields around plasmonic NPs boost photocatalytic rate at the interface between NPs and semiconductors (D. Liu & Xue, 2021). Plasmonic NPs are frequently deposited on the surface of photocatalytic materials. This highlights the fact that towards the surface as opposed to the bulk bottom region, the electron-hole separation rate of photocatalytic material is higher. This fact increases the probability that holes or electrons will successfully generate oxygen or hydrogen by allowing them to go to the surface quickly.

Light scattering mechanism. If bigger plasmonic NPs are embedded into semiconductors, resonant photon scattering may take place (Evanoff & Chumanov, 2005). By trapping and lengthening the average path of input photons, those NPs' primary function can be considered as scattering light further into semiconductors. In this mechanism, there is a higher chance that trapped photons will engage in photocatalytic activity.

Designing the right alignment of plasmonic NPs connected to semiconductors is crucial for the mentioned mechanisms, in addition to size, shape, and composition. To achieve the best results, particle to particle distance, which affects the strength of the electric field, and particle to semiconductor distance, which affects photocatalytic characteristics, must be carefully planned and coordinated (Linic et al., 2011).

3. Experimental methods

3.1 Equipment used for synthesis and annealing of thin films.

In current work, DC MS was carried out using the Kurt Lesker magnetron system as seen in Figure 3.1-a with target-substrate distance of 13 cm. This magnetron system can provide a high vacuum condition before deposition and support two gas systems for Ar and O_2/N_2 gases. Spin-coating depositions were done using a spin coating system. Figure 3.1-b shows Brewer Science tool used for spin-coating of thin films and NPs on various substrates. Varying parameters such as spin-coating rotational speed, rotation time and speed ramp, it is possible to control thin film thickness. Figure 3.1-c shows RTA system MILA 5000 that was used for thesis work. It allows to anneal the nanomaterials up to 1000 °C with the increasing ramp up to 50 °C/s.

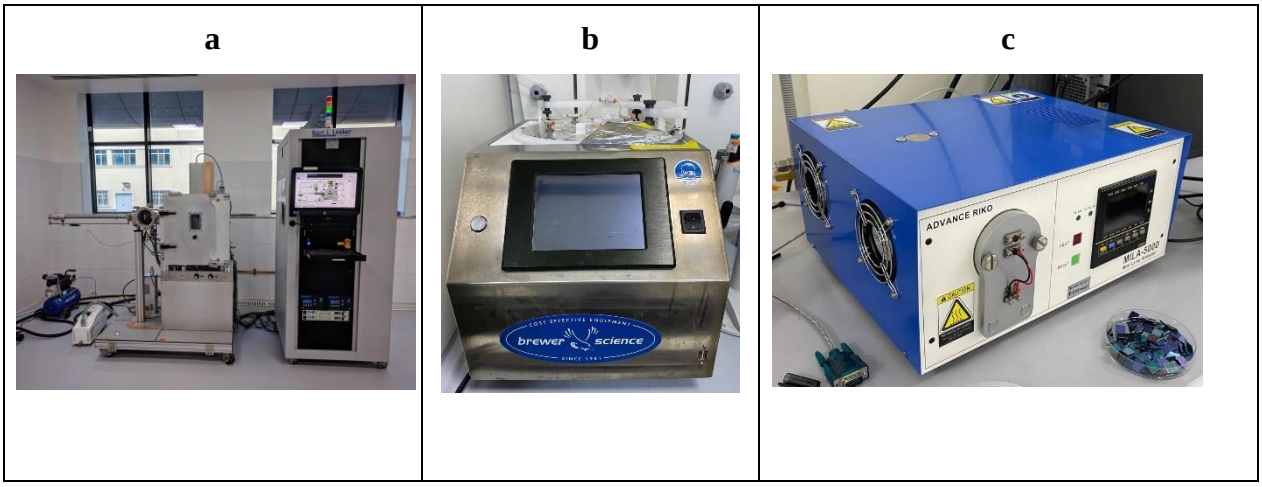

Figure 3.1. The pictures of a) the Kurt Lesker magnetron system, b) spin coating system and c) RTA system that were used for this thesis work.

3.2 "INURA" accelerator facility characteristics.

In current work, IPIB irradiation was carried out for the modification of amorphous and crystalline, or double-layer WO_3 coatings as well as as-deposited Ag thin films with various thicknesses. For that, the Innovative Nazarbayev University's Research Accelerator (INURA) high-current pulsed ion accelerator was used (Kaikanov et al., 2016). The INURA accelerator is an economically viable and adaptable system that can generate 100 ns high current proton ion beam pulses accelerated up to 400 keV. The proton ion beam current can reach up to the 10 kA reaching the current density up to 400 A/cm^2. The overall view of the accelerator is given in

Figure 3.2. Accelerator has accessory systems such as water cleaning and preparation system, gas system, automatic controlling system and pumping system.

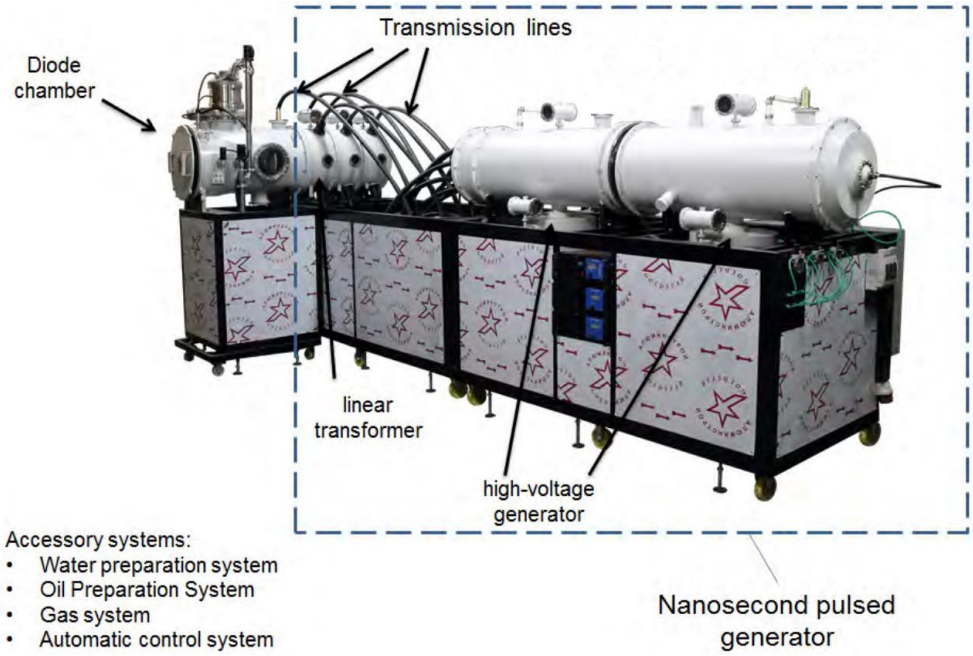

Figure 3.2. The INURA accelerator.

3.3 Beam formation in INURA accelerator and surface modification of WO_3 thin films.

Modification for all samples is performed in the accelerator diode chamber (Figure 3.2) under high vacuum conditions at working pressure of 0.8 kPa. In the chamber, the target material, which is going to be irradiated, is placed in front of the diode with focusing geometry where ions are generated and accelerated. Shortly, the energy is accumulated in the 3 μF capacitor bank and then given to the Blumlein (pulse generator) via pulse transformer. The Blumlein's highest charging voltage ranges from 180 to 200 kV. Subsequently, N_2 gas containing spark-gap in Blumlein gives self-breakdown. The high-voltage pulse is given to the B-applied ion diode via transmission lines and the step-up transformer. Flash-over discharging happens on the surface in the vicinity of the anode made up of copper covered with a polymer dielectric when subjected to such a high applied voltage pulse. Furthermore, due to the influence of the similar second voltage pulse, ions are taken from the flashover discharge plasma and accelerated through the gap between anode and cathode gap of the ion diode where there are no magnetic field lines.

3.4 Photoanode thin films characterization techniques.

3.4.1 X-Ray Diffraction

XRD is a non-destructive method used for analysis of atomic crystalline structures and physio-chemical properties of thin films by detecting scattered from the sample X-ray beams at specific angles (Hammond, Christopher., 2015). Principle of XRD analysis is based on Bragg's formula:

$$n\lambda = 2d_{hkl}sin\theta$$

where n is reflection order, d_{hkl} is distance between planes of the crystalline lattice indicated by Miller indices, θ is angle of incidence of X-ray beam, λ is wavelength of beam equivalent to the crystalline lattice spacing (Hammond, Christopher., 2015). Constructive interference of the reflected beams from lattice planes gives the highest intensity in detector at specific θ angle. The real reason for the scattering is due to electrons in the lattice.

3.4.2 X-Ray Photoelectron Spectroscopy

XPS is a method for analyzing the surface of thin films to determine their chemical states as well as elemental composition by using photoelectric effect principles (Watts, John F., and John Wolstenholme, 2019). The working principle is described by an X-ray beam directed to the surface of the sample where it ejects core electrons of atoms comprising the material. After, kinetic energy and numbers of ejected electron are detected by the XPS machine detector and analyzed to construct XPS spectrum. Binding energies E_b of the peaks in spectrum are individual for specific element and can be obtained by the following formula:

$$E_b = h\upsilon - E_k - \phi$$

where E_k is electron kinetic energy, $h\upsilon$ is energy of incident X-ray photons, ϕ is equipment work function (equipment correction factor) (Watts, John F., and John Wolstenholme, 2019).

3.4.3 Ultraviolet-Visible Spectroscopy

UV-VIS spectroscopy is a spectroscopic technique for measuring optical characteristics of thin films in ultraviolet and visible regions of the electromagnetic spectrum. While radiation in UV-VIS region interacts with thin films, particular processes can happen such as reflections, scatterings, absorbing, fluorescent absorbance and re-emittance, photon induced other chemical reactions. Commonly, absorbance is obtained when measuring the sample with UV-VIS

spectroscopy. Absorbing processes happen when electrons in atoms take incident photon energy and are excited to high energy states. In the case of semiconductor thin films, UV-VIS spectroscopy suggests the simple method to determine the band gaps of the materials. Since, it examines electronic transitions concerning valence and conduction bands of semiconductor thin films. However, optical properties data obtained by UV-VIS spectroscopy do not always give exact band gap estimation due to several factors such as exciton dissociation energies, d-d transitions that can be considered as electron transformations rather than transitions, and phonon interactions. Even though the elaboration of optical properties is dependent on many factors, better understanding of optical band gaps for semiconductors is reachable with UV-VIS spectroscopy. Obtained optical data can give information about the band gap of thin films based on the Tauc method (Makuła et al., 2018).

3.4.4 Transmission Electron Microscopy

TEM is an electron microscopy method that images using transmitted electrons that propagate through a very thin sample (Brandon & Kaplan, 2010). Its high resolution can be used to image crystallographic lattice plane orientations, dislocations, grains with their boundaries and defects. Additionally, diffraction patterns obtained by TEM can give information about the crystallographic structure of thin film and its corresponding lattice plane indices.

3.4.5 Scanning Electron Microscopy

SEM is a microscopic technique that images surface landscape of the thin films in high vacuum conditions by visualizing with focused electron beams. The signals that are detected either secondary electrons which were ejected by incident electrons from the sample surface or backscattered electrons which are reflected (Reimer, 1998). Along with secondary or backscattered electrons, electron-matter interaction includes signals such as characteristic X-rays, cathodoluminescence, transmitted and diffracted electrons. Surface topography of some non-conductive samples may need additional covering with thin conductive layers of metals for better imaging due to charging effects at the sample surface.

3.5 Photocatalytic activity measurement techniques

All the PEC measurements are done using the three-electrode cell - 5 ml inner volume, made-up of polytetrafluoroethylene, quartz window 20 mm in diameter with Ag/AgCl reference electrode shown in Figure 3.3. Sunlight induced water electrolysis and PEC measurements are carried out in Na_2SO_4 electrolyte due to low conductivity of pure water.

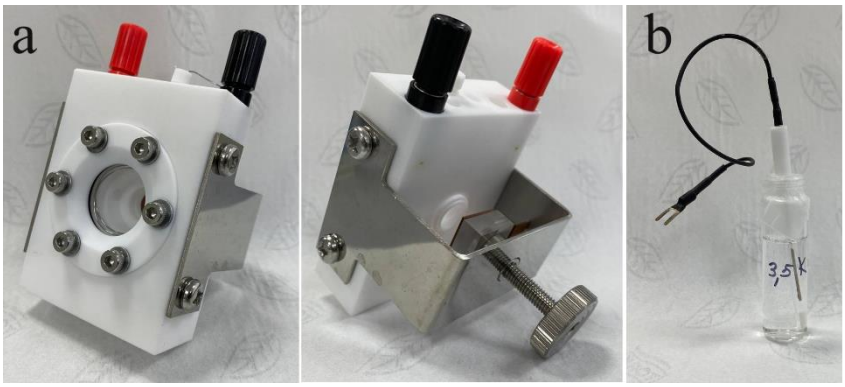

Figure 3.3. a) The three-electrode cell and b) Ag/AgCl reference electrode.

3.5.1 Linear Sweep Voltammetry measurement

Linear sweep voltammetry (LSV) (also called polarization curve measurements) is an electrochemical method for assessing performance of photoelectrode materials. In this technique, photocurrent density is measured at low scan rate and using standard AM 1.5G light radiation (100 mW/cm^2) at WE while potential between WE and RE changes linearly by time. It gives information about onset current where photocurrent density goes up to positive current and where oxidation starts. Plateau current is steady state current where photocurrent does not change after reaching some value while increasing applied bias.

Photocurrent transient measurements (optically chopped LSV) are done during the LSV measurements by opening and closing the light source periodically with a shutter. It can be also measured during the photocurrent-time measurements where the potential is held constant.

3.5.2 Electrochemical Impedance Spectroscopy

EIS is a method in electrochemistry for studying surface charge transport properties of the photoelectrode materials. System impedance is used as a defining parameter instead of simple resistance due to the complex nature of the system involved in PEC. In this technique, impedance

is measured by applying AC bias to the cell and simultaneously measuring current over the cell. If we apply sinusoidal potential bias, then measured current also should be AC current. While doing EIS measurement, the system should be perturbed by a very small signal. Because in small enough bias excitation, the photocurrent response of the semiconductor electrode is pseudo-linear. Only in linear systems current response to sinusoidally changing potential will be at the same frequency but with shifted phase. If perturbed signal potential has the following form:

$$E_t = E_0 \sin(\theta t) \qquad \text{Equation 3.1}$$

where E_t – applied potential at t, E_0 – potential amplitude, θ is frequency. As was mentioned, in linear system, response current has the following form with shifter phase:

$$I_t = I_0 \sin(\theta t + \varphi) \qquad \text{Equation 3.2}$$

where I_t – measured current at t, I_0 – current amplitude. In analogy with Ohm's Law, the system's impedance (Z) can be found in the following manner:

$$Z = \frac{E_t}{I_t} = \frac{E_0 \sin(\theta t)}{I_0 \sin(\theta t+\varphi)} = Z_0 \frac{\sin(\theta t)}{\sin(\theta t+\varphi)} \qquad \text{Equation 3.3}$$

where Z_0 – impedance amplitude. If Euler's formula is used, impedance can be expressed in complex function form:

$$E_t = E_0 \exp(j\theta t) \text{ and } I_t = I_0 \exp(j\theta t - \varphi) \qquad \text{Equation 3.4}$$

$$Z(\theta) = Z_0 \exp(j\varphi) = Z_0(\cos\varphi + j\sin\varphi) \qquad \text{Equation 3.5}$$

Equation for Z (θ) has two parts: real and imaginary. While plotting the real part on the X axis and the imaginary part on the Y axis, we come up with a "Nyquist Plot" as seen in Figure 3.4.

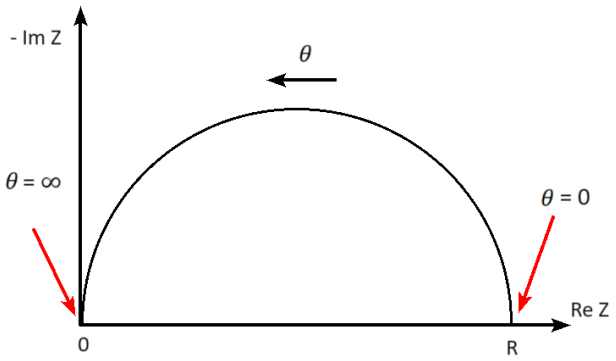

Figure 3.4. Typical Nyquist Plot.

One of the disadvantages of a Nyquist Plot is that we cannot see where the frequency values are indicated. In Figure 3.4, it is given Nyquist Plot for a simple one-time equivalent circuit with one resistor and one capacitor in parallel. In real case measurements, photoelectrode with electrolyte compose more complex circuits where we can measure EIS data and fit it with different circuit configurations. By comparing the semicircles measured from samples in similar conditions, one can find information about coating impedance and its charge-transport properties.

3.5.3 Incident photon-to-current conversion efficiency

IPCE is abbreviation for the incident photon-to-current efficiency measurements. IPCE shows percentage of incident photon numbers (n_p) on material that were converted to electrons n_e as a function of light wavelength. In other words, it is called external quantum efficiency. The following expression give IPCE:

$$IPCE = \frac{n_e}{n_p} = \frac{1240 * J}{\lambda * P}, \qquad \text{Equation 3.6}$$

where, J is photocurrent density at wavelength λ, P is intensity of used monochromatic light. IPCE gives information about which photon wavelengths of the solar spectrum are absorbed by the material and contribute to the photocurrent generation.

3.5.4 Absorbed photon-to-current conversion efficiency

APCE is abbreviation for the absorbed photon-to-current efficiency measurements. In other words, it is called internal quantum efficiency. The following expression give APCE:

$$APCE = \frac{IPCE}{light\ harvesting\ efficiency} = \frac{\frac{n_e}{n_p}}{(1-10^{-A(\lambda)})} = \frac{\frac{1240*J}{\lambda*P}}{(1-10^{-A(\lambda)})}, \qquad \text{Equation 3.7}$$

where, J is photocurrent density at wavelength λ, P is intensity of used monochromatic light, A is absorbance at specific wavelength. Light harvesting efficiency can be calculated using the UV-VIS spectra absorption data. APCE shows the quantity of light generated charge carriers that are donated to the creation of photocurrent per absorbed photon.

4. Improving PEC properties of magnetron-sputtered two-layer WO_3 photoanodes by IPIB irradiation

4.1 Focus of the Chapter

This chapter explores ways to enhance the photoactivity of WO_3 photoelectrodes for water-splitting purposes. We discovered that using intense pulsed ion beams (IPIB) irradiation of a nanosecond timescale on a two-layer (crystalline/amorphous) arrangement of WO_3 thin films can significantly improve its PEC activity. The IPIB irradiation resulted in the formation of polycrystalline and WO_3 structures resembling sponge shapes on the surface, leading to a greater active surface area for chemical reactions and light scattering in the irradiated samples. Consequently, the photocurrent production increased by about 80% at 1.23 reversible hydrogen electrodes (RHE).

4.2 Introduction

Currently, PEC water splitting is thought to be a potential way to meet the needs for renewable energy. As solar-light-based hydrogen manufacturing becomes a realistic option, it opens new opportunities for a variety of industry sectors (Dincer & Acar, 2015; Sazali, 2020). Nevertheless, further research is required to enhance its efficiency as it currently lags behind other renewable energy sources (Jia et al., 2016; K. H. Ng et al., 2021).
Tungsten trioxide, WO_3, is a well-studied wide band gap metal oxide semiconductor material. Through various modification techniques, this band gap can be changed from 3.2 eV to 2.5 eV (Kozlovskiy & Zdorovets, 2020; Mohamedkhair et al., 2021). WO_3 has the potential to operate as

a photoanode material for the oxygen evolution by absorbing sun energy and generating electron-hole pairs. However, it does have certain disadvantages, including insufficient charge separation, sluggish hole kinetics, and surface degradation brought on by the formation of peroxo-species (G. Zheng et al., 2019). Impurity doping, creating WO_3 composites, making heterostructures, and surface engineering might be effective ways to deal with such drawbacks (Kalanur et al., 2020; Markhabayeva et al., 2020; Y. Wang et al., 2013; Zych et al., 2022a). To study the photocatalytic effect of WO_3 based photoelectrodes depending on their shapes, tungsten trioxides in the form of nanorods, -fibers, and -plates, and wedge- or sheet-like materials were fabricated and checked (Chae et al., 2017; Fang et al., 2015; Jiao et al., 2011; Su et al., 2017; Zhou et al., 2017). As efficient strategies, surface and morphological treatments of photoelectrodes can enhance their performance (Samuel et al., 2020). Particularly, surface etching and passivating with other materials might promote charge carriers' mobility, decrease the overpotential of photoelectrodes, and accomplish photocatalytically improved material characteristics (Y. Liu et al., 2018). Additionally, utilizing annealing in diverse settings is an additional method employed to enhance the photocatalytic characteristics of different photoelectrodes. This is due to the substantial impact of annealing on the phase structures of materials (Kalanur et al., 2019; Roselló-Márquez et al., 2020). Modification methods such as laser beam treatment and ion beam irradiation can be employed at the time of fabrication or after depositions for changing opto-electrical, morphological, and phase-structural features (S. Ma et al., 2017; X. D. Zheng, 2019; X.-D. Zheng et al., 2018).

The correct band arrangement of photoelectrode interfaces with water splitting potential gives opportunity to substantially increase photocurrent production due to superior charge separation in several-layered heterojunctions. Furthermore, the PEC activity of photoanodes might be improved by employing 2D nanomaterials for WO_3 (Masoumi et al., 2022), by controlled texturing of material's facets (Le et al., 2021), making unassisted solar cell tandem architectures (Y. Wang et al., 2020), and as mentioned before, combining with plasmonic structures and by inducing oxygen vacancies.

In this work, we report a new technique for surface engineering of WO_3 photoanode that integrates concurrent surface modification and annealing for improving PEC characteristics. The application of intense pulsed ion beam (IPIB) irradiation leads to the formation of a porous WO_3 surface resembling a sponge, in conjunction with the subsequent annealing process. Fabricated photoanodes were checked for the morphology change, structure alteration, optical and PEC performance improvements. This new technique of surface modification gives an opportunity to

fabricate thin sponge-type coating with high crystallinity and porosity that has expanded chemically active area and boosted absorbance straight from amorphous coating.

4.3 The amorphous, crystalline, and two-layer WO_3 photoanodes synthesis and characterizations.

Sample Preparation. Initially, amorphous, crystalline, and two-layer WO_3 photoanodes were prepared on commercial fluoride tin oxide (FTO) substrates. The FTO (350 nm) substrates on glass were washed with ethanol in an ultrasonic bath prior to fabrication. Kurt Lesker magnetron sputtering system (W, Kurt J. Lesker, 99.95% purity, 2.00" diameter) was utilized for the fabrication of WO_3 reactively in DC mode and fixing oxygen/argon flow rates at 21/33 sccm. Fabrication was carried out with sputter power of 100 W, and the substrate holder was rotated at 20 rpm for the homogeneity of coatings. Base pressure of fabrication was 11.4 mTorr.
Firstly, amorphous WO_3 thin coatings were fabricated for 45 min. It is well known that sputtered WO_3 with magnetrons has an amorphous phase (B. Yang et al., 2020). Subsequently, fifty percent of the photoanodes underwent annealing on a hot plate at 500 °C for 20 minutes in ambient air to achieve a crystalline phase. Obtained amorphous and crystalline photoanodes were irradiated with IPIB by varying proton ion beam current densities starting from 10 A/cm^2 up to 32 A/cm^2. IPIB irradiation was carried out using the INURA accelerator at Nazarbayev University (Astana, Kazakhstan) (Kaikanov et al., 2016). The INURA ion accelerator has a pulsed-power design that utilizes less than 10 kW of total power. At the target, the beam achieves a maximum power density of up to 10 MW/cm^2. The accelerator's key specifications include an accelerating voltage range of 300 to 400 kV, a total beam current of 10 kA, and a beam pulse length of 100 ns (FWHM). When a single 100 ns pulse of ion beam irradiates the target, it initiates a rapid annealing process characterized by a heating phase that lasts a hundred nanoseconds, followed by a cooling phase that lasts for microseconds. Overall structure and characteristics of the accelerator are discussed more deeply in previous chapters.
Next, two sets of WO_3 photoanodes were produced, one subjected to irradiation and the other non-irradiated, each consisting of two layers with approximate thicknesses of 380 nm (comprising an amorphous top layer of about 120 nm and a crystalline bottom layer of approximately 260 nm). To create these, an amorphous WO_3 layer was formed on two FTO substrates, followed by a 30-minute synthesis, and subsequently annealed on a hot plate for 20 minutes in ambient air at 500 °C to induce a phase transition to the crystalline state. Then, on top

of that crystalline-phased WO_3 coatings, a second layer of amorphous-phased WO_3 coatings were sputtered for 15 min. The annealing and deposition processes were carried out under identical conditions for both FTO substrates. Next, we subjected one of the prepared two-layer WO3 photoanodes to irradiation with IPIB using a current density of 6 A/cm^2.
The Carl Zeiss Crossbeam 540 GEMINI II Scanning Electron Microscope (SEM), Rigaku Smartlab Automated Multipurpose Grazing Incidence X-ray Diffractometer (GI-XRD) (with an omega angle of 0.5), and Evolution 300 spectrophotometer were employed to examine the morphological, structural, and optical properties of the modified photoanodes.

PEC Characterization. For PEC (photoelectrochemical) properties checking, a three-electrode cell setup was employed where the two-layer WO_3 was used as the working electrode. To measure the PEC, we used a reference electrode of Ag/AgCl (3.5 M KCl) and a counter electrode made of Pt wire. The photocurrent generation of the photoanodes was measured in 0.1 M Na_2SO_4 (pH 7.2) electrolyte utilizing a potentiostat CHI660E and a PLS-EM solar simulator (100 mW/cm^2, AM 1.5). We converted the obtained potential to the reversible hydrogen electrode (RHE) scale using the following equation:

$$V_{RHE} = V_{Ag/AgCl} + 0.059 * pH + 0.205 \qquad \text{Equation 4.1}$$

where, $V_{Ag/AgCl}$ is the applied potential and 0.205 is the standard potential of the Ag/AgCl, KCl (3.5M) reference electrode. Electrochemical impedance spectroscopy (EIS) was performed with light exposure, employing an AC voltage amplitude of 50 mV at a DC bias of 0.68 V vs. RHE. The frequency range covered spanned from 0.01 Hz to 10 kHz. To fit the EIS data to a circuit model, we utilized the EIS Spectrum Analyzer software (Bondarenko, A.S. et al., 2005).

4.4 Irradiation of amorphous and crystalline WO_3 photoanodes

Initially, amorphous and crystalline WO_3 photoanodes were irradiated with IPIB. In Figure 4.1, the SEM images of WO_3 photoanodes on FTO substrate after irradiating with varying current densities (ranging from 10 to 32 A/cm^2) are presented. The SEM pictures of the crystalline photoanodes irradiated at 10 A/cm^2 ion beam current density (Figure 4.1a) showed no noticeable changes when compared to non-irradiated photoanodes. Therefore, it can be inferred that 10 A/cm^2 irradiation has minimal or no impact on the surface morphologies of crystalline-phase

WO_3 photoanodes. On the other hand, irradiating with ion beam current densities of 16 A/cm^2 and 26 A/cm^2 (4.1b and 4.1c) significantly altered the morphology of the initial crystalline coatings, resulting in a porous coating with unfilled spaces opening the substrate material beneath. Increasing the ion beam current density to 32 A/cm^2 had a similar impact on the photoanode, causing an expansion of the open spaces. However, when applied to amorphous samples, comparable ion beams current densities yielded distinct effects on morphology, as depicted in Figure 4.1e–h. After irradiation, all amorphous coatings exhibited a sponge-type morphological structure overall. With an increase in ion beam current density from 10 to 32 A/cm^2, the irregular shapes and sizes of the sponge-type morphology showed a proportional enlargement. It can be stated that IPIB irradiation leads to more significant morphology alterations on amorphous photoanodes than on crystalline ones.

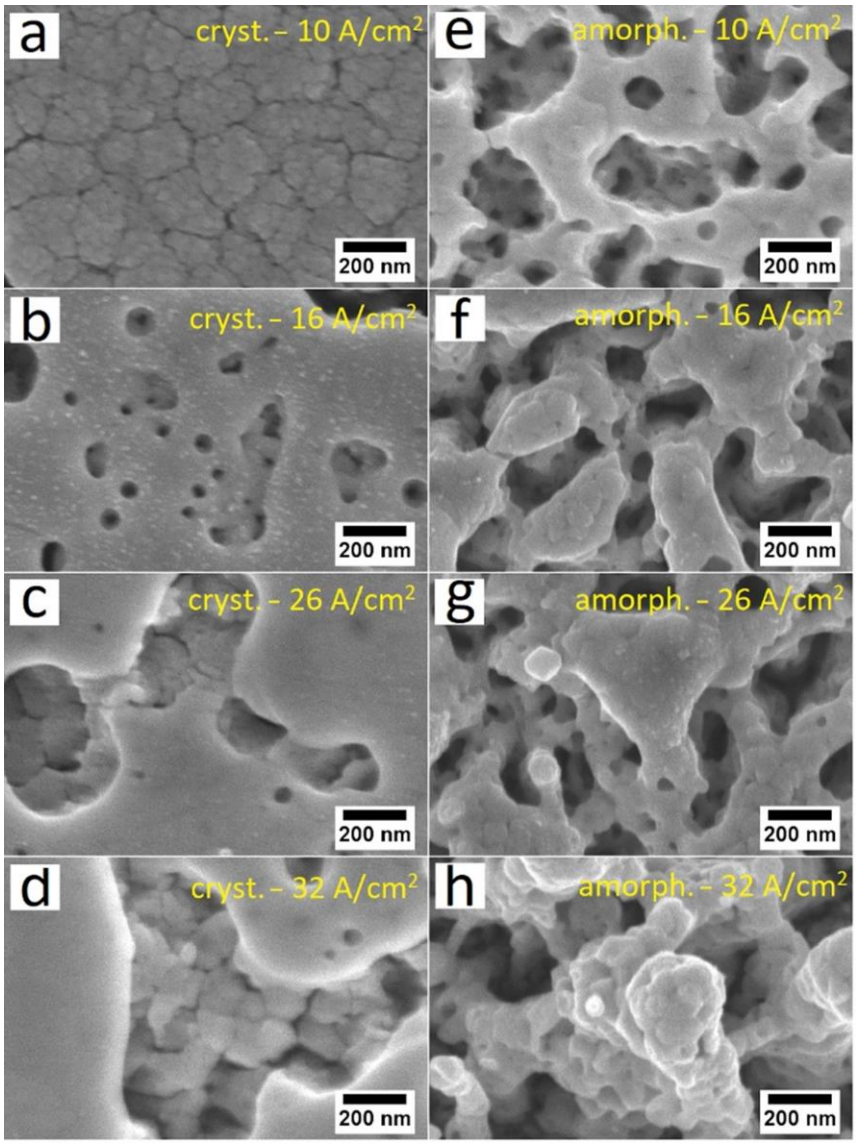

Figure 4.1. SEM images of the surface of crystalline (a–d) and amorphous (e–h) WO_3 thin films following ion beam irradiation at different current densities: (a,e) 10 A/cm^2, (b,f) 16 A/cm^2, (c,g) 26 A/cm^2, and (d,h) 32 A/cm^2.

Next, PEC properties of amorphous and crystalline samples were tested after irradiation with IPIB and investigated that rising ion beam current density decreases the photocurrent production of crystalline-phase WO_3 photoanodes, as can be seen in Figure 4.2. For the irradiated amorphous photoanodes, photocurrent production was not detected at any ion beam current density. Such behavior might be assigned to the creation of different defects in photoanode structure and forming of open spaces, where substrate is available to electrolytes and causes short-circuit condition during the linear sweep voltammetry (LSV) measurement.

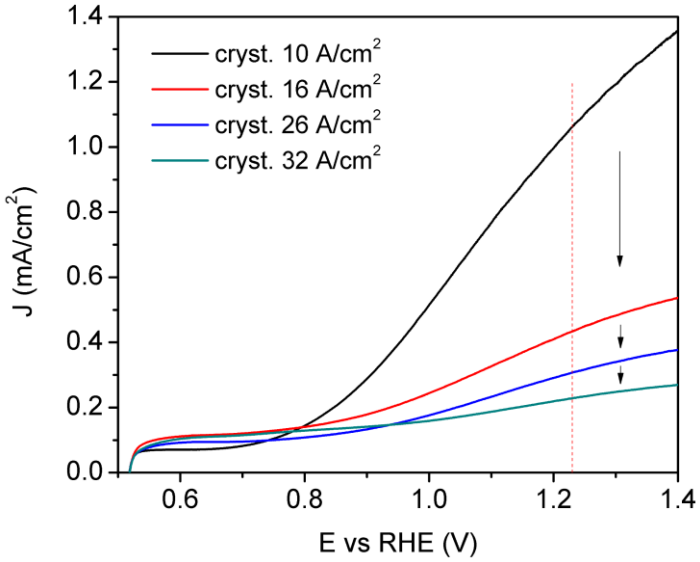

Figure 4.2 LSV curves of irradiated crystalline WO_3 thin films as the ion beam current density increases. The black arrows signify a decrease in photocurrent generation with higher ion beam current densities.

4.5 Irradiation of the two-layer WO_3 photoanode

As bare amorphous and crystalline WO_3 photoanodes do not show good photocatalytic properties after irradiation, it was proposed to create two-layer WO_3 photoanode that gives opportunity to avoid creation of open holes with increased absorbance. Two-layer photoanode consists of the top amorphous layer and bottom crystalline layer. It was revealed that as irradiating two-layer WO_3 photoanode with ion beam current density of 6 A/cm^2, crystalline bottom layer showed no morphological changes and top amorphous layer turned into sponge-type coating. Figure 4.3

represents the surface and cross-sectional SEM images of non-irradiated and irradiated two-layer WO_3 photoanodes, i.e. validating the presence of modification of top amorphous layer after 6 A/cm^2 irradiation.

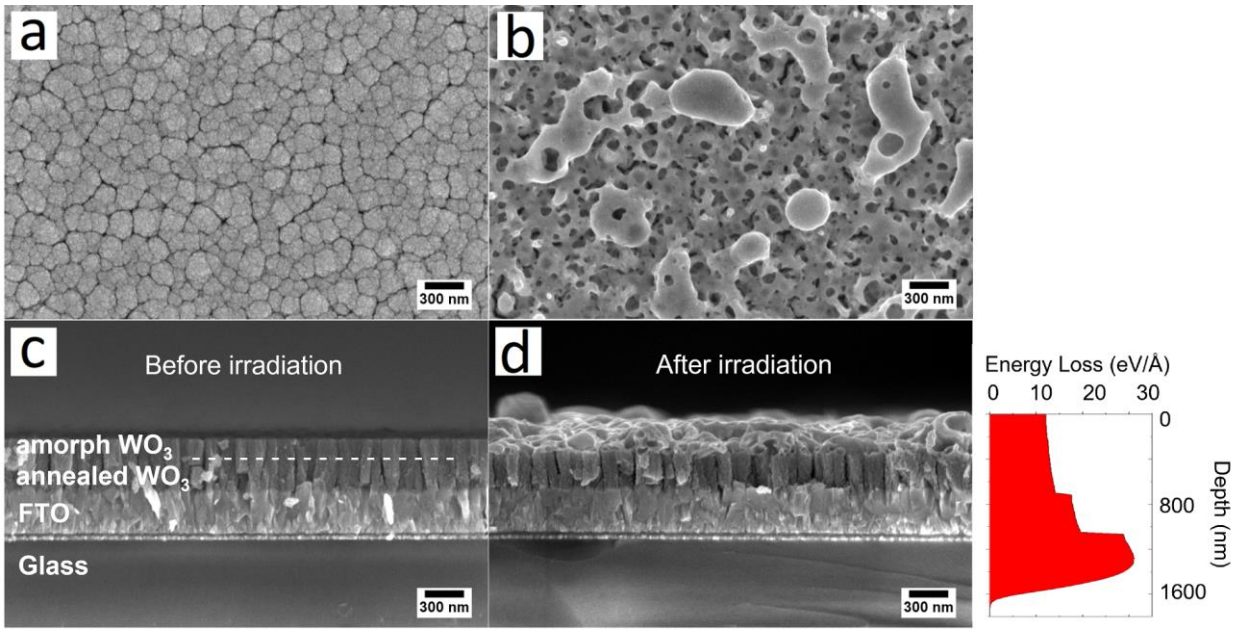

Figure 4.3. Surface SEM images depict (a) the non-irradiated and (b) the irradiated double-layer WO_3 at 6 A/cm^2, while cross-sections illustrate (c) the non-irradiated and (d) the irradiated double-layer WO_3 at 6 A/cm^2. The inset features the calculated energy loss cross-section profile of protons with an initial kinetic energy of 350 keV.

To facilitate a clear understanding of the influences of ion beam irradiating on WO_3-FTO-Glass material, the energy dissipation trajectory of a proton beam with a starting kinetical energy of 350 keV in the target material was determined using the SRIM (Stopping and Range of Ions in Matter) open-source program (http://www.srim.org/, accessed on May 25, 2022). The outcomes of these calculations are given in the inset of Figure 4.3. Computations disclosed a ~1600 nm proton beam distance (penetration depth) in a two-layer WO_3 on FTO photoanode material, which demonstrates that the energy of the IPIB is consumed mainly in the vicinity of the surface slab of target material. Consumed energy by the photoanode during the irradiation brings to super-fast heating of the material's surface layer and its consecutive fast cooling, coming up in the morphological changes of the top amorphous surface layer and its crystallization.

The morphological SEM view of non-irradiated photoanode possesses granular microstructure; yet, after IPIB modification, the surface turns into a sponge-type microstructure with open holes that has random distribution. Plus, as can be seen in Figure 4.3-b, the creation and agglomeration of some WO_3 island clusters on the surface of modified photoanode. Figures 4.3-c, d present a

SEM cross-section view of the photoanodes prior and after the modification with irradiation and confirm the creation of sponge-type morphology and clustering. The modified two-layer photoanode coating in Figure 4.3-d obviously displays that the underneath crystalline layer stays unaltered after irradiating with IPIB.

GI-XRD mode was utilized for determination of the structural characteristics of two-layer WO_3 photoanodes prior and after irradiation. Figure 4.4 displays the related GI-XRD results. The layer underneath possesses crystalline-phase since it was experienced to annealing process on the hot-plate after fabrication, and top coating carries amorphous phase. The red line in Figure 4.4 demonstrates the domination of a monoclinic phase of WO_3 (PDF2, #01-075-2072) for the underneath layer that was subjected to annealing. On the other hand, it is seen that modification by irradiation turned phases of both layers of two-layer WO_3 (amorphous /crystalline) into dominated tetragonal (PDF2, #01-089-1287), as can be seen in Figure 4.4 (blue line).

The intensity peaks from the FTO substrate which are given by black line are less detectable due to the GI-XRD mode, because it measures only the extremely thin top layer of the coating. It was observed that peak (020) of the monoclinic phase disappeared after modification with IPIB. It was additionally checked that one-layer amorphous photoanode indeed crystallizes after IPIB modification at 6 A/cm^2 ion beam current density.

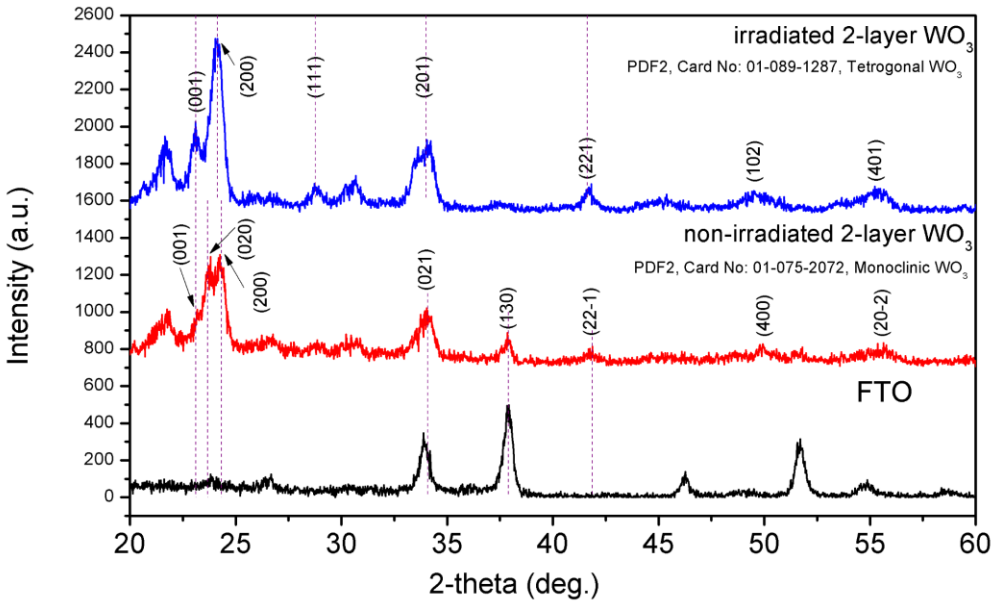

Figure 4.4. GI-XRD patterns for two-layer WO_3 thin films are presented for both non-irradiated and irradiated samples. The lower plot displays the GI-XRD lines corresponding to the FTO substrate.

GI-XRD results showed that it does actually turn into a crystalline phase of WO_3 with the dominance of tetragonal structure, as was depicted in Figure 4.5. As a result of the super-fast annealing caused by IPIB irradiation, the top and bottom layers of our two-layer photoanode crystallize with a dominant tetragonal phase. The GI-XRD peak-signals in Figure 4.5 for amorphous photoanode (blue line) are attributed to peaks of FTO material. High-resolution GI-XRD lines in Figure 4.6 proves the amorphous phase of as-prepared WO_3 photoanode, and it is in good agreement with the prior reports (B. Yang et al., 2020).

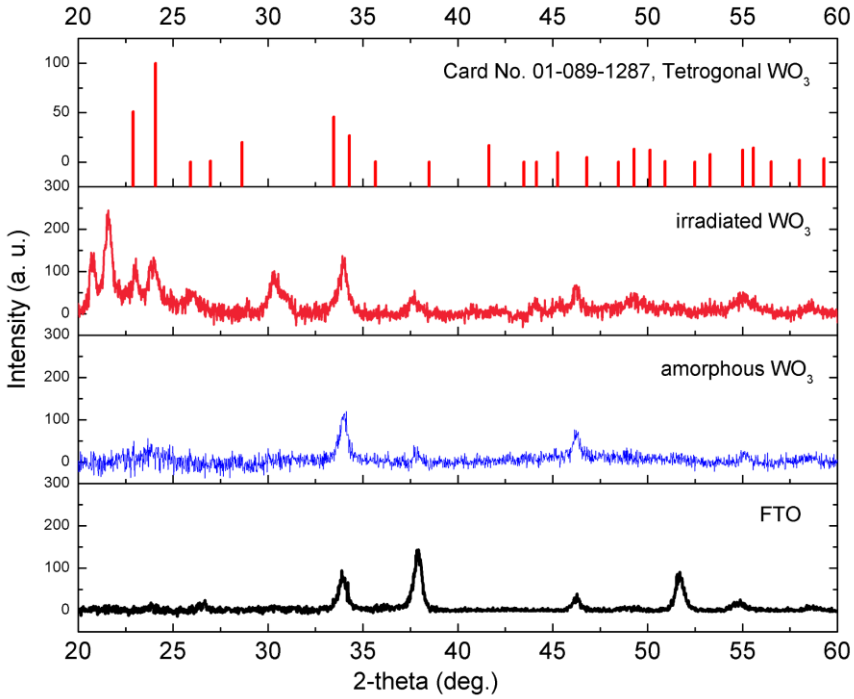

Figure 4.5. GI-XRD patterns of a WO_3 thin film, initially amorphous, both pre- and post-irradiation with an ion beam current density of 6 A/cm^2.

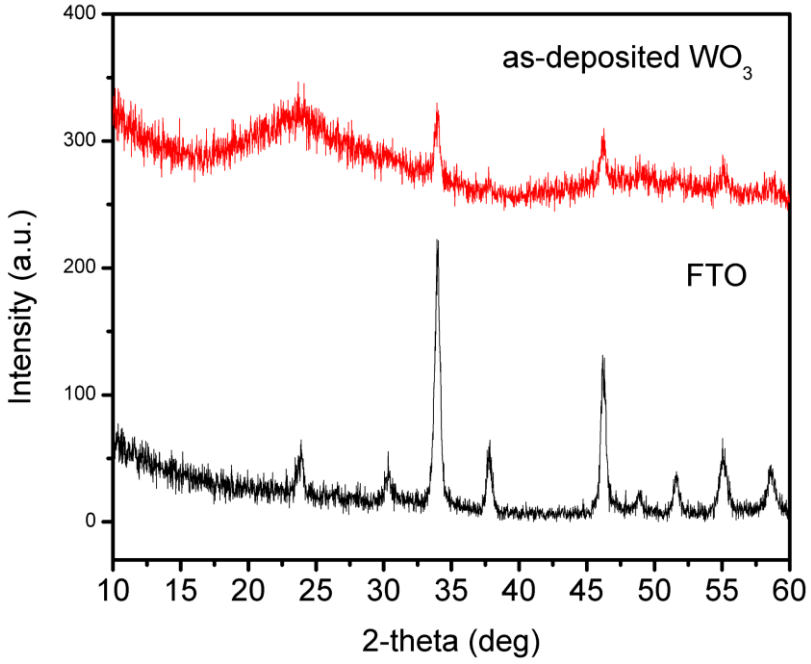

Figure 4.6. GI-XRD patterns of amorphous WO_3 and FTO substrates performed in high-resolution mode.

Figures 4.7-a, b show the absorption spectra and Tauc plot analysis of non-modified and modified two-layer WO_3 with the IPIB irradiation, correspondingly. Clearly, as shown in Figure 4.7-a, the irradiation modified two-layer photoanode possesses better absorbance than that of non-irradiated photoanode. It can be interpreted by the trapping of electrons in created oxygen vacancies, which appeared after modification with IPIB (Popov et al., 2018). Effect of light scatter along the interfaces of sponge-type porous inclusions and light capturing on the ion beam caused point defects of interstitial oxygen intralattice lead to absorption enhancement. The Tauc technique was utilized for analyzing the band gap of the photoanode after modification with irradiation (Makuła et al., 2018). Tauc plot results for both photoanodes in Figure 4.7-b exhibit the similar 3.35 eV band gap prior and after the modification with irradiation.

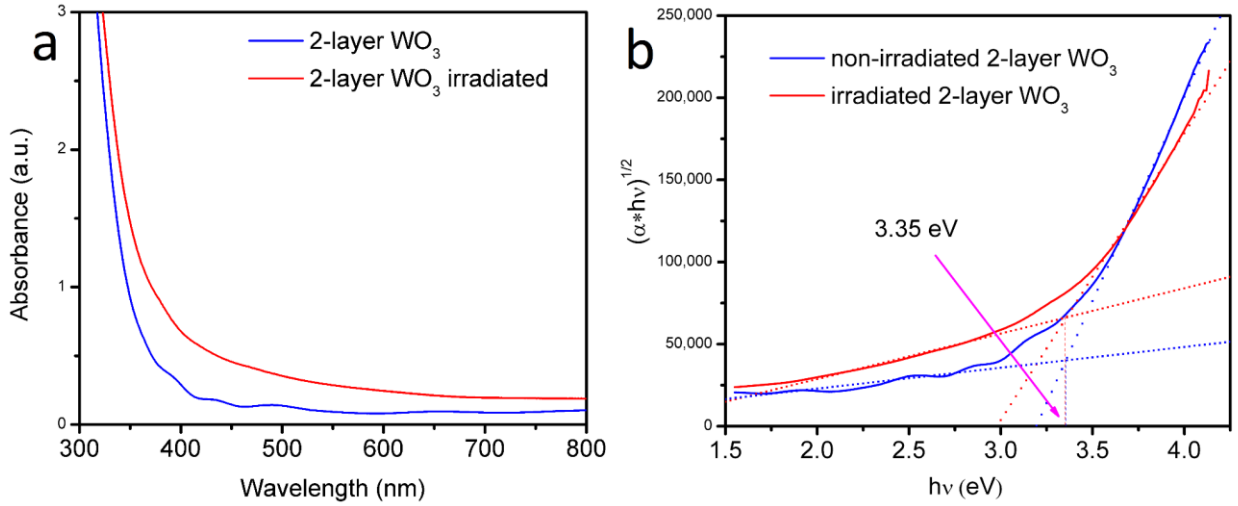

Figure 4.7. (a) Absorbance and (b) Tauc plot of two-layer non-irradiated and irradiated WO_3 photoanodes. Band gap estimations are marked.

The surface compositions of non-irradiated and irradiated samples were further analyzed by XPS technique. XPS survey spectra in Figure 4.8 confirm appearance of O1s, W4f, W4d, C1s peaks associated with oxygen, tungsten, and carbon elements. The C1s peak appeared at 285 eV due to XPS scanning of surface of samples without cleaning with ion etching.

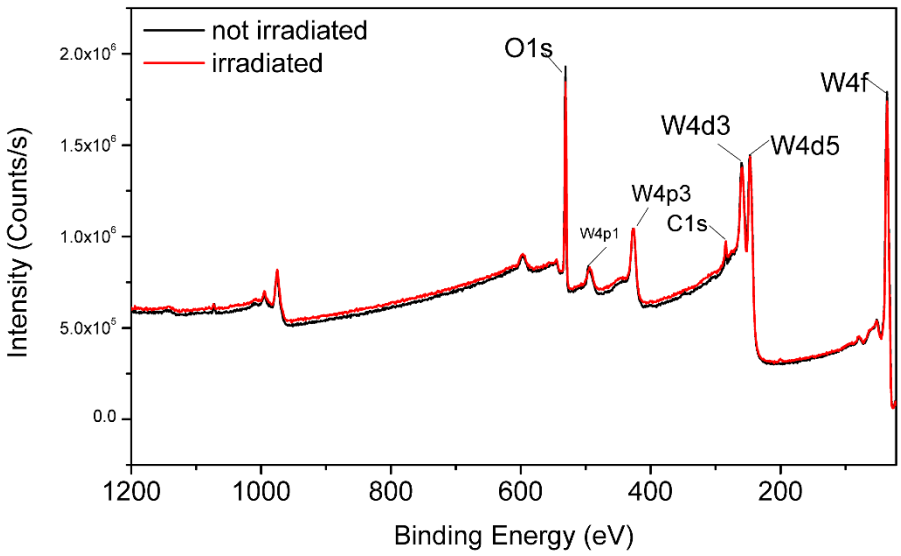

Figure 4.8. a) XPS survey spectra of non-irradiated and irradiated two-layer WO_3 samples.

The deconvolutions of the elements are given in Figure 4.9 for W4f and O1s. High resolution W4f core peak in Figure 4.9-a shows that surface layer of non-irradiated sample has peaks at 38.43, 36.18, 37.79, 35.15 eV corresponding to W^{6+} (4f5/2), W^{6+} (4f7/2), W^{5+} (4f5/2), W^{5+}

(4f7/2) oxidation states, respectably. For irradiated sample in Figure 4.9-b, W4f deconvoluted peaks located at 38.1, 35.72, 37.25, 34.73 eV which correspond to W^{6+} (4f5/2), W^{6+} (4f7/2), W^{5+} (4f5/2), W^{5+} (4f7/2) oxidation states, respectably. Peaks located at 34.02, 31.75 for non-irradiated sample and at 33.79, 31.52 for irradiated sample can be assigned to W^{x+} oxidation state (Mohamedkhair et al., 2020). In report Ref. (Xie et al., 2012), it was reported that the W^{x+} state is an intermediate state between W^{4+} and W^{0}, which might arise from the W^{3+}, W^{2+} or W^{1+} oxidation states. W^{x+} may be resulted from the ions of tungsten with incomplete unbroken ions of oxygen and W-W bonds. Authors conclude that it is difficult to attribute the transitional chemical state to a specific formal oxidation state. All deconvoluted peaks for irradiated sample have shifted to the lower binding energies compared to non-irradiated sample. The reason for that might be increased oxygen vacancies. Since, decreasing binding energy to lower energies means decrease of conduction electron concentrations and more oxygen vacancies. Additionally, increased ratio of W^{5+} to W^{6+} indicates presence of more oxygen vacancies in samples (Jaiswal & Choudhury, 2022). In our case, irradiated sample has ratio of 1.64 compared to non-irradiated sample with W^{5+} / W^{6+} ratio of 1.1, consequently, irradiated sample exhibits more oxygen vacancies. Areas were calculated by integrating deconvoluted peaks of core W4f. Calculated table is given in Appendix A1.

Figure 4.9-c and 4.9-d show deconvoluted O1s high resolution peaks. Non-irradiated sample has peaks located at 531.24 and 532.29 which can be assigned to the lattice oxygen (O_L) and oxygen vacancies (O_V), respectively (Mohamedkhair et al., 2020). Similar behavior is observed for the irradiated sample at 530.96 eV (O_L) and 531.75 eV (O_V) of deconvoluted O1s peaks. It can be observed that the area under O_V for the irradiated sample increased to 2.3 % compared to the non-irradiated sample. It might be assigned to the increasing oxygen vacancies on the surface layer of two-layer WO_3 sample after the irradiation process which is beneficial for enhancement of photocatalytic activities of the surface layer.

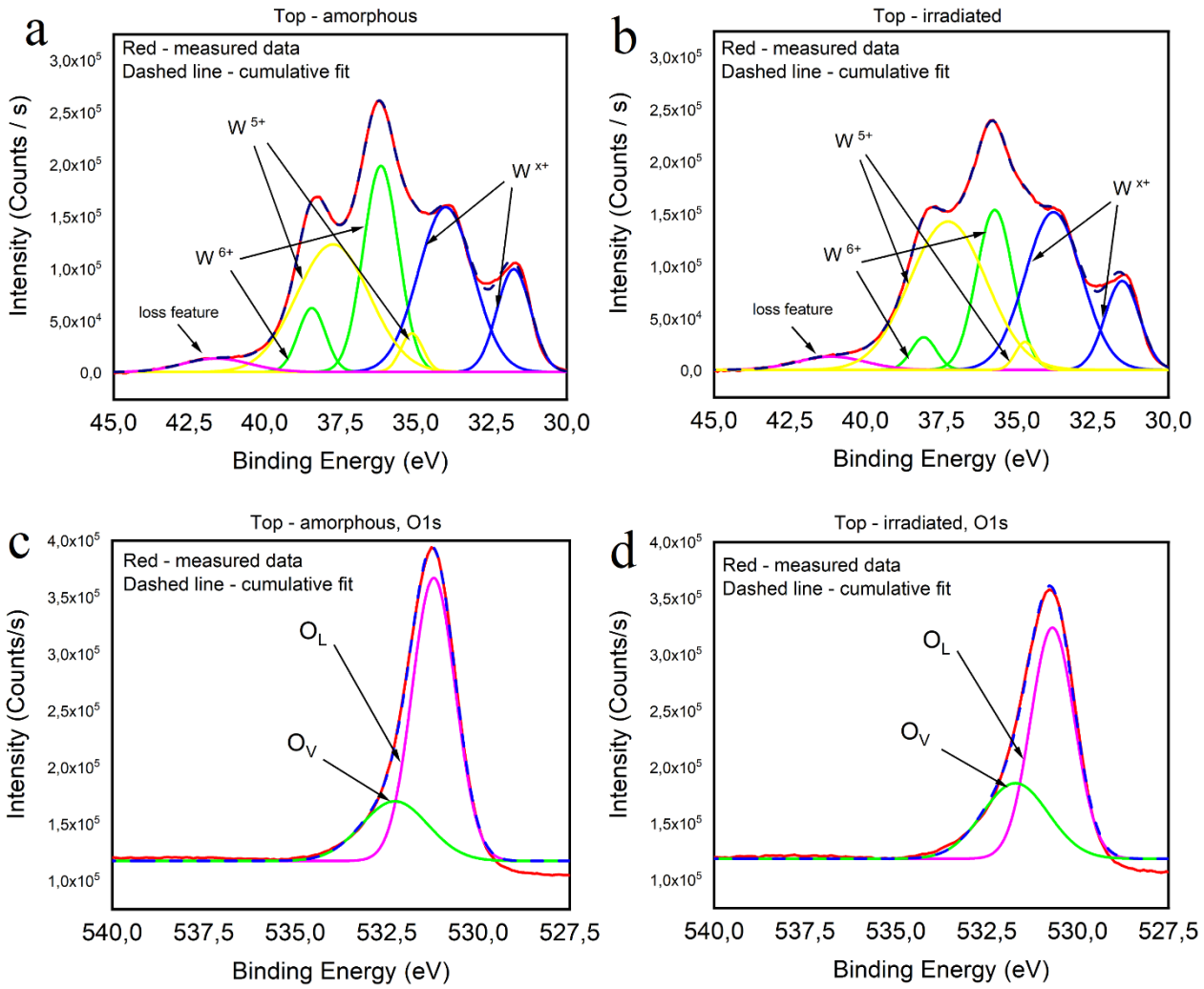

Figure 4.9. a) XPS high resolution spectra of core W4f and O1s peaks of non-irradiated and irradiated two-layer WO_3 samples.

The EIS method was implemented for the determination of the charge transport characteristics of modified and non-modified two-layer photoanodes, as seen in Figure 4.10. EIS measurement results show shorter semicircle radius for the modified photoanode compared to non-modified, i.e., it indicates that the irradiated photoanode is more favorable for the charge transport. Surface changes caused by irradiation promote the charge transfer characteristics of the photoanode, i.e., sponge-type morphology assists in better hole transferrance to the WO_3/electrolyte interface and raises the surface-active areas. Additionally, light capturing in such morphology improves the better electron-hole pair creation by means of enhanced photon trapping.

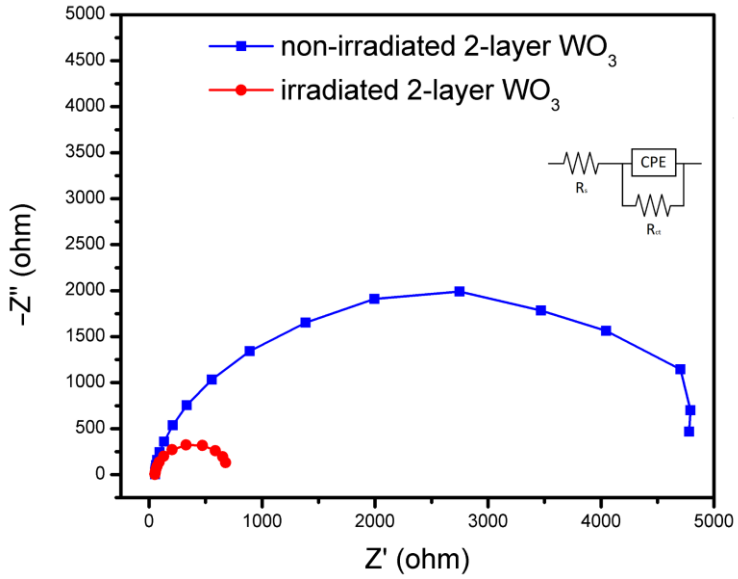

Figure 4.10. EIS Nyquist plots of irradiated and non-irradiated two-layer WO_3.

LSV measurement results are shown for modified and non-modified photoanodes in Figure 4.11. Additional chopped LSV measurements in Figure 4.12 validates that the obtained photoanodes are photocatalytically active. Bare WO_3 showed 0.32 mA/cm^2 photocurrent at 1.23 RHE, whereas for irradiated two-layer WO_3 photocurrent was 0.58 mA/cm^2. Observed ~80 % increase in the photocurrent generation of modified sample related to non-modified sample might be assigned to the several factors. Firstly, sponge-type morphology of photoanodes caused by irradiation may act as light-capturing architecture, increasing absorption. Absorption might be further increased due to light seizure by point defects located in the oxygen sublattice (Popov et al., 2018). In the second place, modification induced by ion-photoanode interaction might increase the active area of the chemical surface at photoanode/electrolyte interface. Thirdly, IPIB modification turns an initial top amorphous WO_3 into crystalline-phased material. It is well known that the crystalline phase of WO_3 is more favorable for PEC application than amorphous (Valerini et al., 2016). Consequently, modification with IPIB of WO_3 photoanode might be recognized as one of the techniques for making materials with good porosity and crystallinity with enhanced PEC properties.

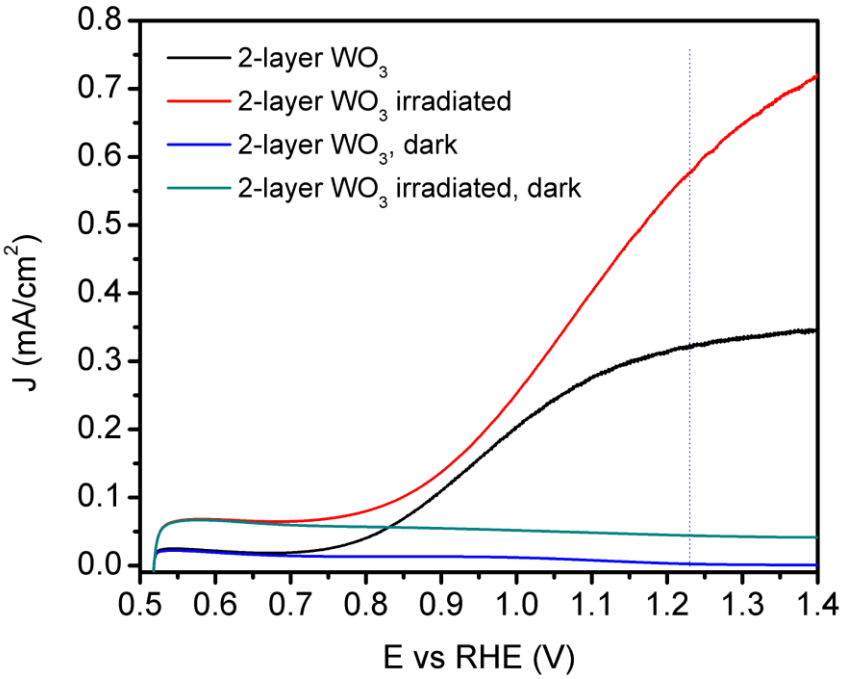

Figure 4.11. LSV measurements of two-layer WO_3 prior and after the irradiation with IPIB of 6 A/cm^2 ion beam current density.

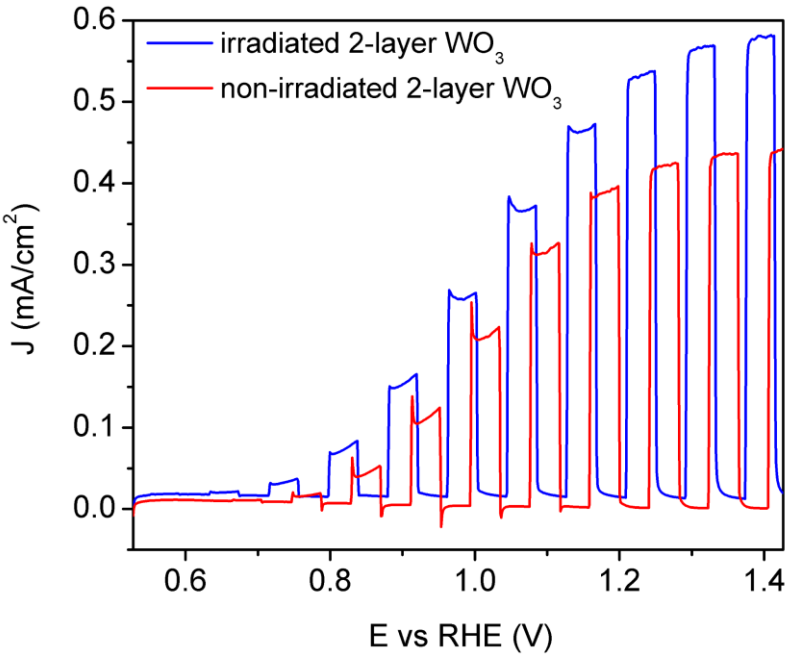

Figure 4.12. Chopped LSV measurements of two-layer WO_3 prior and after the irradiation with IPIB of 6 A/cm^2 ion beam current density.

Generally, modification with ion beam irradiation is broadly utilized for property changing of various materials (X. Wang et al., 2020). Ion beam irradiation, in fact, can have several

influences on target materials such as temperature rise, doping with ions, displacements in atomic range, and other changes in material. Ion irradiation in continuous mode which has less current density is broadly applied for the tuning of the electrical, morphology, and structure characteristics of nanomaterials. For instance, in Ref. (X.-D. Zheng et al., 2018), WO_3 coatings were modified with irradiation using 190 keV Ar+ ions with current densities of between 1 and 2 $\mu A/cm^{-2}$. It was presented that morphology change (pore creation) emerges when the Ar+ ion beam fluence of 10^{17} ions·cm^{-2}. As for IPIB, the irradiating of nanomaterials with very short and high intensity pulses leads to a very quick and powerful energy transport to the surface part of the nanomaterial. In our experiment employed IPIB lasts for 100 nanoseconds and typically delivers a fluence of almost 10^{12} protons·cm^{-2} in a single pulse. This results in an ion rate reaching up to 10^{19} protons·cm^{-2} per second and relates to a power density of 1 MW/cm^2. Mentioned high power density delivered to the upper surface thin slab of the material lead to the quick temperature rise. This may be used to generate warm dense matter states, notably in the field of high energy density physics, with increased beam intensity (Stepanov et al., 2018). For the usage in materials science, the fast-heating annealing process might be utilized for the change of surface vicinity of the bulk nanomaterials (X. Ma et al., 2014). The focus of this chapter is studying effect of IPIB irradiation with various ion beam current densities for the beneficial changes of WO_3-based photocatalytic electrodes. As ion penetration is fast, the fluence needed for pulsed irradiation (10^{12} ions·cm^{-2}) is extremely reduced in comparison to continuous irradiations, which may have a fluence of more than 10^{16} ions·cm^{-2}.

4.6 Conclusion of the chapter

In conclusion, the chapter presents a novel technique for making two-layer WO_3 coating with good porosity and boosted PEC characteristics. Modification of two-layer WO_3 photoanode with one pulse of ion beam creates a photoelectrode with sponge-type crystalline-phased surface layer with increased light trapping and improved charge transfer characteristics. We showed that photocurrent generation was enhanced to ~80 % due to the active surface area increase and better light capture. It is still a challenge to stabilize the irradiation-modified WO_3-based photoanode and can be addressed in future works. Suggested method opens a new route for the usage of IPIB irradiation for the modification of photocatalytic nanomaterials to increase their PEC properties.

5. Shape tuning of a thin silver coating into spherical nanoparticles through the process of solid-state dewetting under the influence of high-current pulsed ion beam irradiation.

5.1 Focus of the chapter

Plasmonic metal NPs play a crucial role in many application areas such as energy harvesting by solar PV devices, hydrogen production using PEC photoelectrodes, etc. In this chapter we study shaping of silver (Ag) nanoparticles from initially prepared Ag thin films on fused silica substrates through solid-state dewetting caused by intense high-current pulsed ion (proton) beams (IPIB) irradiation. The impact of IPIB was investigated by altering ion beam current densities and the number of irradiation pulses. Samples modified by irradiation with IPIB were compared with samples annealed by an ordinary RTA system. IPIB modification makes it possible to heat nanomaterials at super-fast speed (more than 10^9 K/s) with cool down times occurring in microseconds. This feature supplies a super-fast annealing leading to the solid state dewetting mechanism. Our experimental outcomes show that irradiated Ag NPs have more spherical shape relative to RTA modified Ag NPs.

5.2 Introduction

Metal NPs such as gold, silver, copper and their thin coatings have been shown as outstanding structures for light control. This is made possible by their strong localized surface plasmon resonance (LSPR) and surface plasmon polariton (SPP) properties (Farhang et al., 2013; Fathima et al., 2021). Noticeably, Ag NPs and coatings extensively used in many applications: bacteria treatment (Patil et al., 2019), antimicrobial agent (Tehri et al., 2020), sensing of various gasses (Kalai Priya et al., 2021), for sensing by surface enhanced Raman spectroscopy (Malik et al., 2022), etc. as well as plasmonic usage (Belessiotis & Kontos, 2022). As was reviewed in previous chapters, morphological and optical properties of Ag NPs in those reports strongly depend on NPs' size, shape and concentrations.

Various methods were invented to fabricate Ag NPs (Ankudze & Neglo, 2022). Solid state dewetting is a practical straightforward method in which metal coatings are fabricated on substrate material and heated. Thin metal coatings transmoform into small-scale islands or particles due to temperature rise. As a result of minimization of surface energy, during the annealing, arrays of Ag NPs form well adhered to the substrate. Solid state dewetting of metal

coatings into isolated NPs or islands occurs through the diffusion on the surface of the substrate at lower temperatures than melting. Reasons for that are the meta-stable state in which nanomaterials exist due to their high surface to volume ratio and acting tension forces on the surface (Leroy et al., 2016; Thompson, 2012). Ag is vulnerable to dewetting as it does not attach well to many substrate materials. In every step of fabricating Ag NPs by solid state dewetting, it is possible to manage size, shape, and concentration. The characteristics of Ag NPs depend on the heating criteria such as thickness of as-deposited coating (Badán et al., 2022), heating temperature (Gangwar & Agarwal, 2021), fixed temperature hold period (Badán et al., 2022), substrate type (wetting ability and surface roughness) (Araújo et al., 2016; Bhalla et al., 2019; Hooshmand et al., 2016) and rate of temperature rise (Araújo et al., 2018).

Usually, the annealing procedure is done by utilizing the conventional tube furnace operated for a long period of time (more than one hour). RTA is a fast-annealing method which has relatively less annealing time due to rapid temperature increase properties (up to 150 °C/s). Using RTA for the annealing of Ag thin films into NPs at high temperature ramps leads to the fabrication of more homogeneous sized particles and helps to decrease concentration of small particles (Araújo et al., 2018; Bai et al., 2014).

In the current chapter, we investigated solid state dewetting of magnetron sputtered Ag coatings into the NPs collections caused by super-fast annealing with temperature rising ramps of ~10^9 K/s. This super-fast annealing is obtained by the IPIB induced modification occurring within 100 ns and followed by μs cooling (Kaikanov et al., 2021).

Morphological changes, structural evolutions, and shape formations of Ag NPs on fused silica glass substrates fabricated using IPIB were compared with the properties of conventional RTA modified samples. We revealed that super-fast IPIB irradiation brings to the formation more spherical in shape Ag NPs that can be utilized in plasmonic applications.

5.3 Experimental part

Preparation of Ag thin coatings. The Kurt Lesker magnetron sputtering system chamber was loaded with fused silica (FS) substrates, which had been cleaned in an ethanol using ultrasonic bath for 15 minutes. The chamber's base pressure was then 3-5 * 10^{-7} Torr. Using an Ag target (99.99%) with a diameter of 2 inches, Ag coatings were fabricated at room temperature. At a distance of 13 cm, an Ag target was deposited in the perpendicular direction to the substrate plane. Sample fabrication was done in an atmosphere of Ar gas at a pressure of 10 mTorr in the

chamber. Applied power to the target was 5 W, while substrate rotation speed was 20 rpm to ensure uniformity of the coatings. According to measurements made from cross-sectional SEM images, entire Ag coatings had a thickness of 8–10 nm and deposition time was 4.5 min.
A Rigaku SmartLab Automated Multifunctional Grazing incidence X-ray diffractometer (GIXRD) was used for the phase-structure study using CuKa irradiation at a wavelength of 0.1541 nm. Carl Zeiss Crossbeam 540 GEMINI II scanning electron microscope (SEM) and SmartSPM 1000 atomic force microscope (AFM) were used to capture surface and surface morphology pictures of the materials. The optical characteristics were identified with the use of the Evolution 300 UV-VIS spectrometer.

Modification of Ag thin coatings with IPIB and RTA. Samples were prepared through a solid-state dewetting procedure using IPIB annealing and RTA. RTA modification was carried out in the Ar gas environment at 1 L/min flow rate and temperature rising rate of 10 °C/s till the maximum temperature, after which it was instantly allowed to cool down to room temperature. Those maximum temperatures range from 600 °C to 1000 °C (with a step of 100 °C).
The modification of Ag coatings through intense pulsed ion beam (IPIB) was carried out by adjusting current densities of ion beams and the number of irradiation pulses. The Innovative Nazarbayev University Research Accelerator (INURA) system was employed for irradiation, utilizing a 100 ns (FWHM) proton (H+) beam. The specifications of the INURA pulsed ion accelerator include an accelerating voltage of up to 400 kV, a total beam current of 10 kA, a beam pulse duration of less than 100 ns (FWHM), a beam diameter of approximately 5 cm, and a beam composition consisting mainly of protons with a minor component of carbon ions (90/10). The varied IPIB beam current densities and the corresponding number of pulses for each sample are presented in Table 5.1.

Table 5.1. IPIB current densities and number of pulses used for samples irradiation.

Sample #	Number of pulses	Beam current density, A/cm2
1	1	10
2	1	20
3	1	30
4	1	40

5	1	60
6	2	10
7	3	10
8	4	10

5.4 Results and discussion

Figure 5.1a exhibits the SEM picture of as-prepared Ag coatings prior to modifications. Initial Ag coatings show granular microstructure with open holes, because 8-10 nm Ag coatings are not packed enough to assemble homogeneous thin coating. In common, while Ag coatings are fabricated on glass substrates by sputtering, they pursue several steps of Volmer-Weber growth mode (Bulíř, 2011). Initially, diffusion of incident ions happens on the material and followed by the nucleation to create initial-stage tiny islands. Then, those tiny islands become larger by merging. Those synthesized large irregular shaped islands coalesce to become bulk thin films. Figures 5.1b-5.1e represent SEM pictures of the Ag NPs obtained by irradiating as-deposited samples with IPIB varying number of pulses (from 1 to 4) and fixing ion beam current density at 10 A/cm^2. Figures from 5.1f to 5.1j show SEM pictures of irradiation induced samples modified by varying ion beam current densities from 10 to 60 A/cm^2.

All obtained samples exhibit fine circular NPs structures of various size distributions. Previous reports of Ag NPs dewetting confirm that Ag thin films of several nanometers turn into irregular islands at low temperature values, whereas at high temperature annealing they get circular shapes (Bhattacharyya et al., 2009; Kunwar et al., 2017). But still, we discovered fine circular shapes from all our obtained Ag NPs. We maintain that IPIB modification with 10 A/cm^2 induces high temperature annealing which is high enough to create fine circular NPs. The parameters of IPIB caused modification procedure: irradiating ions (H^+ with up to 400 keV energies) go through the substrate material into the 2-3 micrometers depth. Consequently, kinetic energy of the incoming ions are delivered to the target material surface by raising its temperature in a time period of ~100 ns (ion striking pulse time) (Kaikanov et al., 2020). The heated surface layer then quickly cools down in a matter of microseconds by transmitting the thermal energy deeper into the substrate. In general, we are certain that the substrate surface conducts temperatures high enough for circular

NP creation during the dewetting procedure despite the annealing process being extremely quick, with a heating time of around 100 nsec and a cooling time of only a few microseconds.
SEM pictures in Figure 5.1 and distribution of their related sizes in Figures 5.2a and 5.2b exhibit that all irradiation modified Ag NPs possess size variation from 20 nm to 180 nm and result in double-peak histograms. Double-peak histograms show that two specific types of NPs prevail: small NPs (with diameters of less than 40 nm) and large NPs. Average diameter of particles shows slight increase with the increasing IPIB irradiation pulse numbers (identified using ImageJ free program from surface SEM pictures). Such creation of energetically preferable larger particles resulted from the influence of extra irradiation that forces particles to aggregation and shapes recreation. Average particle size increment appeared with decreasing of small particle numbers and decreasing of whole NPs concentration (Figure 5.2a).

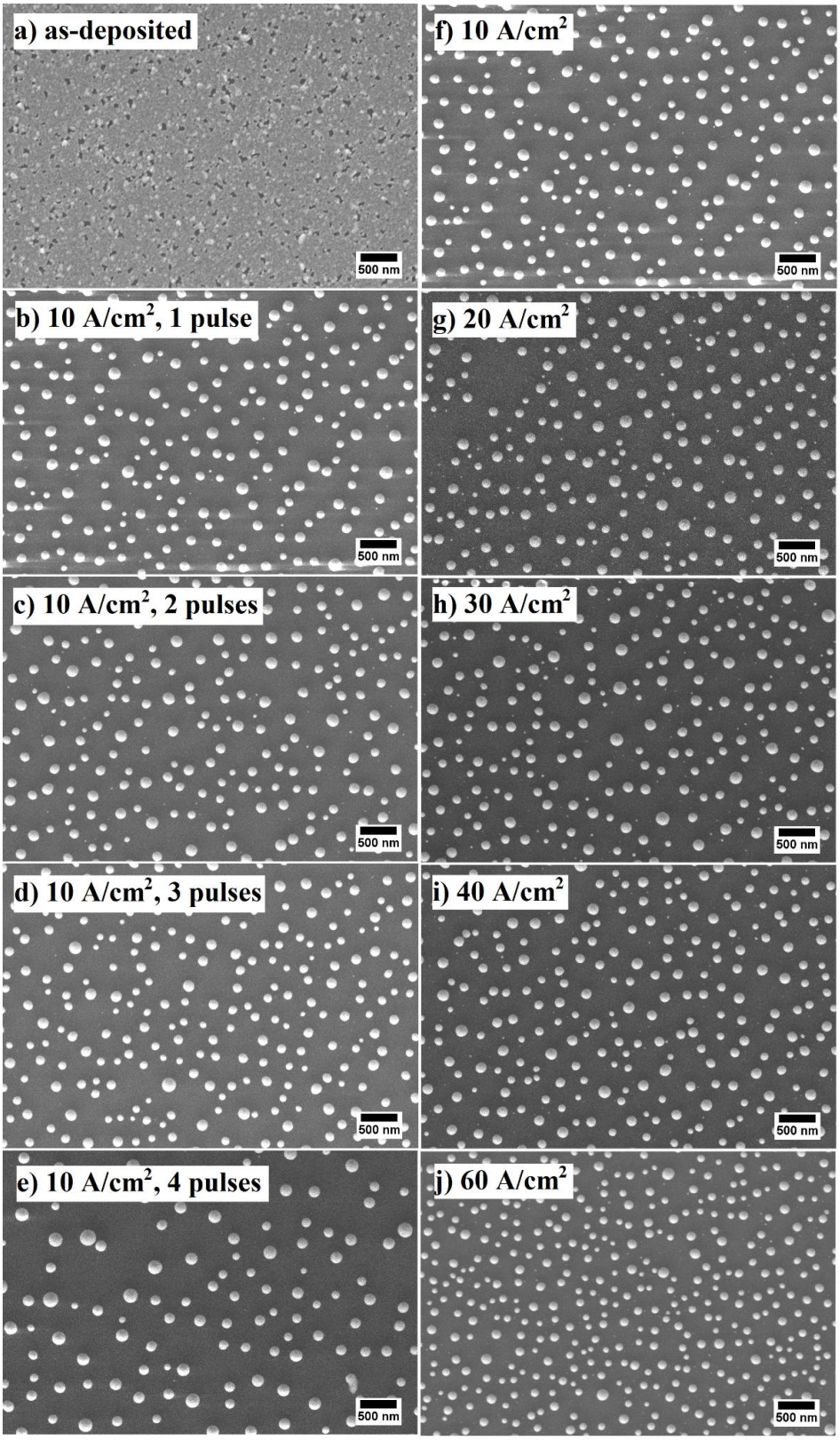

Figure 5.1. SEM images of the Ag coating before and after intense pulsed ion beam (IPIB) irradiation. a) Represents the as-deposited non-irradiated sample. For the irradiated samples, b-e) depict various stages of IPIB irradiation with an ion beam current density of 10 A/cm^2 and different pulse numbers: b) 1 pulse, c) 2 pulses, d) 3 pulses, e) 4 pulses. f-j) show samples

irradiated with a single pulse of IPIB at various ion beam current densities: f) 10 A/cm^2, g) 20 A/cm^2, h) 30 A/cm^2, i) 40 A/cm^2, j) 60 A/cm^2. It's important to note that images b) and f) are identical.

We observe lessening of the number of smaller NPs as current density of ion beams increases. We see a rapid fall of average particle diameter and corresponding rise of NPs concentration at 60 A/cm^2 current density of ion beams (Figures 5.2b and 5.3b). The reason for such behavior might be enhanced substrate roughness resulting from IPIB modification. Previous works confirm that substrate material roughness has a huge impact on the formation of NPs and their shape, morphology (Araújo et al., 2016). The diffusion of Ag atoms on the surface and their coalescence into the bigger Ag NPs are inhibited by increasing substrate roughness. Our experimental results show that IPIB modification increases the surface roughness of the FS substrate.

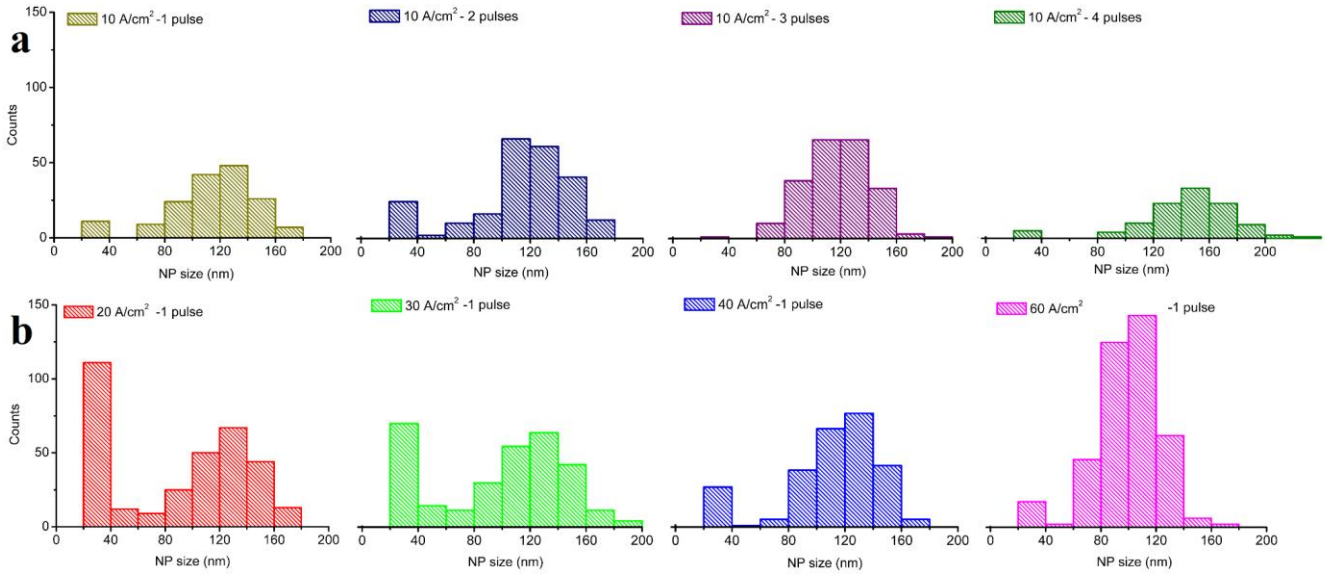

Figure 5.2. Histograms illustrating the distribution of diameters for annealed Ag nanoparticles, where a) represents irradiation with different numbers of IPIB pulses, and b) represents irradiation with a single pulse of IPIB at varying ion beam current densities.

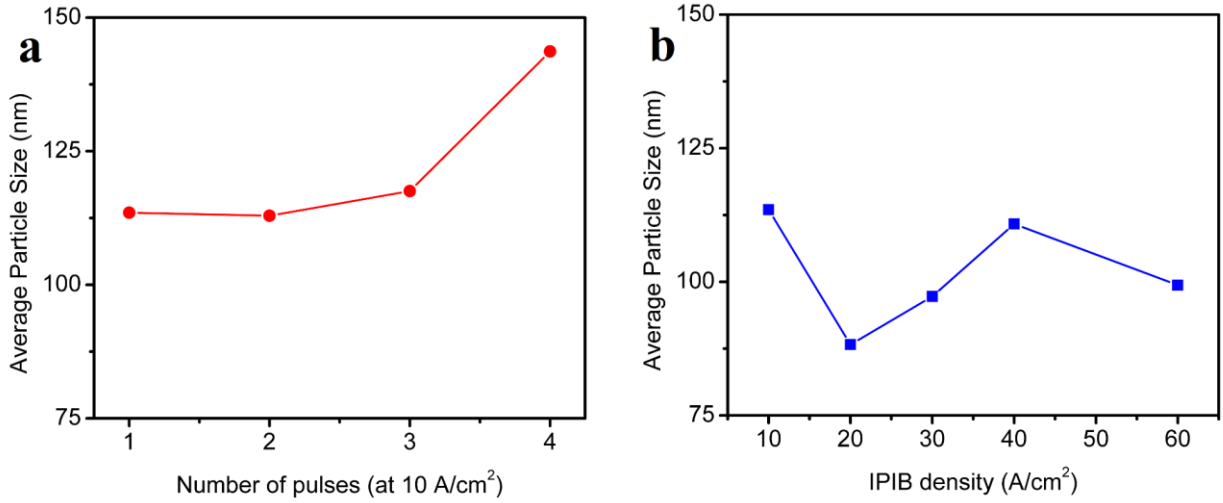

Figure 5.3. Mean diameter of annealed Ag nanoparticles, where a) corresponds to irradiation with different numbers of IPIB pulses, and b) pertains to irradiation with a single IPIB pulse at varying ion beam current densities.

For the comparison of IPIB modification effect on Ag NPs with conventional RTA method, we carried out RTA modification at temperature values extending from 600°C to 1000°C. As was mentioned in prior works, heating temperature, duration of annealing, temperature increasing rate greatly influence the shapes, sizes and concentrations of Ag NPs samples (Araújo et al., 2018). Figure 5.4 represents SEM surface pictures of RTA modified Ag films. We see irregular-shaped and worm-like big islands of Ag NPs at 600°C and 700°C. At temperatures higher than 800°C, Ag coatings turn into fine circular particles. Our experimental outcomes are consistent with the literature data of Ag shape evolution on temperature change: at low temperature heating Ag film turns into worm-like irregular islands, and at higher temperatures depending on substrate and atmospheric condition inside the chamber, Ag film turns into fine circular particles as temperature rises. This last procedure is accompanied by the decreasing number of small particles. Then, further increase of temperature brings coalescence of Ag film into big particles followed by the sublimation, volatilization and removal of Ag films from the substrate (Quan et al., 2017). Size distribution histograms in Figure 5.5 show that a 1000°C heated sample has high concentration of smaller NPs related to 800 and 900°C heated samples. It might be assigned to the start of the volatilization process.

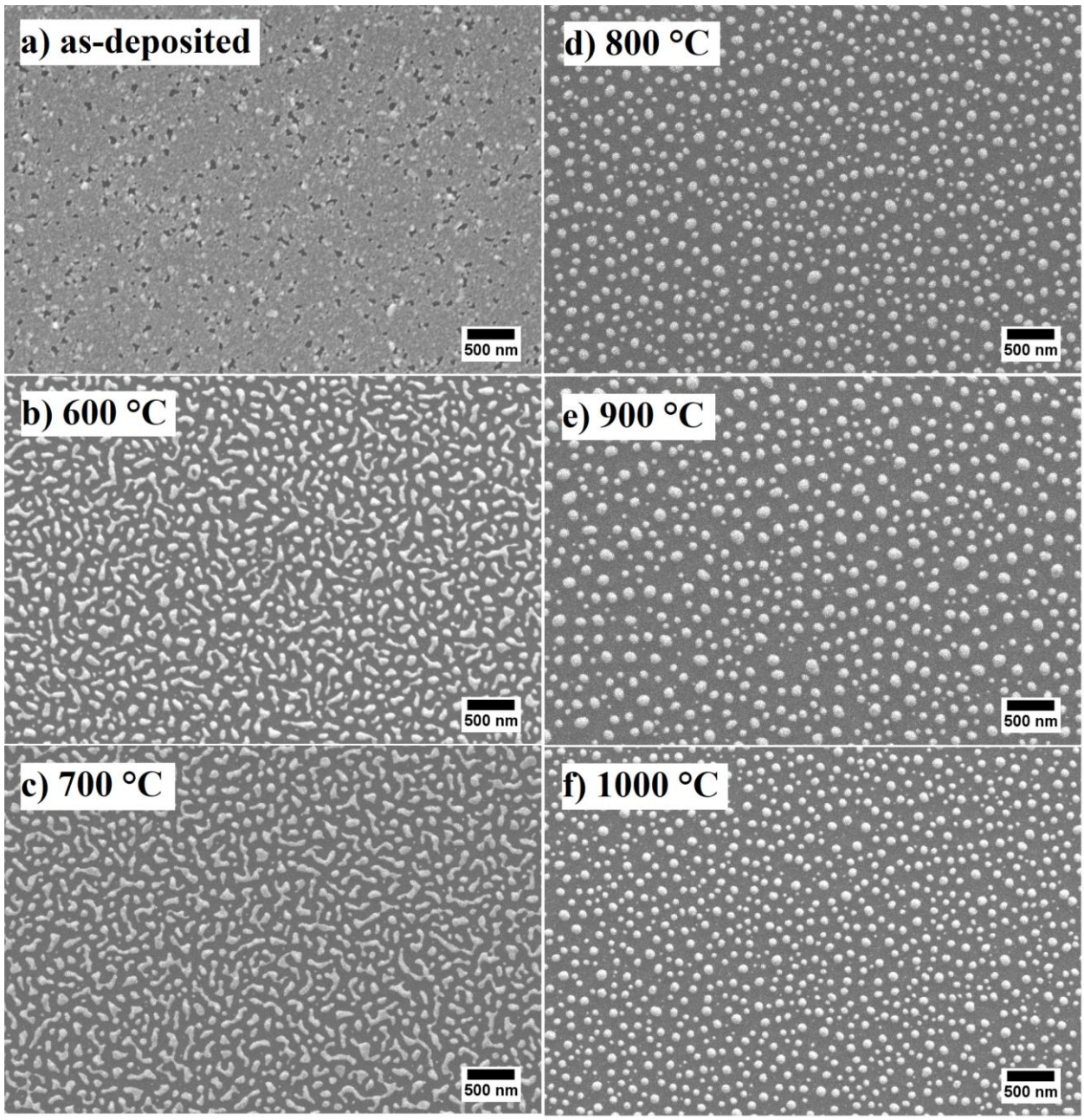

Figure 5.4. SEM images of pre-irradiated Ag coating (a); and RTA annealed Ag coatings at b) 600 °C, c) 700 °C, d) 800 °C, e) 900 °C, f)1000 °C.

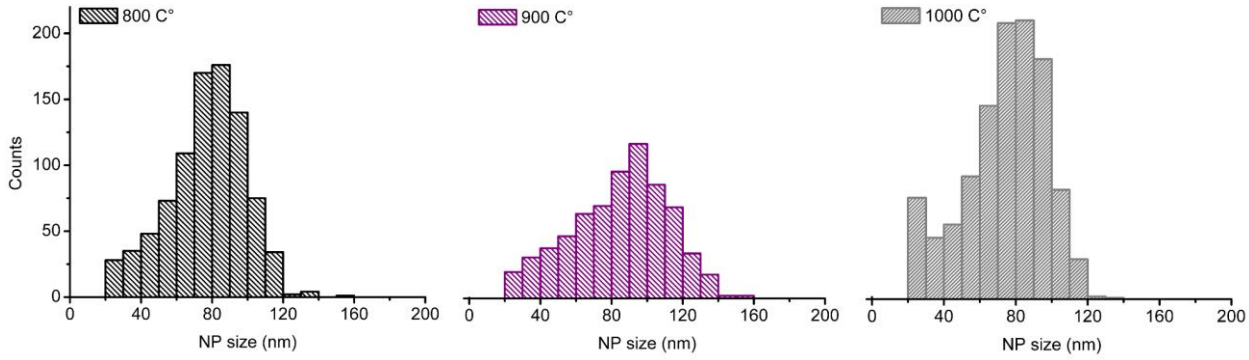

Figure 5.5. Ag NPs' diameter distribution histogram after RTA annealing at 800, 900, and 1000 degrees Celsius.

Ag NPs arrayed in the form of spherical caps are the end product of Ag thin films' solid-state dewetting at high enough heating temperature values. The NPs' sphericity, obtained from the measuring contact angle between NPs and substrate material, is dependent on the NPs' wetting properties (energy of adhesion) to the substrate. Reported results in literature maintain that NPs spherical shape formation is caused mostly by substrate properties and independent of annealing temperature and annealing time (Araújo et al., 2016; Bai et al., 2014; Quan et al., 2017).

Figure 5.6 shows comparison of cross-sectional SEM pictures of Ag coatings after IPIB modification with 40 A/cm^2 current density of ion beams and RTA heating at 1000°C. We distinctly see IPIB modifying created Ag NPs exhibit more spherical form than RTA modified Ag NPs, as shown in Figures 5.6a and 5.6b respectively. The cause of sphericity improvement of Ag NPs created by IPIB irradiation might be the influence of super-fast annealing-heating and annealing-cooling rate. In gradual heating, Ag NPs form semi-spherical shapes by minimization of their surface free energies at dynamic equilibrium conditions. In IPIB irradiation, cooling-down happens in microseconds, so Ag NPs 'freeze' into semi-spherical form in non-equilibrium manner. Consequently, dependences of adhesive forces and wetting characteristics on temperature may influence the latter sphericity properties of Ag NPs. An additional cause of sphericity improvement might be an increase of substrate roughness by IPIB irradiation. This factor was tested by modifying FS substrate with 20 A/cm^2 IPIB irradiation and indeed we saw a rise of substrate roughness. Obviously, the full understanding of causes of sphericity enhancement of Ag NPs after IPIB irradiation is still unknown.

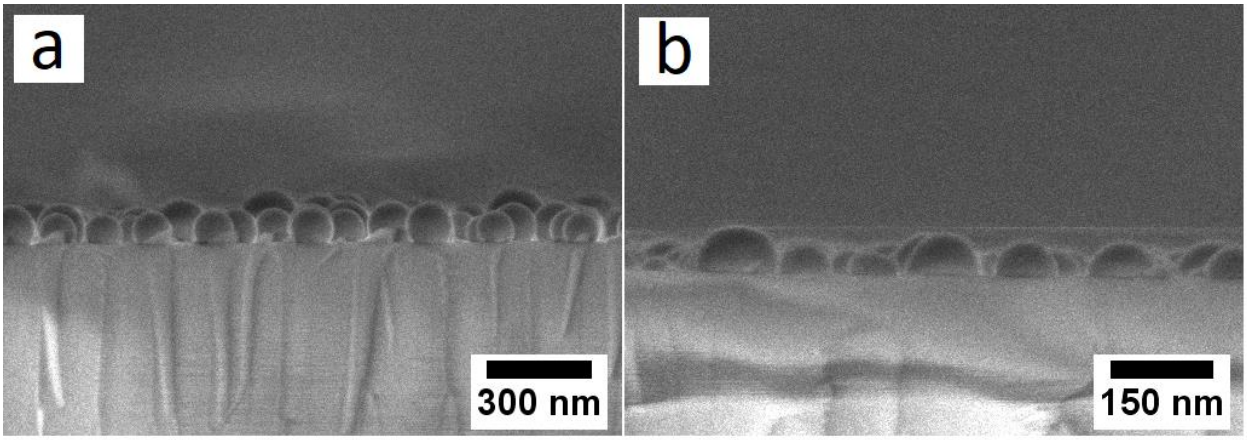

Figure 5.6. SEM cross-sectional images of Ag NPs after being a) 40 A/cm^2 irradiated and b) rapidly thermally annealed at 1000 °C.

Figures 5.7 and 5.8 show GIXRD patterns of Ag coatings that have been RTA modified and IPIB beam treated with differing ion beam current densities and pulse numbers. According to observed GIXRD peaks, the usual face-centered cubic Ag phase may be identified at 38.1°, 44.3°, 64.4°, and 77.4° (card # 01-087-0719 PDF-2). AgO has no identifiable peaks. Conclusion: when compared to as-prepared Ag coatings, both RTA and IPIB annealing induces better crystallinity after modification (Figure 5.7).

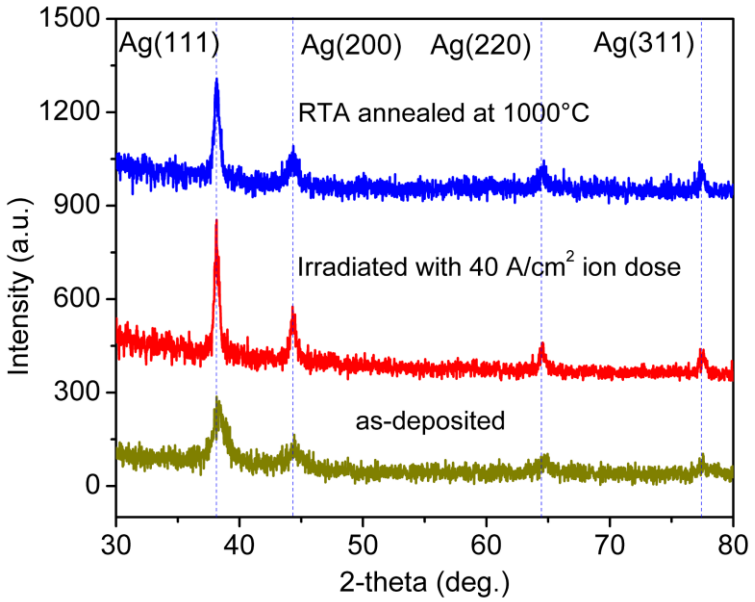

Figure 5.7. GIXRD patterns of as-prepared Ag coatings after they have been annealed with RTA at 1000 °C and exposed to IPIB at a current density of 40 A/cm^2.

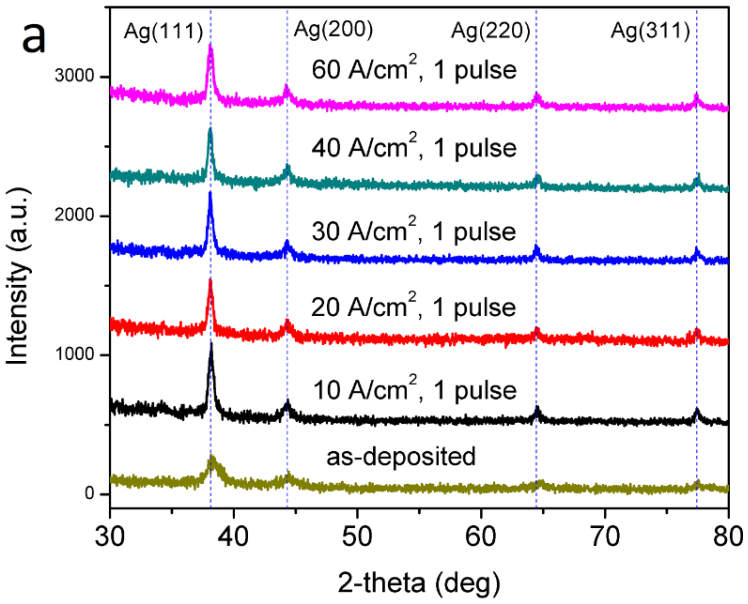
a
Ag(111)
Ag(200)
Ag(220)
Ag(311)
60 A/cm2, 1 pulse
40 A/cm2, 1 pulse
30 A/cm2, 1 pulse
20 A/cm2, 1 pulse
10 A/cm2, 1 pulse
as-deposited
Intensity (a.u.)
2-theta (deg)

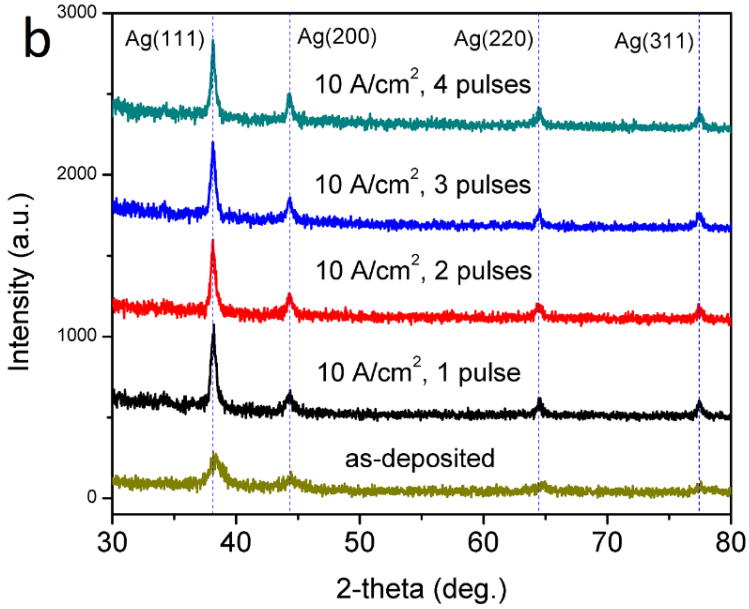
b
Ag(111)
Ag(200)
Ag(220)
Ag(311)
10 A/cm2, 4 pulses
10 A/cm2, 3 pulses
10 A/cm2, 2 pulses
10 A/cm2, 1 pulse
as-deposited
Intensity (a.u.)
2-theta (deg.)

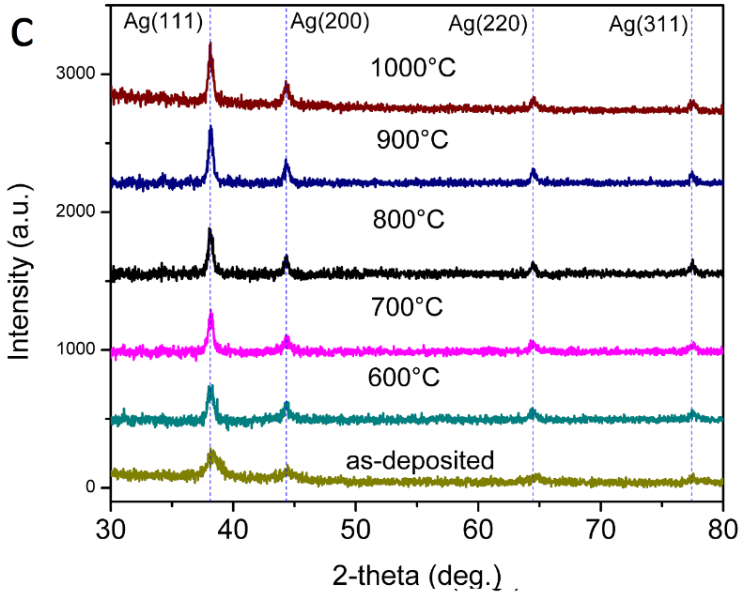
c
Ag(111)
Ag(200)
Ag(220)
Ag(311)
1000°C
900°C
800°C
700°C
600°C
as-deposited
Intensity (a.u.)
2-theta (deg.)

Figure 5.8. GIXRD patterns of as-deposited Ag coatings and following treatments: a) with varying ion beam current densities, b) with increasing pulse numbers at the same 10 A/cm^2 current density of ion beam, and c) RTA annealed at various temperatures.

AFM measurement analysis of Ag NPs modified with IPIB at 40 A/cm^2 are depicted in Figure 5.9: surface AFM image, profile view, and 3D AFM image. Along the inset line in Figure 5.9a, the AFM profile of Figure 5.9b is produced. Ag NP distribution, sizes and height from AFM results are very congruent with SEM findings.

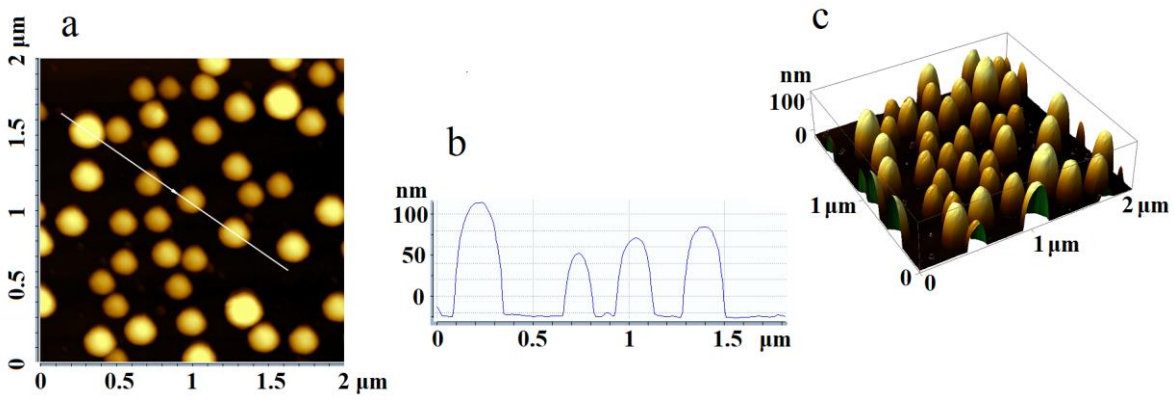

Figure 5.9. AFM surface image (a), AFM profile view (b), and corresponding 3D image of Ag NPs irradiated with ion beams of 40 A/cm^2 current density.

Next, optical characteristics of solid-state dewetted Ag NPs are studied by UV-VIS spectroscopy. All samples show distinct plasmon peaks on their absorption spectra associated with Ag NPs, e.g., dipolar peaks around 450 nm and quadrupolar peaks around 360 nm. IPIB irradiation induced Ag NPs' absorption spectra with varying ion beam current density (Figure 5.10a) in good agreement with average diameter change data in Figure 5.3b. The enhanced absorption and narrow line spectrum are shown for the Ag NPs obtained by IPIB at 60 A/cm^2.

In Figure 5.10b, optical properties of RTA modified Ag NPs are shown. They show clear dipole absorption peaks from 445 to 460 nm for the temperature values of 800-1000°C, whereas for 600 and 700°C they exhibit broad and low intense absorption of worm-like structured Ag NPs (Araújo et al., 2016).

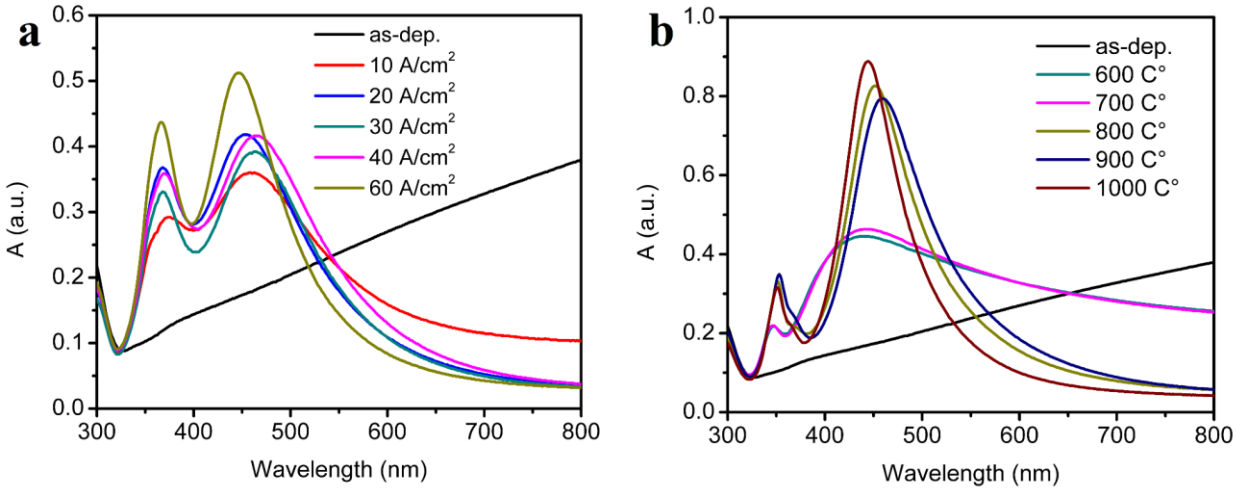

Figure 5.10. Ag NPs absorption spectra following a) IPIB irradiation with variable ion beam current density and b) RTA annealing at various temperatures.

In general, IPIB modified samples show plasmonic peaks of low intensity, with broad linewidth, redshifting and more distinct quadrupolar peaks compared to RTA modified Ag NPs. It is assigned to the creation of particles with bigger sizes after IPIB irradiation than RTA and it is clearly shown in results depicted in Figures 5.2 and 5.5.

5.5 Chapter conclusion

Ag NPs are created from Ag coatings by solid-state dewetting using IPIB modification varying ion beam current densities and number of pulses. Similar Ag coatings are also annealed with the standard RTA method. 100 ns annealing with IPIB irradiation creates Ag NPs with good crystallinity and improved sphericity in comparison with RTA. Previous research demonstrated that the sphericity of the solid-state dewetted NPs at normal and RTA annealing is independent of the annealing factors such as annealing temperature. In contrast, we have demonstrated that the shape and sphericity of Ag NPs are significantly affected by extremely rapid rates of temperature increase and cooling. However, there are still many unanswered questions regarding exact mechanisms Ag NPs create their spherical shape.

6. The photoactivity enhancement of WO_3 photoanodes using combined effect of plasmonic Au NPs and photoluminescent $Y_2O_3:Eu^{3+}$ NPs

6.1 Focus of the chapter

This chapter reports combinational usage of Eu^{3+} doped Y_2O_3 nanoparticles with Au NPs to increase photocatalytic activity of WO_3 photoanodes. Photoactive WO_3 for PEC applications suffers from poor light absorbance in visible range. To use better light absorbance in visible range, plasmonic noble Au NPs have been employed to facilitate photocatalytic activity and increase overall modified photoanode absorbance in the visible range of the electromagnetic spectrum. Further depositing $Y_2O_3:Eu^{3+}$ submicron particles (SPs) on Au NPs/ WO3 photoanode enhances light scattering and enforces utilization of Au NPs plasmonic effect. Such improvement is due to the downconvertion properties of $Y_2O_3:Eu^{3+}$ SPs, e.g., it converts ultraviolet photons into visible photos. As a result, we observed absorbance enhancements, increased electron-hole separation, and improved photocurrent generation from the modified photoanode.

6.2 Introduction

The WO_3 is suitable material for photocatalysis, sensor application and electrochromism (Huang et al., 2015; Lee et al., 2006; Najafi-Ashtiani, 2019). It is widely used for photoelectrochemical (PEC) solar water splitting purposes due to its suitable alignments of conduction and valence band edges with water oxidation/reduction potentials (G. Zheng et al., 2019). However, it suffers from poor solar light utilization in visible range and inefficient charge separation and transport properties (G. Zheng et al., 2019). Up to now, various strategies have been employed to deal with above mentioned drawbacks: surface engineering (J. Li et al., 2021), facet modification (M. Yang et al., 2021), composite creation (Ram et al., 2020), utilization of 2D structures and MXenes (Makola et al., 2023), various doping protocols (Kalanur et al., 2020).

Along with listed strategies, photoluminescence materials can be also combined with photocatalytic WO_{3-x} materials (Dai et al., 2019; Tsai et al., 2016). Previously, fluorescent carbon quantum dots were successfully used for perovskite solar cells (Maxim et al., 2020). The efficiency enhancement of perovskite solar cell was due to the ability of quantum dots to convert UV light into visible light which is beneficial for high absorbance of perovskites in visible range of light. For WO_3 that has poor absorbance in visible range of light, to benefit from photoluminescence downconverting materials, some co-catalyst material is needed. Plasmonic

Au NPs have distinct absorbance peaks depending on size and shape of NPs in visible range of the light. It is also widely used as co-catalyst material for photocatalytic WO_3 photoanodes. Near field and scattering mechanisms of Au NPs/WO_3, while interacting with light, facilitate electron-hole separation and help to increase hydrogen/oxygen evolution rates (Abouelela et al., 2021; Atabaev, 2018).

In this chapter, we report a method of combining Y_2O_3:Eu^{3+} SPs with Au NPs on WO_3 for photocatalytic enhancement. Scattering of light from Y_2O_3:Eu^{3+} SPs and their emission in visible range of light absorbed by Au NPs increase overall photocatalytic activity of WO_3 photoanodes.

6.3 Experimental: photoanode synthesis methods

Overall, 4 samples were prepared referenced as following: reference WO_3 as WO-R, WO_3 with Y_2O_3:Eu^{3+} SPs as WO-Y, WO_3 with Au NPs as WO-A, and WO_3 with Y_2O_3:Eu^{3+} SPs + Au NPs as WO-YA.*WO_3 photoanode preparation and its combination with Au NPs.* Initially, FTO glass substrates underwent a cleaning process in ethanol, employing an ultrasonic bath for a duration of 20 minutes. Subsequently, an oxygen plasma treatment using a Plasma Cleaner set to 'High Mode' was utilized to eliminate any remaining contaminants on the surface. Following this, four identical samples of WO_3 were deposited onto the FTO glass substrates for 33 minutes using the magnetron sputtering technique. The sputtering process was done using a Kurt Lesker DC magnetron system equipped with a W target (W, Kurt J. Lesker, purity of 99.95%, and a diameter of 2.00 inches). The deposition was conducted at a power of 100 W, a base pressure of 11.4 mTorr, and a gas flow rate of 16 sccm for argon and 40 sccm for oxygen. To ensure uniformity in the film, the substrate holder was rotated at a speed of 0.5 rpm during the deposition process. All obtained samples had a film thickness of 55 nm, with an initial amorphous structure. Following synthesis, all four samples were annealed in air at 500°C for 20 minutes, maintaining identical annealing conditions. Next, Au sputter coating with a 3.7 nm thickness was applied to two of the samples using a Q150T ES sputter coater. To convert the top Au film into nanoparticles through solid-state dewetting, all samples underwent hot plate annealing once more in air at 500°C for 20 minutes.

Y_2O_3:Eu^3 SPs synthesis. Europium nitrate hydrate (Eu $(NO_3)_3$*$5H_2O$) with a purity of 99.99%, yttrium nitrate hexahydrate ($Y(NO_3)_3$*$6H_2O$) with a purity of 99.8%, and urea were purchased from Merck and used without any need for purification throughout the experiment. The

preparation of luminescent Y_2O_3:Eu^{3+} SPs followed a previously reported protocol, with slight adjustments, Ref (Askerbay et al., 2020). The combination of yttrium and europium was done in a 97:3 ratio, totaling 1 mmol. In a brief, 0.5 g of urea, 371.5 mg of ($Y(NO_3)_3$*$6H_2O$), and 12.8 mg of (Eu ($NO_3)_3$*$5H_2O$) were accurately blended in 40 ml of deionized water. This obtained mixture was annealed at 90°C in a sealed container for 2 hours. The resulting precipitate of the oxide product was subjected to multiple washes with deionized water, followed by drying and calcination at 600°C for 1 hour in an air environment.

WO-Y and WO-YA preparation. After Y_2O_3:Eu^{3+} SPs synthesis, 2 samples were coated with Y_2O_3:Eu^{3+} SPs using spin-coating method. For that, Y_2O_3:Eu^{3+} SPs were dispersed in DI water in 300 microL volume and poured on sample. The spin rotation was at 1500 rpm with 250 ramps for 30 s. Alternatively, we also used drop-casting deposition of Y_2O_3:Eu^{3+} SPs. Finally, the samples were dried in air at 60 C to enhance adhesion. *Materials characterizations.* Characterization of the materials and samples was conducted as follows: Scanning Electron Microscopy (SEM) images were acquired using the Carl Zeiss Crossbeam 540 GEMINI II Scanning Electron Microscope. Phase structural analysis was carried out using a Rigaku SmartLab Automated multipurpose X-ray diffractometer (XRD) with CuKa irradiation at a wavelength of 0.1541 nm. Optical properties were measured using the Evolution 300 spectrophotometer. The thickness of thin films was checked using the Dektak XT Stylus profilometer.

For specific characterizations of Y_2O_3:Eu^{3+} SPs, SEM (Auriga Crossbeam 540, Carl Zeiss, Oberkochen, Germany), and energy-dispersive X-ray spectroscopy (EDX, Aztec, Oxford Instruments, Abingdon, UK) were used to examine morphological changes and elemental analysis, respectively. The photoluminescence (PL) characteristics of the resulting Y_2O_3:Eu^{3+} SPs were examined using an absolute quantum yield spectrometer (C9920-02, Hamamatsu Photonics K.K., Hamamatsu, Japan).

Linear Sweep Voltammetry (LSV) measurements of the photoanodes were carried out using a CHI660E potentiostat in three-electrode cells with an Ag/AgCl reference electrode (3.5 M KCl). The electrolyte used for LSV measurements was 0.16 M Na_2SO_4 with a pH of 7. A PLS-FX300HU solar simulator (100 mW/cm^2, AM 1.5) served as the light source for all PEC measurements. The obtained potential was then converted to the reversible hydrogen electrode (RHE) scale using the Equation 4.1.

Electrochemical impedance spectroscopy (EIS) was performed in a frequency range from 1 Hz to 10 kHz with an AC voltage amplitude of 50 mV at a DC bias of 0.68 V vs. $V_{Ag/AgCl}$ on light

illumination. Circuit model fitting of EIS data was carried out using the EIS Spectrum Analyzer software (Bondarenko, A.S. et al., 2005).

6.4 Results and discussions

In figure 6.1, SEM pictures of WO-R, WO-Y, WO-A, and WO-YA are shown. Pure WO_3 (WO-R) shows granular surface structure with slanted small hills-like morphology (white bars in Figure 6.1-a) up to 220 nm in size. Au on WO_3 (sample WO-A) shows non-uniformly distributed, irregular-shaped NPs in size range from 8 to 53 nm (in some places up to 100 nm) as shown in Figure 6.1b as white colored particles indicated with yellow arrows. Y_2O_3:Eu^{3+} SPs on WO_3 (sample WO-Y) in Figure 6.1c indicated by blue arrows exhibit distinct uniform sizes of 100 nm in diameter. Lastly, sample WO-YA, all combined, shows successful deposition of all three components in one place (Figure 6.1d). EDS analysis in Appendix A2 confirms successful synthesis of Y_2O_3:Eu^{3+} SPs on WO_3.

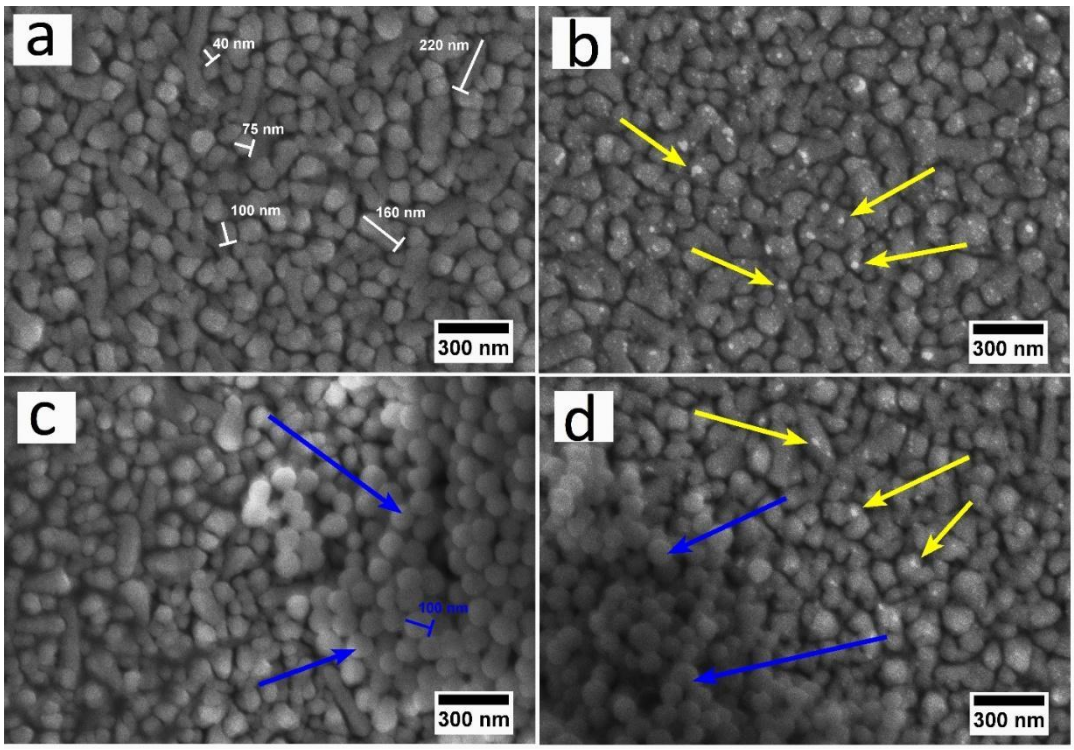

Figure 6.1. Surface SEM images of a) WO-R, b) WO-A, c) WO-Y and d) WO-YA on FTO substrates.

Structural phases of samples were identified by using GI-XRD measurements as shown in Figure 6.2a. The monoclinic crystalline phase (card #: 00-036-0102) of WO_3 is shown in reference WO-

R and in all other samples. No other peaks related to Au or Y_2O_3:Eu^{3+} SPs are detected from GI-XRD patterns. Absence of peaks corresponding to Au or Y_2O_3:Eu^{3+} SPs is assigned to low concentration of materials on WO_3. For that reason, phases of Y_2O_3:Eu^{3+} SPs were identified separately as shown in Figure 6.2b. It shows crystalline cubic phase of Y_2O_3 (card #01-076-8044).

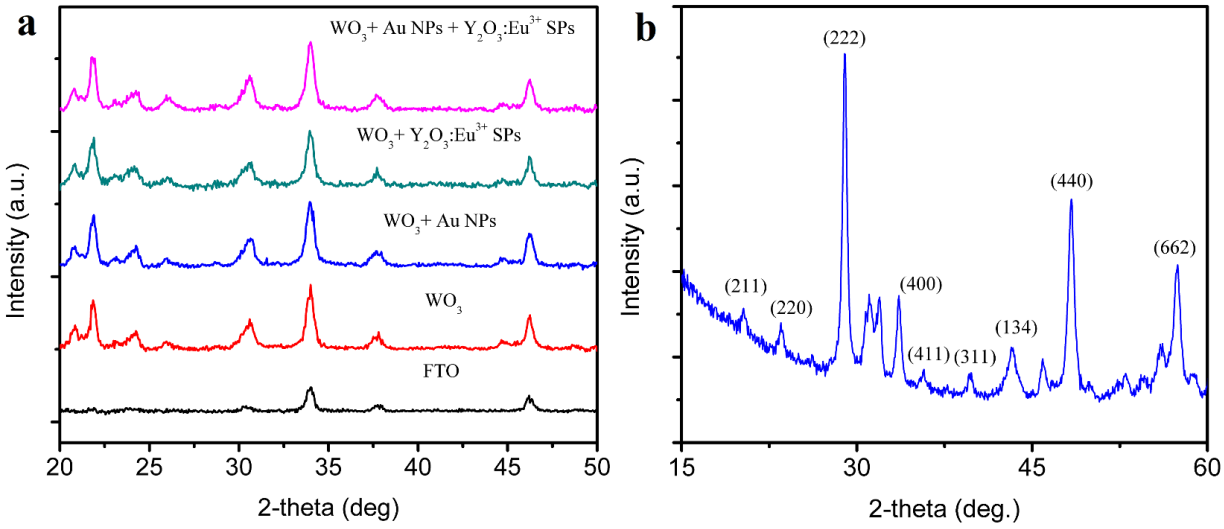

Figure 6.2. XRD patterns of a) WO-R, WO-A, WO-Y, WO-YA, and b) separate Y_2O_3:Eu^{3+} SPs.

The downconvertion properties of Y_2O_3:Eu^{3+} SPs were tested by PL spectroscopy. Figure 6.3 represents the PL excitation and emission results of Y_2O_3:Eu^{3+} SPs with absolute quantum yield of 78.3% at excitation of 250 nm. Four distinctive emissions of Y_2O_3:Eu^{3+} SPs $^5D_0 \rightarrow {}^7F_0$, $^5D_0 \rightarrow {}^7F_1$, $^5D_0 \rightarrow {}^7F_2$, $^5D_0 \rightarrow {}^7F_3$ were identified in spectra (W. Wang & Zhu, 2018). The strength of the $^5D_0 \rightarrow {}^7F_2$ transition located at 610.8 nm is largest. It clarifies emission of the red color and demonstrates the effective integrating of ions into the yttria matrix. The emissions of Y_2O_3:Eu^{3+} SPs in the visible portion of light can possibly increase absorption of Au NPs followed by the energy transfer to the WO_3.

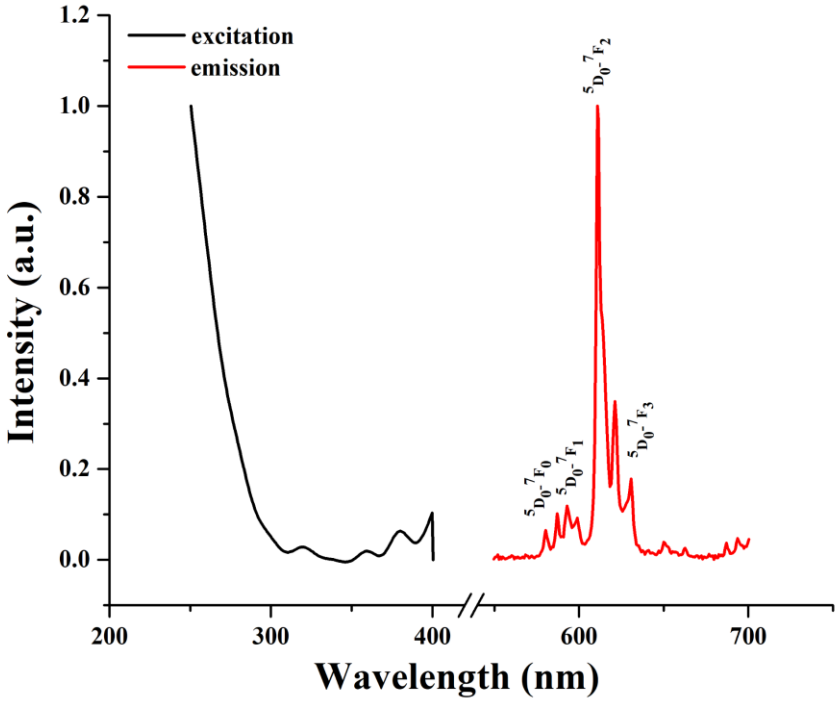

Figure 6.3. PL spectra of Y_2O_3:Eu^{3+} SPs.

The absorbance spectra of samples WO-R, WO-A, WO-Y and WO-YA can be seen in Figure 6.4. Sample WO-R has typical absorbance for UV region of light (< 400 nm) due to its wider band gap. Combining WO-R with Y_2O_3:Eu^{3+} SPs (sample WO-Y) shows absorbance enhancement along the spectra from 350 nm to 800 nm (blue colored line). It is due to slight scattering effect from circular forms of Y_2O_3:Eu^{3+} SPs and their emissions in visible region of the light. Absorbance of the sample WO-A, with Au NPs, shows the characteristic plasmonic resonance peak ~ 540 nm (red colored line). Shape and peak position of plasmonic resonance of Au NPs strongly dictated by their forms and sizes (J. Li et al., 2021). The maximum absorbance is seen on sample WO-YA (Figure 6.4, teal colored line). It can be assigned to the overlay of absorbances from Au NPs, WO_3, and Y_2O_3:Eu^{3+} SPs. One key observation is that the increase in absorbance when using WO-YA is greater compared to WO-Y in a specific spectral range centered at 550 nm. This could confirm effective utilization of photoluminescent material to increase absorption of Au NPs in conjunction with PEC photoanodes.

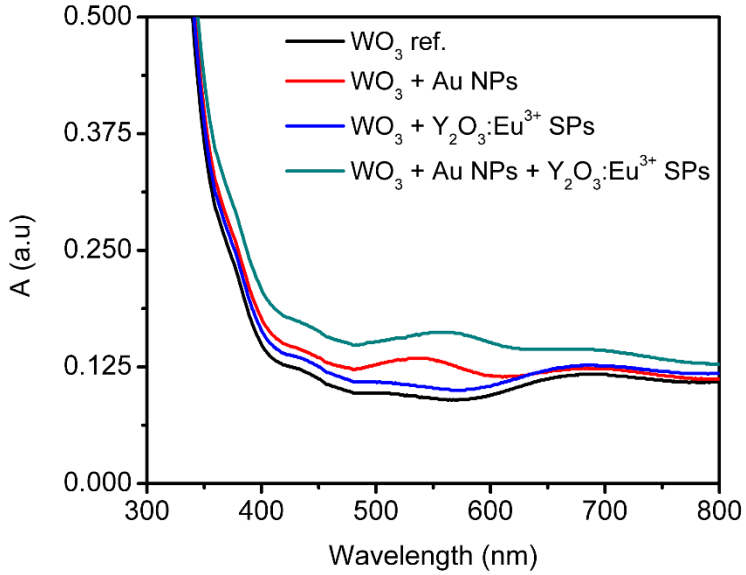

Figure 6.4. Absorbance spectra of WO-R, WO-Y, WO-A, and WO-YA samples.

Robust light scattering from $Y_2O_3:Eu^{3+}$ SPs can boost both Au NPs' and WO_3 capability to benefit from extra light photons. Additionally, the light emitting from $Y_2O_3:Eu^{3+}$ SPs (seen from 550 and 600 nm) can be absorbed by Au NPs with resonance peaks located at the red region of the light. Resultantly assisted by Au Nps with near field mechanism and improved charge-carrier creation would improve efficiency in WO_3 photoanode. Figure 6.5 provides a visual depiction of the integrated photoanode, illustrating the concept. It illustrates how light harvesting occurs with combined assistance of Au NPs and $Y_2O_3:Eu^{3+}$ SPs.

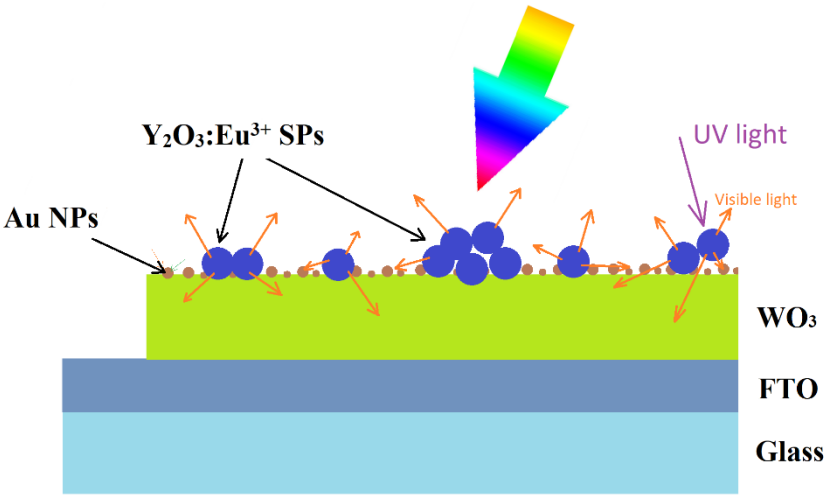

Figure 6.5. Schematics for WO_3 photoanode covered by Au NPs and $Y_2O_3:Eu^{3+}$ SPs for improved efficiency.

The photocatalytic activity of prepared photoanodes is tested with LSV measurements as shown in Figure 6.6a. Total photocatalytic current generation raised by 37.5 % on sample WO-YA

compared to WO-R at 1.23 V vs RHE. Samples WO-Y and WO-A also show slight increase in photocurrent generation. Still, usage of both Au NPs and Y_2O_3:Eu^{3+} SPs provides significant effect for photoactivity of WO_3. We ascribe such enhancement to light managing caused by the above-mentioned combination. EIS measurement results in Figure 6.6-b clearly indicate (inset) that sample WO-YA, WO_3 combined with Au and Y_2O_3:Eu^{3+}, has improved charge-transport characteristics compared to other samples.

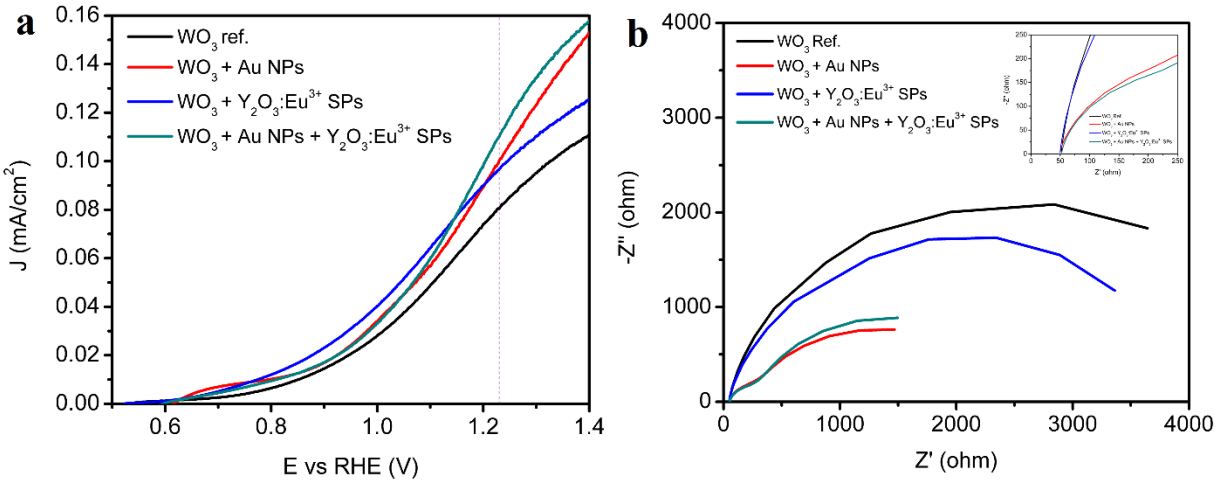

Figure 6.6. a) LSV and b) EIS measurements of WO-R, WO-Y, WO-A, and WO-YA samples.

To check the repeatability of the results, extra experiments were done while changing parameters such as Au film thickness and concentrations of Y_2O_3:Eu^{3+} SPs. Concentrations of Y_2O_3:$Eu3^{+}$ SPs on WO_3 can be managed by adjusting spin-coating rotating speed. To be certain, Y_2O_3:Eu^{3+} SPs were deposited on the same photoanodes where Au NPs coated after LSV measurement, and LSV measurements are done again in the similar settings. Experiment outcomes are shown in Figure 6.7, where for (a) Au thin film thickness was 1.9 nm and speed of Y_2O_3:Eu^{3+} SPs' spin-coating was 2000 rpm, for (b) Au – 2.9 nm and Y_2O_3:Eu^{3+} SPs spin-coating speed was 1000 rpm, for (c) Au – 5.1 nm and Y_2O_3:Eu^{3+} SPs deposited by drop-casting method. All cases show photocatalytic enhancement after using both Au and Y_2O_3:Eu^{3+} SPs, where the highest photocurrent enhancement was 73 % at 1.23 RHE for drop-casting employed sample (Figure 6.7-c) due to larger concentrations of Y_2O_3:Eu^{3+} SPs.

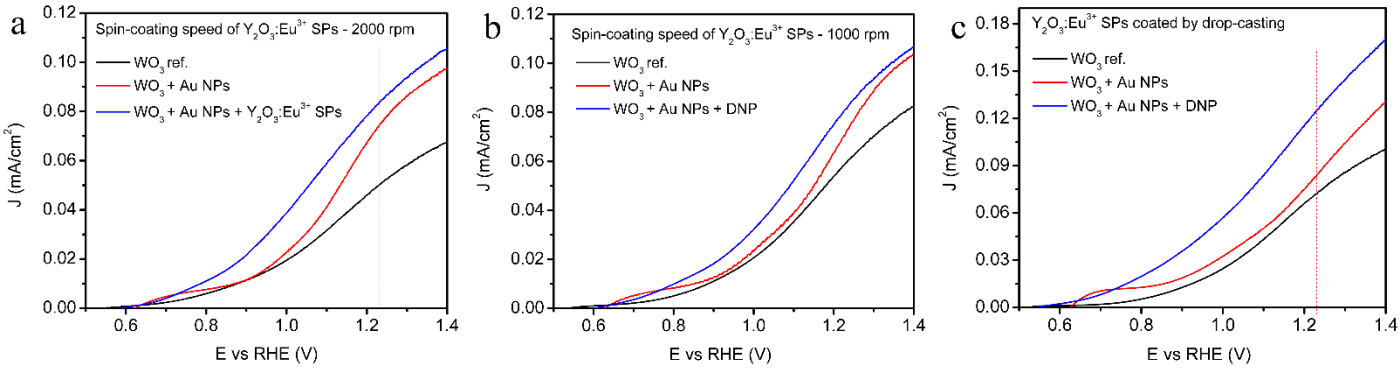

Figure 6.7. a) Conducting LSV measurements on WO_3 photoanodes incorporating Au NPs and $Y_2O_3:Eu^{3+}$ SPs with the following parameters: a) spin-coating Y2O3:Eu3+ SPs onto a initially 2 nm thick layer of Au at 2000 rpm, b) spin-coating $Y_2O_3:Eu^{3+}$ SPs onto a initially 3 nm thick layer of Au at 1000 rpm and c) depositing $Y_2O_3:Eu^{3+}$ SPs onto a initially 5 nm thick layer of Au using the drop-casting method.

To confirm downconversion effect or scattering effect for photocatalytic enhancement on sample WO-YA, additional experiments are performed. To check, Y_2O_3 NPs were fabricated with no Eu doping and coated onto WO_3 with drop casting and spin-coating method at 1500 rpm. We observed that Y_2O_3 NPs/WO_3 photoanode has no enhanced photocatalytic activity as seen in Figure 6.8a, whereas drop casted Y_2O_3 NPs on WO_3 sample shows slight increase of photocurrent compared to sample results (drop casted $Y_2O_3:Eu^{3+}$ SP) in Figure 6.7c. It is obviously seen that the main role was played by downconversion of $Y_2O_3:Eu^{3+}$ SP in photocatalytic improvement of sample WO-YA. SEM pictures in Figure 6.9 show successful coating of Y_2O_3 NPs on WO_3.

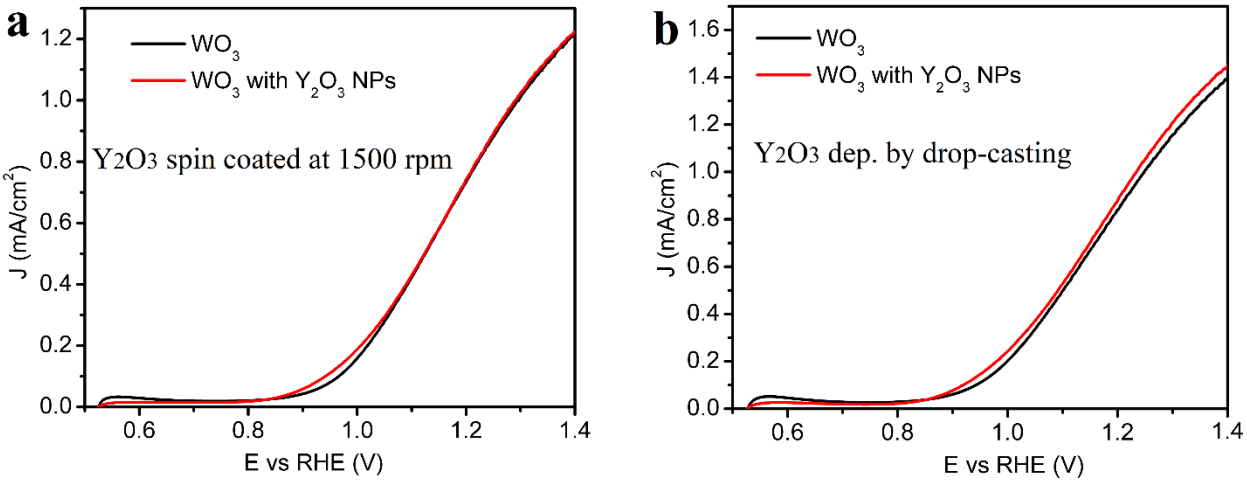

Figure 6.8. LSV testing of WO_3 photoanodes with Y_2O_3 NPs was carried out through two different approaches: a) via the spin-coating method and b) drop-casting method.

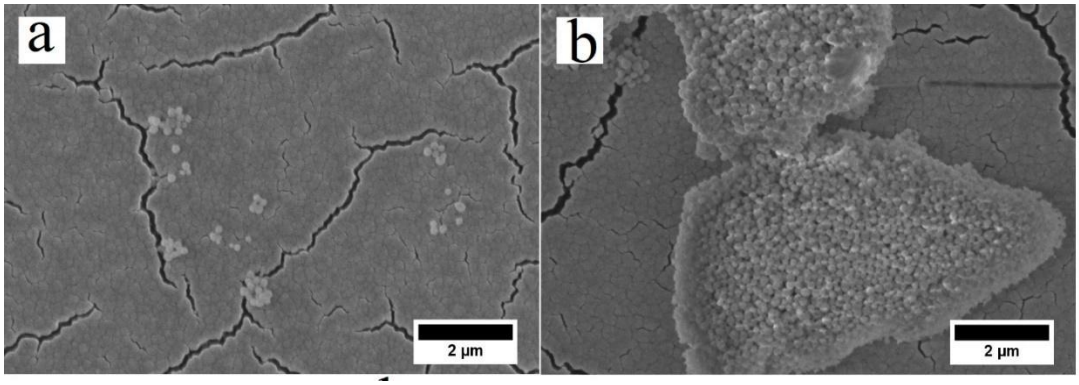

Figure 6.9. Surface SEM images of WO_3 photoanodes with Y_2O_3 NPs were carried out through two different approaches: a) via the spin-coating method and b) drop-casting method.

6.5 Chapter conclusion

This chapter reports novel way to employ photoluminescent downshifting material combined with Au nanoparticles for improved photocatalysis efficiency. We prepared using magnetron sputtering identical WO_3 photoanodes and added both Au NPs and photoluminescent Y_2O_3:Eu^{3+} SP. Our findings show that integration of Au NPs and Y_2O_3:Eu^{3+} SP with WO_3 significantly increase photocurrent generation due to combined effects of plasmonic, downconversion and scattering. We believe that our study opens new opportunities for the utilization of photoluminescent materials in various applications, including photocatalysis and water splitting.

7. Modification of WO_3 thin films without substrate by IPIB irradiation

7.1 Focus of the chapter

The WO_3 is a cheap, relatively stable, and easy synthesized metal oxide material that has high potential usage in many fields: water oxidation and purification, electrochromic, sensors, etc. Required optoelectronic properties of WO_3 for those applications can be achieved by using IPIB irradiation. For that purpose, it is important to study IPIB irradiation effect on WO_3 thin films. In previous chapters, IPIB irradiation of WO_3 thin films were conducted on FTO substrates where we observed WO_3 sponge-like structures after irradiation. There is fast heat transfer (fast cooling) to the substrate during and after the irradiation in WO_3/substrate configuration. Energy delivered by IPIB to the WO_3 layer increases its temperature typically to several hundred degrees of Celsius and, in the absence of substrate, WO_3 layer cools down slowly. Since heat diffusion into

the substrate (in particular, into commercial crystalline FTO used in previous chapters) is significantly fast than environmental heat dissipation.

In this chapter, modification of WO_3 thin films by intense pulsed proton beam irradiation was carried out on TEM membranes to see modification results while IPIB annealing cools down slowly. The used TEM membranes have open window with SiN (of 15 nm) support film on it which is enough to minimize substrate effect. Results show creation of non-sponge structures at 10 A/cm^2 compared to WO_3 with FTO substrates. Additionally, creation of single crystalline plates and distinct dislocations in crystalline WO_3 samples are observed at 4 and 10 A/cm^2 ion beam current densities of IPIB irradiation.

7.2 Introduction

The $WO_{3\leq x}$ thin films have great applications in many fields due to their photocatalytic activities, electrochromic properties and stability. Improvement of their optoelectronic properties and functionalities often result from modifications that create beneficial defects such as oxygen vacancies, lattice distortions, dislocations, etc.

Ion irradiation is a powerful technique to create and control defects in thin film nanomaterials by altering, particularly, optical, electrical, and structural properties (X. Wang et al., 2020). Point defects such as oxygen vacancies, lattice dislocations, interstitial ion doping can increase performance of photocatalyst materials such as WO_3 (Kozlovskiy et al., 2021; Kozlovskiy & Zdorovets, 2020). It was shown that proper concentration of oxygen vacancies can give positive influence to improve photocurrent generation, to charge carrier generation, separation and transport properties of photoelectrodes (Y. Li et al., 2016; Y. Zhang et al., 2019). In our case, the IPIB irradiation of the material leads to surface annealing and strongly depends on the underneath substrate's thermal diffusion properties. During the IPIB irradiation, proton ions penetrate the material to few microns including substrate, and give temperature rise to anneal the near-surface layer as seen in Figure 7-1. After the initial heat-up during the IPIB irradiation, the hot surface layer cools down by conducting heat deeper into substrate and radiating heat outside. In this sense, the cooling time dominantly controlled by substrate material (FTO in our case) and it has a huge impact on crystallization processes of irradiated WO_3. In previous chapters we used FTO glass substrates, therefore cooling happens fast due to intense heat diffusion into the substrate. In the absence of a substrate, the energy supplied by IPIB raises the temperature of the WO_3 layer to several hundred degrees Celsius, which then cools down slowly.

In this chapter, we studied the influence of IPIB irradiation on free-standing WO_3 thin film without the substrate. Amorphous (a- WO_3) and crystalline(c-WO_3) WO_3 thin films were prepared on TEM membranes by magnetron sputtering method. c-WO_3 thin films were prepared from a-WO_3 thin films by subsequent hot plate annealing in air.

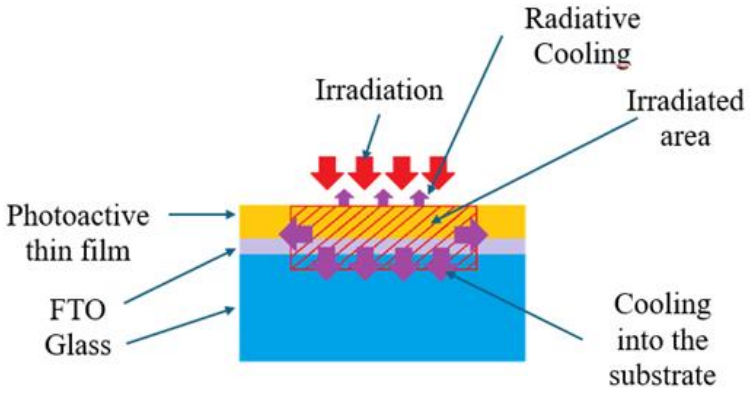

Figure 7.1. The schematic diagram of IPIB irradiation effect on WO_3/FTO/Glass photoanode.

7.3 Experimental methods

WO_3 thin films were deposited by Kurt Lesker magnetron system by reactive sputtering W (purity 99.99 %) target with identical thicknesses (~ 30 nm) on commercial TEM membranes (Ted Pella, Si wafer with window that has 15 nm SiN). Deposition parameters are as following: power – 100 W, dep. time – 1min 30 s, oxygen, and argon flow rates – 21/33 sccm, chamber pressure during the deposition – 11.4 mTorr.

After deposition, half of the samples were annealed to crystallize the structure at 500°C on a hotplate in air for 1 hour. Samples denoted from WO - 1 to WO - 8 and their IPIB irradiation parameters are given in Table 7.1

Table 7.1. Parameters and modification information of WO_3 thin films on TEM membranes.

Phase	Amorphous				Crystalline			
Sample name	WO-1 (amorphous-reference)	WO-2	WO-3	WO-4	WO-5 (crystalline-reference)	WO-6	WO-7	WO-8

Ion beams current density (A/cm^2)	0	4	10	17	0	4	10	17

7.4 Results and discussions

Overall, 8 WO_3 thin film samples were prepared (4 c-WO_3, 4 a-WO_3) and 6 of them were irradiated with IPIB at 4, 10, 17 A/cm^2 ion beams current densities. We observed that samples both amorphous and crystalline irradiated at 17 A/cm^2 have been broken and flown away as a result of surface pressure induced by such high ion beam current density. Consequently, only results from samples WO-1, WO-2, WO-3, WO-5, WO-6, WO-7 are considered for further analysis.

As-deposited thin films show amorphous nature (sample WO-1), but after annealing at 500°C in air, they are converted into polycrystalline WO_3 (sample WO-5) as shown on TEM images in Figures 7.2a and 7.2b.

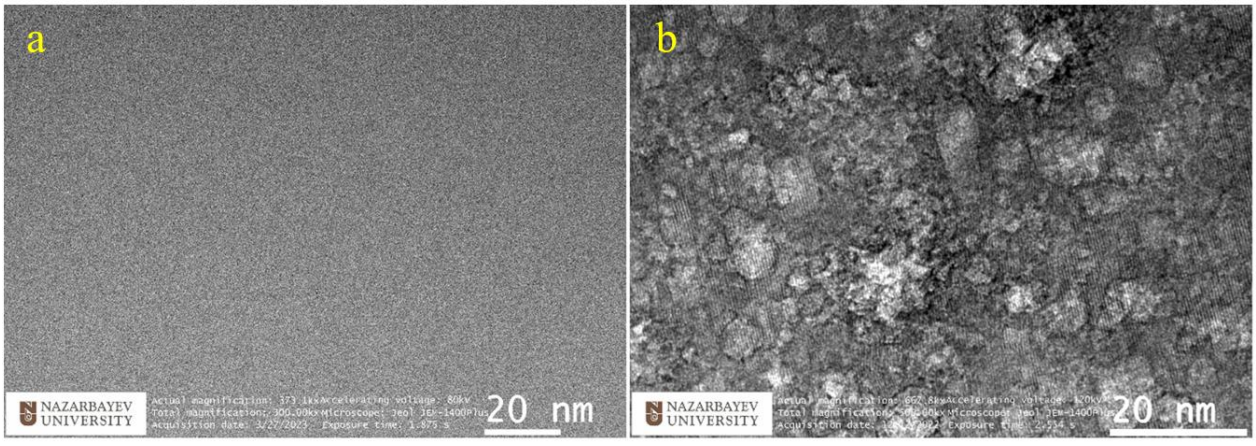

Figure 7.2. TEM images of WO_3 thin films: a) as-deposited (amorphous) a-WO_3 and b) after annealing at 500°C, c-WO_3.

Polycrystalline TEM imaging of annealed sample (c-WO_3) shows grains of various sizes up to 30 nm. No distinct defects or dislocations are observed in this step.

Figure 7.3 shows TEM images of a-WO_3 and c-WO_3 samples after irradiation at 4 A/cm^2 ion beams current density. Sample WO-2 in Figure 7.3-a at 60kx magnification with diffraction pattern inset and magnified at 500kx in 7.3-b show that a-WO_3 turned into polycrystalline thin films with distinct grains after irradiation. Surface and bulk structure of the became uniformly distributed irregular mountain structured morphology with no cracks. No dislocations or other defects are seen in thin film after irradiation as seen from Figure 7.3-a,b. After irradiation c-WO_3 at 4 A/cm^2, WO-6 has separate distinct regions (plates) with cracks at boundaries (indicated with green arrows) that appeared due to thermal expansion during the annealing process as seen in Figure 7.3-c, 7.3-d, and 7.3-e. WO-6 sample exhibits homogeneous morphology with long hills (dark regions in Figure 7.3-c) that stop at boundary cracks. We conclude that irradiation at 4 A/cm^2 turned polycrystalline c-WO_3 into plates of single crystalline order. This fact can be observed from WO-6 TEM image in Figure 7.3-d (1000 kx magnification) that shows atomic lattice patterns of three separate plates grown in three different directions and separated by cracks. To confirm, we checked diffractions from the sample region that contain five different plates (Figure 7.3-e) and the region with only one plate (Figure 7.3-f).

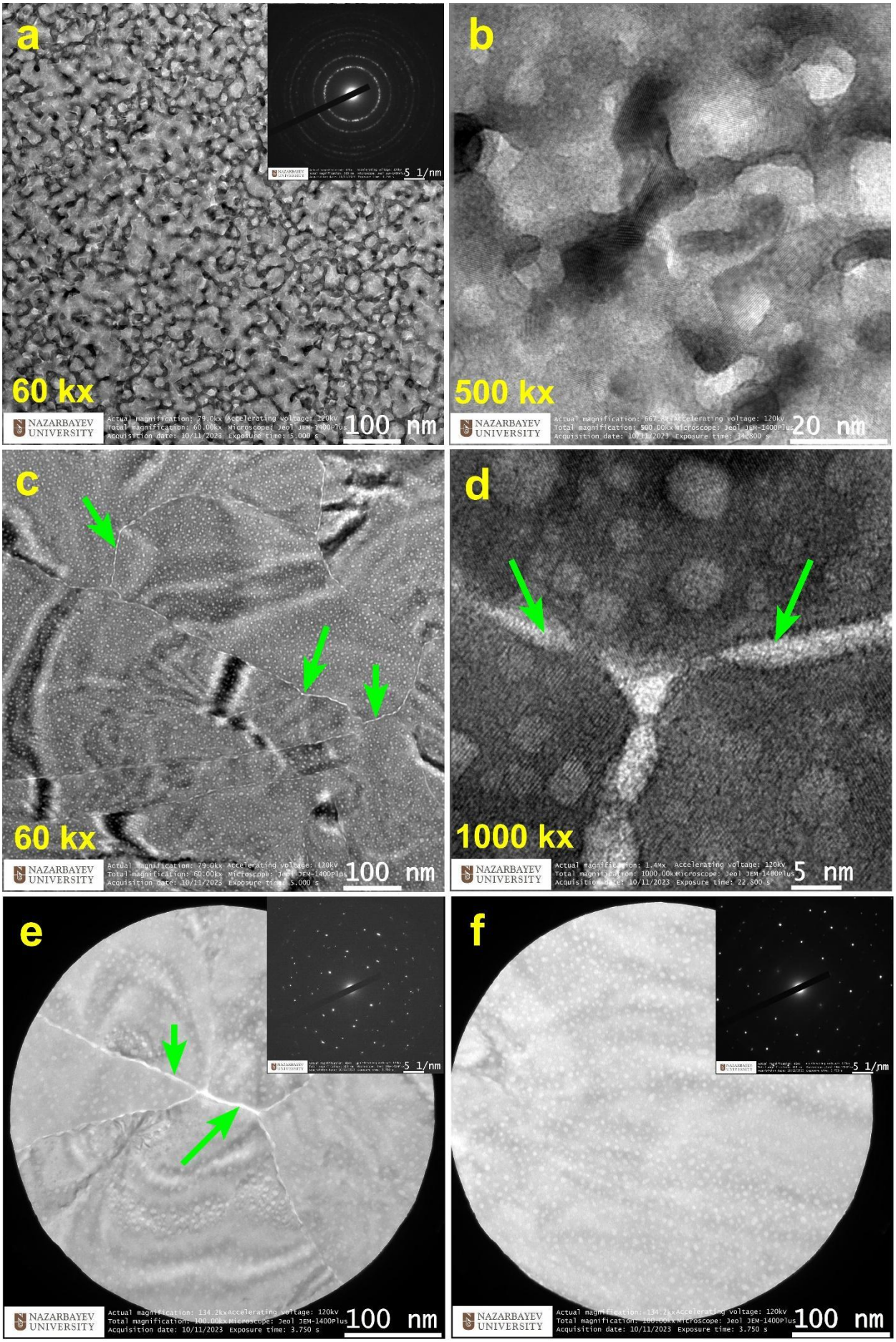
a
60 kx
5 1/nm
NAZARBAYEV UNIVERSITY
100 nm
b
500 kx
NAZARBAYEV UNIVERSITY
20 nm
c
60 kx
NAZARBAYEV UNIVERSITY
100 nm
d
1000 kx
NAZARBAYEV UNIVERSITY
5 nm
e
5 1/nm
NAZARBAYEV UNIVERSITY
100 nm
f
5 1/nm
NAZARBAYEV UNIVERSITY
100 nm

Figure 7.3. TEM images of a) sample WO-2 at 60 kx magnification, b) sample WO-2 at 500 kx magnification and c) sample WO-6 at 60 kx magnification, d) sample WO-6 at 1000 kx magnification. Images e and f shows sample WO-6 with and without crack and their corresponding diffraction patterns in insets.

Corresponding diffraction patterns of chosen regions reveal that indeed each single crack plate has single crystalline nature. It might be explained by the combined effect of annealing and directional influence from the ion beam irradiation. Initially crystalline samples recrystallizes and under ion flow directional influence creates single crystalline structures, aligned with the ion flow. We believe that 4 A/cm^2 is suitable ion beam current density to have directional influence for this thickness of the WO_3 thin film with plates. Overall, morphological changes show that initially crystalline sample has more morphological resistance to IPIB ion beam irradiation at 4 A/cm^2 than initially amorphous sample, since more energy needed to change atomic positions of stable crystalline structures.

Figure 7.4 shows TEM images of samples WO-3 and WO-7 that were irradiated at 10 A/cm^2 ion beams current densities. The WO-3 shows non-homogeneous thin film with separate plates and accumulated nanoparticles (indicated with green arrows, up to 100 nm in size) as seen from TEM images in Figure 7.4-a, 7.4-c and 7.4-e. Corresponding diffraction pattern inset in Figure 7.4-a and atomic order pictures in high resolution TEM image in Figure 7.4-e confirm its polycrystalline nature after irradiation. Usually, separate plates separated by cracks at boundaries occurs during the annealing processes in thin films. Cracks separating plates appear after irradiation induced high temperature rise followed by with mechanical strains and cracking during the cool down. This short pulsed high temperature rise causes material to melt and then recrystallize again. Most of the sample WO-3 flew away compared to initially crystalline WO-7 sample due to sputtering induced by IPIB irradiation. The TEM image of initially crystalline sample (WO-7) in Figure 7.4-b shows homogeneous thin films with distinct separate polycrystalline plates with cracks at boundaries. Diffraction pattern inset in Figure 7.4-b and high-resolution TEM images in Figure 7.4-d show that sample WO-7 also has polycrystalline nature. It was revealed that IPIB irradiation of c-WO_3 thin films with 10 A/cm^2 induces many dislocations, shown at high-resolution TEM image in Figure 7.4-f. Such dislocations were not observed from initially amorphous WO-3 sample or from samples irradiated at 4 A/cm^2. More dislocation images from the same sample (WO-7) can be found in Appendix A3.

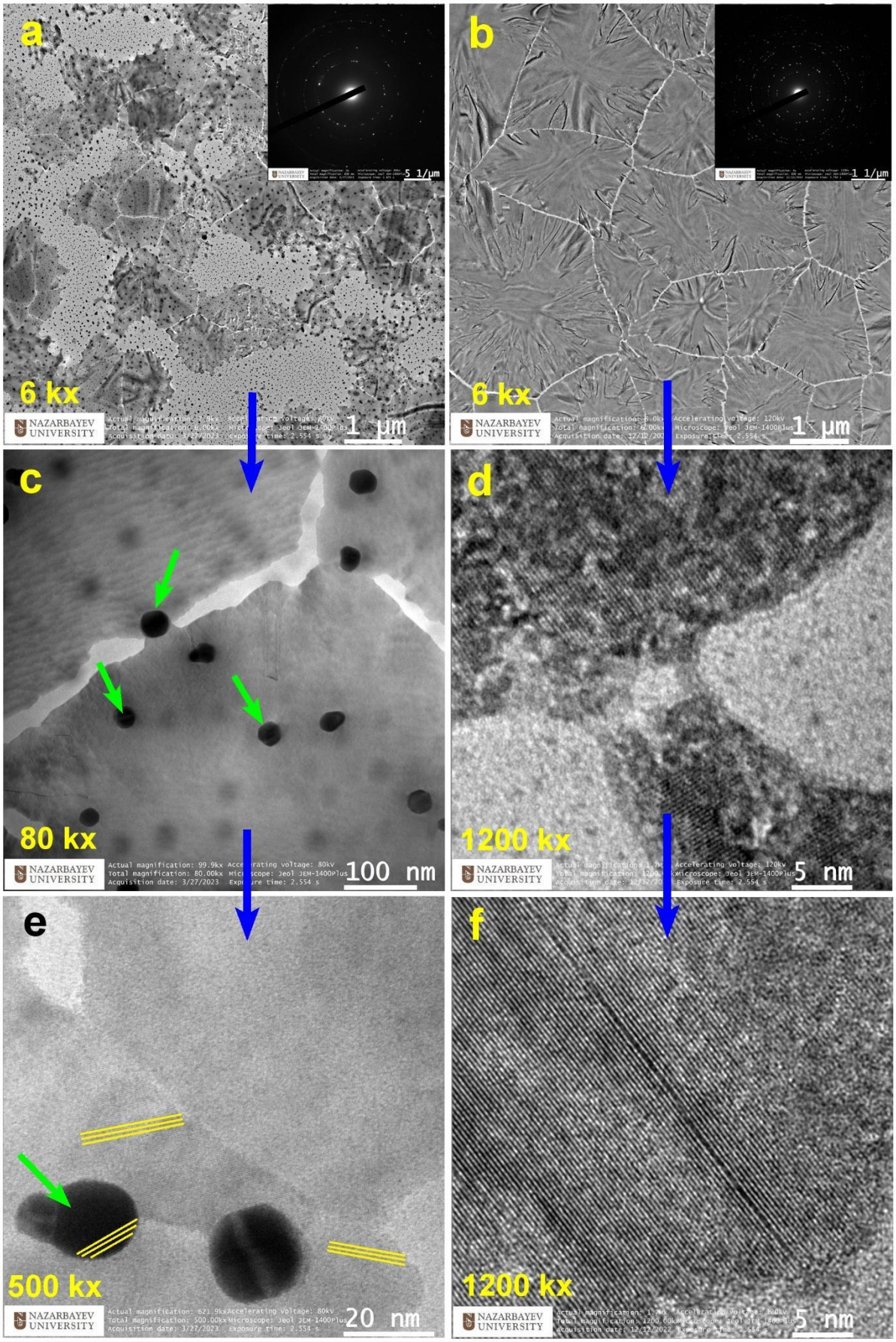
a
6 kx
1 μm
b
6 kx
1 μm
c
80 kx
100 nm
d
1200 kx
5 nm
e
500 kx
20 nm
f
1200 kx
5 nm

Figure 7.4. TEM images: a) sample WO-3 and b) sample WO-7 both at 6 kx magnifications with their corresponding diffraction pattern insets at right top; images c) and e) show sample WO-3 at 80 kx, 500 kx magnification respectably; images d) and f) exhibit sample WO-7 at 1200 kx magnification. Image f shows distinct dislocation induced by ion beam irradiation at 10 A/cm^2.

Figure 7.5 shows initially amorphous and crystalline WO_3 thin films with substrates on FTO/glass and without substrates on TEM membranes irradiated at 10 A/cm^2 ion beam current density. As was explained previously, irradiation of WO_3 thin films on FTO/glass substrates happens with consequent fast cooling due to intense heat diffusion to the substrate layer, otherwise, without substrate subsequent cooling is slow. This explains creation of sponge-like structures on initially amorphous WO_3 with substrates compared to initially amorphous WO_3 without substrates as seen in Figures 7.5-b and 7.5-d. As melting and crystallization happens during the irradiation, with substrate, sample freeze on that sponge like morphology due to fast cooling in non-equilibrium way.

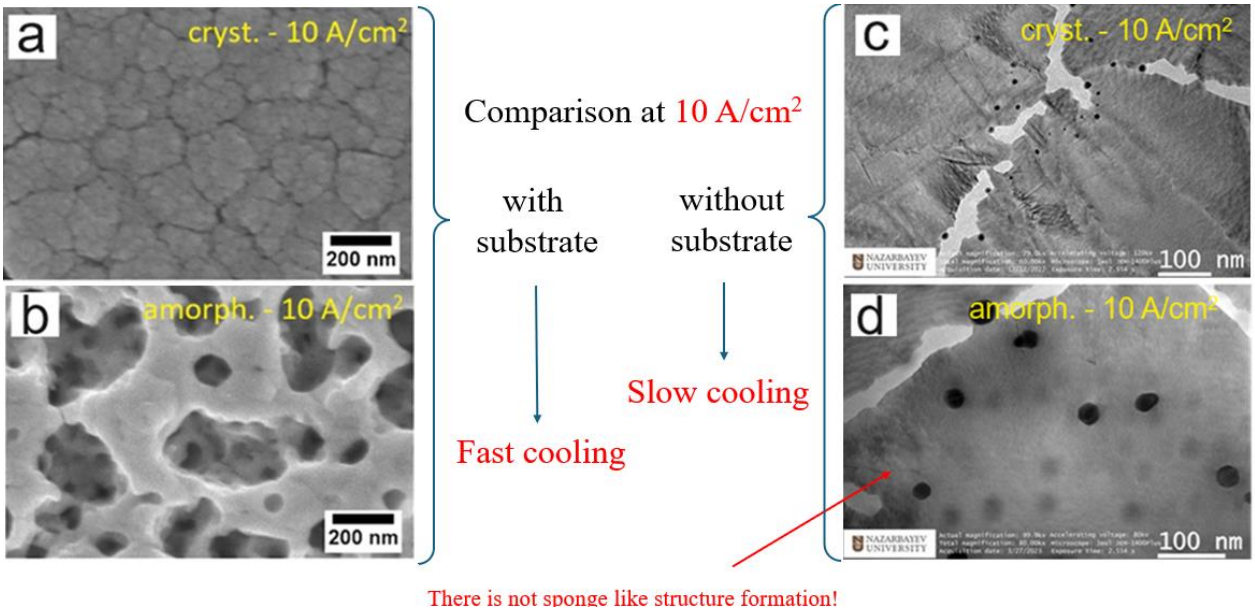

Figure 7.5. Initially amorphous and crystalline WO_3 thin films a), b) with substrates on FTO/glass and c), d) without substrates on TEM membranes irradiated at 10 A/cm^2 ion beam current density (sample WO-7).

In conclusion, we show that ion beams current density of 10 A/cm^2 might be optimum value for irradiating WO_3 thin films to induce maximum number of dislocations and point defects which are beneficial at some extend for usage in PEC applications. Also, we report the optimum IPIB

irradiation current density 4 A/cm^2 ion, at which initially polycrystalline WO_3, free standing (no substrate), turn into the collection of large size (up to few microns in lateral size) single crystalline plates.

7.5 Conclusions

WO_3 thin films of ~30 nm thicknesses were synthesized onto TEM membranes and irradiated with IPIB to study structural and morphological changes. Our initially deposited samples have an amorphous nature and they become polycrystalline after hot plate annealing in air. IPIB irradiation of the amorphous sample at 4 A/cm^2 changes its morphology into uniformly distributed polycrystalline film. IPIB irradiation at current density of 4 A/cm^2 of polycrystalline WO_3 sample turns into homogeneous film with long hills, structure changes into single crystalline plates. No defects or dislocations are observed for both the amorphous and crystalline samples after 4 A/cm^2 irradiation. However, irradiation at 10 A/cm^2 induces substantial morphological changes on both crystalline and amorphous samples. Amorphous sample obtains polycrystalline nature with non-homogeneous thin film structure with separate plates. Polycrystalline film irradiated at 10 A/cm^2 turned to homogeneous polycrystalline film with distinct plates separated with cracks and many dislocations. It can be concluded that 10 A/cm^2 is the optimum ion beam current density for inducing large number of dislocations and defects that can have a beneficial role in PEC usage.

8. Conclusions and Outlook

8.1 Summary and conclusions

In conclusion, this thesis has been dedicated to advancing the surface modification of magnetron sputtered WO_3 photoelectrodes through a comprehensive exploration of of effect of intense pulsed ion (proton) beam (IPIB) irradiation. The primary objective was to enhance the photocatalytic properties of WO_3, with a specific focus on studying the impact of IPIB irradiation on WO_3, on the shape formation of plasmonic Ag NPs and studying combined plasmonic NPs and fluorescent NPs with WO_3.

IPIB method, which uses energetic ions that penetrate up to few micrometers of the material and modify its surface with superfast annealing, served as a robust tool in this investigation. Additionally, the application of IPIB opens new opportunities of silver NP sphericity control at solid-state dewetting, revealing a significant influence of super-fast annealing on the sphericity of these nanoparticles.

Magnetron technology, renowned for its efficiency in thin film deposition and coating processes, contributed additional dimensions to the surface modification strategies employed in this work. The synergy between IPIB and magnetron techniques not only enhanced the efficacy of surface engineering but also opened paths for innovative approaches in tailoring material surfaces for improved photocatalysis.

Furthermore, the concurrent utilization of plasmonic NPs and fluorescent materials, strengthened by the advantages of both IPIB and magnetron technologies, emerged as a highly effective strategy for increasing the photoactivity of WO_3 thin films. Consequently, this research not only propels the frontier of surface modification techniques but also illuminates the intricate interplay between WO_3 and IPIB while substrate effect is decreased. The results obtained open promising novel pathways for future advances in advanced materials and photocatalysis.

8.2 Outlook

Looking ahead, the future trajectory of research in the field of photoelectrochemical (PEC) water splitting holds great promise, particularly in the context of advancing materials beyond WO_3. In this pursuit, the intense pulsed ion beam (IPIB) technique, proven to be effective in surface modification, presents a compelling path for exploration and application across a broader spectrum of materials.

The versatility of IPIB, with its ability to introduce energetic ions deep into materials and induce super-fast annealing, positions it as a valuable tool for tailoring the surfaces of diverse compounds. By extending its application beyond WO_3, we believe that we can unlock the full potential of IPIB in optimizing the performance of different photoelectrode materials for PEC water splitting. This strategic shift towards a broader materials palette encompasses semiconductors, metal oxides, and other promising candidates, thereby expanding the scope of possibilities in the quest for efficient and sustainable hydrogen production.

Bibliography

Abohamzeh, E., Salehi, F., Sheikholeslami, M., Abbassi, R., & Khan, F. (2021). Review of hydrogen safety during storage, transmission, and applications processes. *Journal of Loss Prevention in the Process Industries*, *72*, 104569. https://doi.org/10.1016/j.jlp.2021.104569

Abouelela, M. M., Kawamura, G., & Matsuda, A. (2021). A review on plasmonic nanoparticle-semiconductor photocatalysts for water splitting. *Journal of Cleaner Production*, *294*, 126200. https://doi.org/10.1016/j.jclepro.2021.126200

Agreement, P. (2015). United Nations Framework Convention on Climate Change, Paris Agreement. *Ed*. https://unfccc.int/process-and-meetings/ the-paris-agreement/the-paris-agreement

Ai, B., & Zhao, Y. (2018). Glancing angle deposition meets colloidal lithography: A new evolution in the design of nanostructures. *Nanophotonics*, *8*(1), 1–26. https://doi.org/10.1515/nanoph-2018-0105

Akal, D., Öztuna, S., & Büyükakın, M. K. (2020). A review of hydrogen usage in internal combustion engines (gasoline-Lpg-diesel) from combustion performance aspect. *International Journal of Hydrogen Energy*, *45*(60), 35257–35268. https://doi.org/10.1016/j.ijhydene.2020.02.001

Al-Ghussain, L. (2019). Global warming: Review on driving forces and mitigation: Global Warming: Review on Driving Forces and Mitigation. *Environmental Progress & Sustainable Energy*, *38*(1), 13–21. https://doi.org/10.1002/ep.13041

Ankudze, B., & Neglo, D. (2022). Green synthesis of silver nanoparticles from peel extract of Chrysophyllum albidum fruit and their antimicrobial synergistic potentials and biofilm inhibition properties. *BioMetals*. https://doi.org/10.1007/s10534-022-00483-5

Anpo, M., Kishiguchi, S., Ichihashi, Y., Takeuchi, M., Yamashita, H., Ikeue, K., Morin, B., Davidson, A., & Che, M. (2001). The design and development of second-generation titanium oxide photocatalysts able to operate under visible light irradiation by applying a

metal ion-implantation method. *Research on Chemical Intermediates*, *27*(4–5), 459–467. https://doi.org/10.1163/156856701104202101

Apolinário, A., Lopes, T., Costa, C., Araújo, J. P., & Mendes, A. M. (2019). Multilayered WO_3 Nanoplatelets for Efficient Photoelectrochemical Water Splitting: The Role of the Annealing Ramp. *ACS Applied Energy Materials*, *2*(2), 1040–1050. https://doi.org/10.1021/acsaem.8b01530

Araújo, A., Mendes, M. J., Mateus, T., Costa, J., Nunes, D., Fortunato, E., Águas, H., & Martins, R. (2018). Ultra-fast plasmonic back reflectors production for light trapping in thin Si solar cells. *Solar Energy*, *174*, 786–792. https://doi.org/10.1016/j.solener.2018.08.068

Araújo, A., Mendes, M. J., Mateus, T., Vicente, A., Nunes, D., Calmeiro, T., Fortunato, E., Águas, H., & Martins, R. (2016). Influence of the Substrate on the Morphology of Self-Assembled Silver Nanoparticles by Rapid Thermal Annealing. *The Journal of Physical Chemistry C*, *120*(32), 18235–18242. https://doi.org/10.1021/acs.jpcc.6b04283

Askerbay, A., Molkenova, A., & Atabaev, T. Sh. (2020). Latent fingerprint detection with luminescent Y2O3:Eu3+ nanoparticles. *Materials Today: Proceedings*, *20*, 245–248. https://doi.org/10.1016/j.matpr.2019.10.042

Atabaev, T. Sh. (2018). Plasmon-enhanced solar water splitting with metal oxide nanostructures: A brief overview of recent trends. *Frontiers of Materials Science*, *12*(3), 207–213. https://doi.org/10.1007/s11706-018-0413-4

Ayodele, B. V., Abdullah, T. A. R. B. T., Alsaffar, M. A., Mustapa, S. I., & Salleh, S. F. (2020). Recent advances in renewable hydrogen production by thermo-catalytic conversion of biomass-derived glycerol: Overview of prospects and challenges. *International Journal of Hydrogen Energy*, *45*(36), 18160–18185. https://doi.org/10.1016/j.ijhydene.2019.08.002

Azam, A., Kim, J., Park, J., Novak, T. G., Tiwari, A. P., Song, S. H., Kim, B., & Jeon, S. (2018). Two-Dimensional WO_3 Nanosheets Chemically Converted from Layered WS_2 for High-Performance Electrochromic Devices. *Nano Letters*, *18*(9), 5646–5651. https://doi.org/10.1021/acs.nanolett.8b02150

Badán, J. A., Navarrete-Astorga, E., Henríquez, R., Jiménez, F. M., Ariosa, D., Ramos-Barrado, J. R., & Dalchiele, E. A. (2022). Silver Nanoparticle Arrays onto Glass Substrates Obtained by Solid-State Thermal Dewetting: A Morphological, Structural and Surface Chemical Study. *Nanomaterials*, *12*(4), 617. https://doi.org/10.3390/nano12040617

Bai, Y., Gao, Z., Chen, N., Liu, H., Yao, J., Ma, S., & Shi, X. (2014). Elimination of small-sized Ag nanoparticles via rapid thermal annealing for high efficiency light trapping structure. *Applied Surface Science*, *315*, 1–7. https://doi.org/10.1016/j.apsusc.2014.07.029

Bandi, S., & Srivastav, A. K. (2021). Review: Oxygen-deficient tungsten oxides. *Journal of Materials Science*, *56*(11), 6615–6644. https://doi.org/10.1007/s10853-020-05757-2

Bao, K., Mao, W., Liu, G., Ye, L., Xie, H., Ji, S., Wang, D., Chen, C., & Li, Y. (2017). Preparation and electrochemical characterization of ultrathin WO3−x /C nanosheets as anode materials in lithium ion batteries. *Nano Research*, *10*(6), 1903–1911. https://doi.org/10.1007/s12274-016-1373-6

Bard, A. J., & Fox, M. A. (1995). Artificial Photosynthesis: Solar Splitting of Water to Hydrogen and Oxygen. *Accounts of Chemical Research*, *28*(3), 141–145. https://doi.org/10.1021/ar00051a007

Belessiotis, G. V., & Kontos, A. G. (2022). Plasmonic silver (Ag)-based photocatalysts for H2 production and CO2 conversion: Review, analysis and perspectives. *Renewable Energy*, *195*, 497–515. https://doi.org/10.1016/j.renene.2022.06.044

Besozzi, E., Dellasega, D., Russo, V., Conti, C., Passoni, M., & Beghi, M. G. (2019). Thermomechanical properties of amorphous metallic tungsten-oxygen and tungsten-oxide coatings. *Materials & Design*, *165*, 107565. https://doi.org/10.1016/j.matdes.2018.107565

Bhalla, N., Jain, A., Lee, Y., Shen, A. Q., & Lee, D. (2019). Dewetting Metal Nanofilms—Effect of Substrate on Refractive Index Sensitivity of Nanoplasmonic Gold. *Nanomaterials*, *9*(11), 1530. https://doi.org/10.3390/nano9111530

Bhattacharyya, S. R., Datta, D., Shyjumon, I., Smirnov, B. M., Chini, T. K., Ghose, D., & Hippler, R. (2009). Growth and melting of silicon supported silver nanocluster films. *Journal of Physics D: Applied Physics*, *42*(3), 035306. https://doi.org/10.1088/0022-3727/42/3/035306

Bin Adnan, M. A., Arifin, K., Minggu, L. J., & Kassim, M. B. (2018). Titanate-based perovskites for photochemical and photoelectrochemical water splitting applications: A review. *International Journal of Hydrogen Energy*, *43*(52), 23209–23220. https://doi.org/10.1016/j.ijhydene.2018.10.173

Boateng, E., Thind, S. S., Chen, S., & Chen, A. (2022). Synthesis and electrochemical studies of WO_3 -based nanomaterials for environmental, energy and gas sensing applications. *Electrochemical Science Advances*, *2*(5). https://doi.org/10.1002/elsa.202100146

Bondarenko, A.S., Ragoisha, G.A., & Pomerantsev, A.L. (2005). Progress in Chemometrics Research; Pomerantsev, A.L., Ed.; *Nova Science Publishers: New York, NY, USA*, 89-102.

Brandon, D. G., & Kaplan, W. D. (2010). *Microstructural characterization of materials* (2. ed., repr). Wiley.

Bulíř, J. (2011). Preparation of nanostructured ultrathin silver layer. *Journal of Nanophotonics*, *5*(1), 051511. https://doi.org/10.1117/1.3562568

Chaabouni, F., Abaab, M., & Rezig, B. (2004). Effect of the substrate temperature on the properties of ZnO films grown by RF magnetron sputtering. *Materials Science and Engineering: B*, *109*(1–3), 236–240. https://doi.org/10.1016/j.mseb.2003.10.105

Chae, S. Y., Lee, C. S., Jung, H., Joo, O.-S., Min, B. K., Kim, J. H., & Hwang, Y. J. (2017). Insight into Charge Separation in WO_3 /$BiVO_4$ Heterojunction for Solar Water Splitting. *ACS Applied Materials & Interfaces*, *9*(23), 19780–19790. https://doi.org/10.1021/acsami.7b02486

Chandrasekaran, S., Zhang, P., Peng, F., Bowen, C., Huo, J., & Deng, L. (2019). Tailoring the geometric and electronic structure of tungsten oxide with manganese or vanadium

doping toward highly efficient electrochemical and photoelectrochemical water splitting. *Journal of Materials Chemistry A*, *7*(11), 6161–6172. https://doi.org/10.1039/C8TA12238E

Chen, B., Zhang, Z., Baek, M., Kim, S., Kim, W., & Yong, K. (2018). An antenna/spacer/reflector based Au/BiVO4/WO3/Au nanopatterned photoanode for plasmon-enhanced photoelectrochemical water splitting. *Applied Catalysis B: Environmental*, *237*, 763–771. https://doi.org/10.1016/j.apcatb.2018.06.048

Costa, M. B., de Araújo, M. A., Tinoco, M. V. de L., Brito, J. F. de, & Mascaro, L. H. (2022). Current trending and beyond for solar-driven water splitting reaction on WO3 photoanodes. *Journal of Energy Chemistry*, *73*, 88–113. https://doi.org/10.1016/j.jechem.2022.06.003

Crowley-Vigneau, A., Kalyuzhnova, Y., & Ketenci, N. (2023). What motivates the 'green' transition: Russian and European perspectives. *Resources Policy*, *81*, 103128. https://doi.org/10.1016/j.resourpol.2022.103128

Dai, D., Tu, X., Li, X., Lv, T., & Han, F. (2019). Tuning solar absorption spectra via carbon quantum dots/VAE composite layer and efficiency enhancement for crystalline Si solar module. *Progress in Photovoltaics: Research and Applications*, *27*(4), 283–289. https://doi.org/10.1002/pip.3109

Dang, X., Jiang, X., Zhang, T., & Zhao, H. (2021). WO_3 Inversce Opal Photonic Crystals: Unique Property, Synthetic Methods and Extensive Application. *Chinese Journal of Chemistry*, *39*(6), 1706–1715. https://doi.org/10.1002/cjoc.202000687

de Respinis, M., De Temmerman, G., Tanyeli, I., van de Sanden, M. C. M., Doerner, R. P., Baldwin, M. J., & van de Krol, R. (2013). Efficient Plasma Route to Nanostructure Materials: Case Study on the Use of m-WO_3 for Solar Water Splitting. *ACS Applied Materials & Interfaces*, *5*(15), 7621–7625. https://doi.org/10.1021/am401936q

Dellasega, D., Pietralunga, S. M., Pezzoli, A., Russo, V., Nasi, L., Conti, C., Vahid, M. J., Tagliaferri, A., & Passoni, M. (2015). Tungsten oxide nanowires grown on amorphous-

like tungsten films. *Nanotechnology*, *26*(36), 365601. https://doi.org/10.1088/0957-4484/26/36/365601

Demir, K. Ç. (2020). Corrosion behavior of electrodeposited Wo3 thin films. *Ceramics International*, *46*(4), 4358–4364. https://doi.org/10.1016/j.ceramint.2019.10.159

Di Fonzo, F., Bailini, A., Russo, V., Baserga, A., Cattaneo, D., Beghi, M. G., Ossi, P. M., Casari, C. S., Li Bassi, A., & Bottani, C. E. (2006). Synthesis and characterization of tungsten and tungsten oxide nanostructured films. *Catalysis Today*, *116*(1), 69–73. https://doi.org/10.1016/j.cattod.2006.02.080

Dias, P., Lopes, T., Meda, L., Andrade, L., & Mendes, A. (2016). Photoelectrochemical water splitting using WO_3 photoanodes: The substrate and temperature roles. *Physical Chemistry Chemical Physics*, *18*(7), 5232–5243. https://doi.org/10.1039/C5CP06851G

Dincer, I., & Acar, C. (2015). Review and evaluation of hydrogen production methods for better sustainability. *International Journal of Hydrogen Energy*, *40*(34), 11094–11111. https://doi.org/10.1016/j.ijhydene.2014.12.035

Efkere, H. İ., Gümrükçü, A. E., Özen, Y., Kınacı, B., Aydın, S. Ş., Ates, H., & Özçelik, S. (2021). Investigation of the effect of annealing on the structural, morphological and optical properties of RF sputtered WO3 nanostructure. *Physica B: Condensed Matter*, *622*, 413350. https://doi.org/10.1016/j.physb.2021.413350

Evanoff, D. D., & Chumanov, G. (2005). Synthesis and Optical Properties of Silver Nanoparticles and Arrays. *ChemPhysChem*, *6*(7), 1221–1231. https://doi.org/10.1002/cphc.200500113

Fàbrega, C., Murcia-López, S., Monllor-Satoca, D., Prades, J. D., Hernández-Alonso, M. D., Penelas, G., Morante, J. R., & Andreu, T. (2016). Efficient WO3 photoanodes fabricated by pulsed laser deposition for photoelectrochemical water splitting with high faradaic efficiency. *Applied Catalysis B: Environmental*, *189*, 133–140. https://doi.org/10.1016/j.apcatb.2016.02.047

Fang, Y., Lee, W. C., Canciani, G. E., Draper, T. C., Al-Bawi, Z. F., Bedi, J. S., Perry, C. C., & Chen, Q. (2015). Thickness control in electrophoretic deposition of WO3 nanofiber thin

films for solar water splitting. *Materials Science and Engineering: B*, *202*, 39–45. https://doi.org/10.1016/j.mseb.2015.09.005

Farhang, A., Bigler, N., & Martin, O. J. F. (2013). Coupling of multiple LSP and SPP resonances: Interactions between an elongated nanoparticle and a thin metallic film. *Optics Letters*, *38*(22), 4758. https://doi.org/10.1364/OL.38.004758

Fathima, H., Mohandas, N., Varghese, B. S., Anupkumar, P., Swathi, R. S., & Thomas, K. G. (2021). Core–Shell Plasmonic Nanostructures on Au Films as SERS Substrates: Thickness of Film and Quality Factor of Nanoparticle Matter. *The Journal of Physical Chemistry C*, *125*(29), 16024–16032. https://doi.org/10.1021/acs.jpcc.1c02339

Fernández-Domene, R. M., Cháfer-Ortega, A., Lombana-Fernández, J. A., Sánchez-Tovar, R., & Solsona, B. (2023). Ionic liquids and nanotechnology: Synthesis of WO3 nanostructures by anodization as photoelectrocatalysts. *Ceramics International*, *49*(10), 15434–15441. https://doi.org/10.1016/j.ceramint.2023.01.128

Figueroa, R., Cruz, T. G. S., & Gorenstein, A. (2007). WO3 pillar-type and helical-type thin film structures to be used in microbatteries. *Journal of Power Sources*, *172*(1), 422–427. https://doi.org/10.1016/j.jpowsour.2007.05.080

Fujishima, A., & Honda, K. (1972). Electrochemical Photolysis of Water at a Semiconductor Electrode. *Nature*, *238*(5358), 37–38. https://doi.org/10.1038/238037a0

Gangwar, M. S., & Agarwal, P. (2021). *Effect of the annealing temperature on the growth of the silver nanoparticles synthesized by physical route*. 020100. https://doi.org/10.1063/5.0061110

Ghazal, S., Mirzaee, M., & Darroudi, M. (2022). Green synthesis of tungsten oxide (WO_3) nanosheets and investigation of their photocatalytic and cytotoxicity effects. *Micro & Nano Letters*, *17*(11), 286–298. https://doi.org/10.1049/mna2.12134

Gomes Silva, C., Juárez, R., Marino, T., Molinari, R., & García, H. (2011). Influence of Excitation Wavelength (UV or Visible Light) on the Photocatalytic Activity of Titania Containing Gold

Nanoparticles for the Generation of Hydrogen or Oxygen from Water. *Journal of the American Chemical Society*, *133*(3), 595–602. https://doi.org/10.1021/ja1086358

Gu, C., Jia, A.-B., Zhang, Y.-M., & Zhang, S. X.-A. (2022). Emerging Electrochromic Materials and Devices for Future Displays. *Chemical Reviews*, *122*(18), 14679–14721. https://doi.org/10.1021/acs.chemrev.1c01055

Guerin, S., & Hayden, B. E. (2006). Physical Vapor Deposition Method for the High-Throughput Synthesis of Solid-State Material Libraries. *Journal of Combinatorial Chemistry*, *8*(1), 66–73. https://doi.org/10.1021/cc050117p

Gullapalli, S. K., Vemuri, R. S., & Ramana, C. V. (2010). Structural transformation induced changes in the optical properties of nanocrystalline tungsten oxide thin films. *Applied Physics Letters*, *96*(17), 171903. https://doi.org/10.1063/1.3421540

Gupta, R. B. (Ed.). (2008). *Hydrogen Fuel: Production, Transport, and Storage* (0 ed.). CRC Press. https://doi.org/10.1201/9781420045772

Gutpa, J., Shaik, H., Naveen Kumar, K., & Sattar, S. A. (2022). PVD techniques proffering avenues for fabrication of porous tungsten oxide (WO3) thin films: A review. *Materials Science in Semiconductor Processing*, *143*, 106534. https://doi.org/10.1016/j.mssp.2022.106534

Hamdani, I. R., & Bhaskarwar, A. N. (2021). Recent progress in material selection and device designs for photoelectrochemical water-splitting. *Renewable and Sustainable Energy Reviews*, *138*, 110503. https://doi.org/10.1016/j.rser.2020.110503

Hammond, Christopher. (2015). *The basics of crystallography and diffraction.* (Vol. 21). International Union of Crystallography texts on crystallography.

Hannah Ritchie, Max Roser, & Pablo Rosado. (2022). *"Energy". Published online at OurWorldInData.org. Retrieved from: 'https://ourworldindata.org/energy.'* Online Resource. https://ourworldindata.org/energy'

Hansen, J., Sato, M., Ruedy, R., Lo, K., Lea, D. W., & Medina-Elizade, M. (2006). Global temperature change. *Proceedings of the National Academy of Sciences*, *103*(39), 14288–14293. https://doi.org/10.1073/pnas.0606291103

Hassanpouryouzband, A., Joonaki, E., Edlmann, K., Heinemann, N., & Yang, J. (2020). Thermodynamic and transport properties of hydrogen containing streams. *Scientific Data*, *7*(1), 222. https://doi.org/10.1038/s41597-020-0568-6

Hayat, M. B., Ali, D., Monyake, K. C., Alagha, L., & Ahmed, N. (2019). Solar energy-A look into power generation, challenges, and a solar-powered future. *International Journal of Energy Research*, *43*(3), 1049–1067. https://doi.org/10.1002/er.4252

Hjelm, A., Granqvist, C. G., & Wills, J. M. (1996). Electronic structure and optical properties of WO 3 , LiWO 3 , NaWO 3 , and HWO 3. *Physical Review B*, *54*(4), 2436–2445. https://doi.org/10.1103/PhysRevB.54.2436

Hodes, G., Cahen, D., & Manassen, J. (1976). Tungsten trioxide as a photoanode for a photoelectrochemical cell (PEC). *Nature*, *260*(5549), 312–313. https://doi.org/10.1038/260312a0

Hooshmand, N., Panikkanvalappil, S. R., & El-Sayed, M. A. (2016). Effects of the Substrate Refractive Index, the Exciting Light Propagation Direction, and the Relative Cube Orientation on the Plasmonic Coupling Behavior of Two Silver Nanocubes at Different Separations. *The Journal of Physical Chemistry C*, *120*(37), 20896–20904. https://doi.org/10.1021/acs.jpcc.6b02480

Hou, B., Shen, L., Shi, H., Kapadia, R., & Cronin, S. B. (2017). Hot electron-driven photocatalytic water splitting. *Physical Chemistry Chemical Physics*, *19*(4), 2877–2881. https://doi.org/10.1039/C6CP07542H

Hu, Q., He, J., Chang, J., Gao, J., Huang, J., & Feng, L. (2020). Needle-Shaped WO_3 Nanorods for Triethylamine Gas Sensing. *ACS Applied Nano Materials*, *3*(9), 9046–9054. https://doi.org/10.1021/acsanm.0c01731

Huang, Z.-F., Song, J., Pan, L., Zhang, X., Wang, L., & Zou, J.-J. (2015). Tungsten Oxides for Photocatalysis, Electrochemistry, and Phototherapy. *Advanced Materials*, *27*(36), 5309–5327. https://doi.org/10.1002/adma.201501217

Hwan Cho, S., Min Suh, J., Jeong, B., Hyung Lee, T., Soon Choi, K., Hoon Eom, T., Kim, T., & Won Jang, H. (2022). Fast responding and highly reversible gasochromic H2 sensor using Pd-decorated amorphous WO3 thin films. *Chemical Engineering Journal*, *446*, 136862. https://doi.org/10.1016/j.cej.2022.136862

Hwang, T., Fukuda, M., Nogami, S., Hasegawa, A., Usami, H., Yabuuchi, K., Ozawa, K., & Tanigawa, H. (2016). Effect of self-ion irradiation on hardening and microstructure of tungsten. *Nuclear Materials and Energy*, *9*, 430–435. https://doi.org/10.1016/j.nme.2016.06.005

Introduction to Dislocations. (2011). Elsevier. https://doi.org/10.1016/C2009-0-64358-0

Jain, P. K., Huang, X., El-Sayed, I. H., & El-Sayed, M. A. (2008). Noble Metals on the Nanoscale: Optical and Photothermal Properties and Some Applications in Imaging, Sensing, Biology, and Medicine. *Accounts of Chemical Research*, *41*(12), 1578–1586. https://doi.org/10.1021/ar7002804

Jaiswal, M. K., & Choudhury, B. (2022). Hydrated Orthorhombic/Hexagonal Mixed-Phase WO_3 Core–Shell Nanoribbons for Hole-Mediated Photocatalysis. *ACS Applied Nano Materials*, *5*(3), 3599–3610. https://doi.org/10.1021/acsanm.1c04267

Jamali, M., & Shariatmadar Tehrani, F. (2020). Effect of synthesis route on the structural and morphological properties of WO3 nanostructures. *Materials Science in Semiconductor Processing*, *107*, 104829. https://doi.org/10.1016/j.mssp.2019.104829

Jia, J., Seitz, L. C., Benck, J. D., Huo, Y., Chen, Y., Ng, J. W. D., Bilir, T., Harris, J. S., & Jaramillo, T. F. (2016). Solar water splitting by photovoltaic-electrolysis with a solar-to-hydrogen efficiency over 30%. *Nature Communications*, *7*(1), 13237. https://doi.org/10.1038/ncomms13237

Jiang, M., Zhang, G., Li, C., Liu, J., Guo, K., Ning, H., Shi, M., Guo, D., Yao, R., & Peng, J. (2020). Effects of rapid thermal annealing on wide band gap tungsten oxide films. *Superlattices and Microstructures*, *142*, 106541. https://doi.org/10.1016/j.spmi.2020.106541

Jiao, Z., Wang, J., Ke, L., Sun, X. W., & Demir, H. V. (2011). Morphology-Tailored Synthesis of Tungsten Trioxide (Hydrate) Thin Films and Their Photocatalytic Properties. *ACS Applied Materials & Interfaces*, *3*(2), 229–236. https://doi.org/10.1021/am100875z

Kaikanov, M., Amanzhulov, B., Demeuova, G., Akhtanova, G., Bozheyev, F., Kemelbay, A., & Tikhonov, A. (2020). Modification of Silver Nanowire Coatings with Intense Pulsed Ion Beam for Transparent Heaters. *Nanomaterials*, *10*(11), 2153. https://doi.org/10.3390/nano10112153

Kaikanov, M., Baigarin, K., Tikhonov, A., Urazbayev, A., Kwan, J. W., Henestroza, E., Remnev, G., Shubin, B., Stepanov, A., Shamanin, V., & Waldron, W. L. (2016). An accelerator facility for WDM, HEDP, and HIF investigations in Nazarbayev University. *Journal of Physics: Conference Series*, *717*, 012099. https://doi.org/10.1088/1742-6596/717/1/012099

Kaikanov, M., Kemelbay, A., Amanzhulov, B., Demeuova, G., Akhtanova, G., Bozheyev, F., & Tikhonov, A. (2021). Electrical conductivity enhancement of transparent silver nanowire films on temperature-sensitive flexible substrates using intense pulsed ion beam. *Nanotechnology*, *32*(14), 145706. https://doi.org/10.1088/1361-6528/abd49e

Kalai Priya, A., Yogesh, G. K., Subha, K., Kalyanavalli, V., & Sastikumar, D. (2021). Synthesis of silver nano-butterfly park by using laser ablation of aqueous salt for gas sensing application. *Applied Physics A*, *127*(4), 292. https://doi.org/10.1007/s00339-021-04370-7

Kalanur, S. S. (2019). Structural, Optical, Band Edge and Enhanced Photoelectrochemical Water Splitting Properties of Tin-Doped WO3. *Catalysts*, *9*(5), 456. https://doi.org/10.3390/catal9050456

Kalanur, S. S., Noh, Y.-G., & Seo, H. (2020). Engineering band edge properties of WO3 with respect to photoelectrochemical water splitting potentials via a generalized doping protocol of first-row transition metal ions. *Applied Surface Science*, *509*, 145253. https://doi.org/10.1016/j.apsusc.2020.145253

Kalanur, S. S., & Seo, H. (2018). Influence of molybdenum doping on the structural, optical and electronic properties of WO3 for improved solar water splitting. *Journal of Colloid and Interface Science*, *509*, 440–447. https://doi.org/10.1016/j.jcis.2017.09.025

Kalanur, S. S., & Seo, H. (2019). Intercalation of barium into monoclinic tungsten oxide nanoplates for enhanced photoelectrochemical water splitting. *Chemical Engineering Journal*, *355*, 784–796. https://doi.org/10.1016/j.cej.2018.08.210

Kalanur, S. S., Singh, R., & Seo, H. (2021). Enhanced solar water splitting of an ideally doped and work function tuned {002} oriented one-dimensional WO3 with nanoscale surface charge mapping insights. *Applied Catalysis B: Environmental*, *295*, 120269. https://doi.org/10.1016/j.apcatb.2021.120269

Kalanur, S. S., Yoo, I.-H., Cho, I.-S., & Seo, H. (2019). Effect of oxygen vacancies on the band edge properties of WO3 producing enhanced photocurrents. *Electrochimica Acta*, *296*, 517–527. https://doi.org/10.1016/j.electacta.2018.11.061

Kalanur, S. S., Yoo, I.-H., Eom, K., & Seo, H. (2018). Enhancement of photoelectrochemical water splitting response of WO3 by Means of Bi doping. *Journal of Catalysis*, *357*, 127–137. https://doi.org/10.1016/j.jcat.2017.11.012

Kalanur, S. S., Yoo, I.-H., & Seo, H. (2017). Fundamental investigation of Ti doped WO3 photoanode and their influence on photoelectrochemical water splitting activity. *Electrochimica Acta*, *254*, 348–357. https://doi.org/10.1016/j.electacta.2017.09.142

Kozlovskiy, A. L., Alina, A., & Zdorovets, M. V. (2021). Study of the effect of ion irradiation on increasing the photocatalytic activity of WO3 microparticles. *Journal of Materials Science: Materials in Electronics*, *32*(3), 3863–3877. https://doi.org/10.1007/s10854-020-05130-8

Kozlovskiy, A. L., & Zdorovets, M. V. (2020). Study of the photocatalytic activity of irradiated WO3 microparticles. *Applied Physics A*, *126*(8), 638. https://doi.org/10.1007/s00339-020-03827-5

Kunwar, S., Sui, M., Zhang, Q., Pandey, P., Li, M.-Y., & Lee, J. (2017). Various Silver Nanostructures on SapphireUsing Plasmon Self-Assembly and Dewetting of Thin Films. *Nano-Micro Letters*, *9*(2), 17. https://doi.org/10.1007/s40820-016-0120-6

Le, H. V., Pham, P. T., Le, L. T., Nguyen, A. D., Tran, N. Q., & Tran, P. D. (2021). Fabrication of tungsten oxide photoanode by doctor blade technique and investigation on its photocatalytic operation mechanism. *International Journal of Hydrogen Energy*, *46*(44), 22852–22863. https://doi.org/10.1016/j.ijhydene.2021.04.113

Lee, S.-H., Deshpande, R., Parilla, P. A., Jones, K. M., To, B., Mahan, A. H., & Dillon, A. C. (2006). Crystalline WO3 Nanoparticles for Highly Improved Electrochromic Applications. *Advanced Materials*, *18*(6), 763–766. https://doi.org/10.1002/adma.200501953

Leroy, F., Borowik, Ł., Cheynis, F., Almadori, Y., Curiotto, S., Trautmann, M., Barbé, J. C., & Müller, P. (2016). How to control solid state dewetting: A short review. *Surface Science Reports*, *71*(2), 391–409. https://doi.org/10.1016/j.surfrep.2016.03.002

Li, J., Lou, Z., & Li, B. (2021). Engineering plasmonic semiconductors for enhanced photocatalysis. *Journal of Materials Chemistry A*, *9*(35), 18818–18835. https://doi.org/10.1039/D1TA04541E

Li, L., Lin, J., Wu, N., Xie, S., Meng, C., Zheng, Y., Wang, X., & Zhao, Y. (2022). Review and outlook on the international renewable energy development. *Energy and Built Environment*, *3*(2), 139–157. https://doi.org/10.1016/j.enbenv.2020.12.002

Li, Y., McMaster, W. A., Wei, H., Chen, D., & Caruso, R. A. (2018). Enhanced Electrochromic Properties of WO_3 Nanotree-like Structures Synthesized via a Two-Step Solvothermal Process Showing Promise for Electrochromic Window Application. *ACS Applied Nano Materials*, *1*(6), 2552–2558. https://doi.org/10.1021/acsanm.8b00190

Li, Y., Tang, Z., Zhang, J., & Zhang, Z. (2016). Defect Engineering of Air-Treated WO_3 and Its Enhanced Visible-Light-Driven Photocatalytic and Electrochemical Performance. *The Journal of Physical Chemistry C*, *120*(18), 9750–9763. https://doi.org/10.1021/acs.jpcc.6b00457

Limwichean, S., Kasayapanand, N., Ponchio, C., Nakajima, H., Patthanasettakul, V., Eiamchai, P., Meng, G., & Horprathum, M. (2021). Morphology-controlled fabrication of nanostructured WO3 thin films by magnetron sputtering with glancing angle deposition for enhanced efficiency photo-electrochemical water splitting. *Ceramics International*, *47*(24), 34455–34462. https://doi.org/10.1016/j.ceramint.2021.08.359

Linic, S., Christopher, P., & Ingram, D. B. (2011). Plasmonic-metal nanostructures for efficient conversion of solar to chemical energy. *Nature Materials*, *10*(12), 911–921. https://doi.org/10.1038/nmat3151

Liu, D., & Xue, C. (2021). Plasmonic Coupling Architectures for Enhanced Photocatalysis. *Advanced Materials*, *33*(46), 2005738. https://doi.org/10.1002/adma.202005738

Liu, X., Wang, F., & Wang, Q. (2012). Nanostructure-based WO3 photoanodes for photoelectrochemical water splitting. *Physical Chemistry Chemical Physics*, *14*(22), 7894. https://doi.org/10.1039/c2cp40976c

Liu, Y., Wygant, B. R., Mabayoje, O., Lin, J., Kawashima, K., Kim, J.-H., Li, W., Li, J., & Mullins, C. B. (2018). Interface Engineering and its Effect on WO_3 -Based Photoanode and Tandem Cell. *ACS Applied Materials & Interfaces*, *10*(15), 12639–12650. https://doi.org/10.1021/acsami.8b00304

Liu, Z., Hou, W., Pavaskar, P., Aykol, M., & Cronin, S. B. (2011). Plasmon Resonant Enhancement of Photocatalytic Water Splitting Under Visible Illumination. *Nano Letters*, *11*(3), 1111–1116. https://doi.org/10.1021/nl104005n

Lou, B.-S., Chen, W.-T., Diyatmika, W., Lu, J.-H., Chang, C.-T., Chen, P.-W., & Lee, J.-W. (2022). High power impulse magnetron sputtering (HiPIMS) for the fabrication of

antimicrobial and transparent TiO2 thin films. *Current Opinion in Chemical Engineering*, *36*, 100782. https://doi.org/10.1016/j.coche.2021.100782

Ma, S., Li, Y., Luo, X., Zhao, S., Cao, Z., Ding, Y., Cui, D., Zhou, N., Wang, L., & Ran, G. (2023). Dislocation-rich BiOI nanosheets designed by nitrogen ion implantation for improving NIR-triggered bactericidal activity. *Materials Today Energy*, *31*, 101214. https://doi.org/10.1016/j.mtener.2022.101214

Ma, S., Zeng, L., Tao, L., Tang, C. Y., Yuan, H., Long, H., Cheng, P. K., Chai, Y., Chen, C., Fung, K. H., Zhang, X., Lau, S. P., & Tsang, Y. H. (2017). Enhanced Photocatalytic Activity of WS2 Film by Laser Drilling to Produce Porous WS2/WO3 Heterostructure. *Scientific Reports*, *7*(1), 3125. https://doi.org/10.1038/s41598-017-03254-2

Ma, X., Zhang, G., Wang, G., Zhu, G., Zhou, W., Wang, J., & Sun, B. (2014). Surface morphology, microstructure and properties of as-cast AZ31 magnesium alloy irradiated by high intensity pulsed ion beams. *Applied Surface Science*, *311*, 567–573. https://doi.org/10.1016/j.apsusc.2014.05.109

Makola, L. C., Moeno, S., Ouma, C. N. M., & Dlamini, L. N. (2023). MXene mediated layered 2D-2D-3D g-C3N4@Ti3C2T@WO3 multijunctional heterostructure with enhanced photoelectrochemical and photocatalytic properties. *Nano-Structures & Nano-Objects*, *33*, 100934. https://doi.org/10.1016/j.nanoso.2022.100934

Makuła, P., Pacia, M., & Macyk, W. (2018). How To Correctly Determine the Band Gap Energy of Modified Semiconductor Photocatalysts Based on UV–Vis Spectra. *The Journal of Physical Chemistry Letters*, *9*(23), 6814–6817. https://doi.org/10.1021/acs.jpclett.8b02892

Malik, U., Korcoban, D., Mehla, S., Kandjani, A. E., Sabri, Y. M., Balendhran, S., & Bhargava, S. K. (2022). Fabrication of fractal structured soot templated titania-silver nano-surfaces for photocatalysis and SERS sensing. *Applied Surface Science*, *594*, 153383. https://doi.org/10.1016/j.apsusc.2022.153383

Mandlekar, B. K., Jadhav, A. L., Jadhav, S. L., Khan, A., & Kadam, A. V. (2023). Binder-free room-temperature synthesis of amorphous-WO3 thin film on FTO, ITO, and stainless steel by electrodeposition for electrochromic application. *Optical Materials*, *136*, 113460. https://doi.org/10.1016/j.optmat.2023.113460

Marhaba, S. (2018). Effect of Size, Shape and Environment on the Optical Response of Metallic Nanoparticles. In M. S. Seehra & A. D. Bristow (Eds.), *Noble and Precious Metals—Properties, Nanoscale Effects and Applications*. InTech. https://doi.org/10.5772/intechopen.71574

Markhabayeva, A. A., Moniruddin, M., Dupre, R., Abdullin, K. A., & Nuraje, N. (2020). Designing of WO_3@Co_3O_4 Heterostructures to Enhance Photoelectrochemical Performances. *The Journal of Physical Chemistry A*, *124*(3), 486–491. https://doi.org/10.1021/acs.jpca.9b09173

Martins, A. S., Guaraldo, T. T., Wenk, J., Mattia, D., & Boldrin Zanoni, M. V. (2022). Nanoporous WO3 grown on a 3D tungsten mesh by electrochemical anodization for enhanced photoelectrocatalytic degradation of tetracycline in a continuous flow reactor. *Journal of Electroanalytical Chemistry*, *920*, 116617. https://doi.org/10.1016/j.jelechem.2022.116617

Masoumi, Z., Tayebi, M., Kolaei, M., & Lee, B.-K. (2022). Efficient and stable core-shell α–Fe2O3/WS2/WOx photoanode for oxygen evolution reaction to enhance photoelectrochemical water splitting. *Applied Catalysis B: Environmental*, *313*, 121447. https://doi.org/10.1016/j.apcatb.2022.121447

Maxim, A. A., Sadyk, S. N., Aidarkhanov, D., Surya, C., Ng, A., Hwang, Y.-H., Atabaev, T. Sh., & Jumabekov, A. N. (2020). PMMA Thin Film with Embedded Carbon Quantum Dots for Post-Fabrication Improvement of Light Harvesting in Perovskite Solar Cells. *Nanomaterials*, *10*(2), 291. https://doi.org/10.3390/nano10020291

Migas, D. B., Shaposhnikov, V. L., Rodin, V. N., & Borisenko, V. E. (2010). Tungsten oxides. I. Effects of oxygen vacancies and doping on electronic and optical properties of different

phases of WO3. *Journal of Applied Physics*, *108*(9), 093713. https://doi.org/10.1063/1.3505688

Mirzaei, A., Kim, J.-H., Kim, H. W., & Kim, S. S. (2019). Gasochromic WO3 Nanostructures for the Detection of Hydrogen Gas: An Overview. *Applied Sciences*, *9*(9), 1775. https://doi.org/10.3390/app9091775

Mohamedkhair, A. K., Drmosh, Q. A., Qamar, M., & Yamani, Z. H. (2020). Nanostructured Magnéli-Phase W18O49 Thin Films for Photoelectrochemical Water Splitting. *Catalysts*, *10*(5), 526. https://doi.org/10.3390/catal10050526

Mohamedkhair, A. K., Drmosh, Q. A., Qamar, M., & Yamani, Z. H. (2021). Tuning Structural Properties of WO3 Thin Films for Photoelectrocatalytic Water Oxidation. *Catalysts*, *11*(3), 381. https://doi.org/10.3390/catal11030381

Najafi-Ashtiani, H. (2019). The effect of different surface morphologies on WO3 and WO3-Au gas-sensors performance. *Journal of Materials Science: Materials in Electronics*, *30*(13), 12224–12233. https://doi.org/10.1007/s10854-019-01581-w

Nakagawa, Y., Hayashi, Y., Yang, S., & Shibayama, T. (2022). Effects of gas phase ion irradiation and vacuum annealing on the visible light photocatalytic properties of WO3. *Vacuum*, *206*, 111519. https://doi.org/10.1016/j.vacuum.2022.111519

Nakate, U. T., Singh, V. K., Yu, Y. T., & Park, S. (2021). WO3 nanorods structures for high-performance gas sensing application. *Materials Letters*, *299*, 130092. https://doi.org/10.1016/j.matlet.2021.130092

Nazir, M. S., Ali, N., Bilal, M., & Iqbal, H. M. N. (2020). Potential environmental impacts of wind energy development: A global perspective. *Current Opinion in Environmental Science & Health*, *13*, 85–90. https://doi.org/10.1016/j.coesh.2020.01.002

Ng, C., Ng, Y. H., Iwase, A., & Amal, R. (2013). Influence of Annealing Temperature of WO_3 in Photoelectrochemical Conversion and Energy Storage for Water Splitting. *ACS Applied Materials & Interfaces*, *5*(11), 5269–5275. https://doi.org/10.1021/am401112q

Ng, K. H., Lai, S. Y., Cheng, C. K., Cheng, Y. W., & Chong, C. C. (2021). Photocatalytic water splitting for solving energy crisis: Myth, Fact or Busted? *Chemical Engineering Journal*, *417*, 128847. https://doi.org/10.1016/j.cej.2021.128847

Ollitrault, J., Martin, N., Rauch, J.-Y., Sanchez, J.-B., & Berger, F. (2015). Improvement of ozone detection with GLAD WO3 films. *Materials Letters*, *155*, 1–3. https://doi.org/10.1016/j.matlet.2015.04.099

Paracchino, A., Laporte, V., Sivula, K., Grätzel, M., & Thimsen, E. (2011). Highly active oxide photocathode for photoelectrochemical water reduction. *Nature Materials*, *10*(6), 456–461. https://doi.org/10.1038/nmat3017

Patil, D., Wasson, M. K., Aravindan, S., Perumal, V., & Rao, P. V. (2019). Fabrication of silver nanoparticles-embedded antibacterial polymer surface through thermal annealing and soft molding technique. *Materials Research Express*, *6*(4), 045010. https://doi.org/10.1088/2053-1591/aaf916

Piekoszewski, J., & Langner, J. (1991). High intensity pulsed ion beams in material processing: Equipment and applications. *Nuclear Instruments and Methods in Physics Research Section B: Beam Interactions with Materials and Atoms*, *53*(2), 148–160. https://doi.org/10.1016/0168-583X(91)95650-3

Pihosh, Y., Turkevych, I., Mawatari, K., Uemura, J., Kazoe, Y., Kosar, S., Makita, K., Sugaya, T., Matsui, T., Fujita, D., Tosa, M., Kondo, M., & Kitamori, T. (2015). Photocatalytic generation of hydrogen by core-shell WO3/BiVO4 nanorods with ultimate water splitting efficiency. *Scientific Reports*, *5*(1), 11141. https://doi.org/10.1038/srep11141

Popov, A. I., Lushchik, A., Shablonin, E., Vasil'chenko, E., Kotomin, E. A., Moskina, A. M., & Kuzovkov, V. N. (2018). Comparison of the F-type center thermal annealing in heavy-ion and neutron irradiated Al2O3 single crystals. *Nuclear Instruments and Methods in Physics Research Section B: Beam Interactions with Materials and Atoms*, *433*, 93–97. https://doi.org/10.1016/j.nimb.2018.07.036

Quan, J., Zhang, J., Qi, X., Li, J., Wang, N., & Zhu, Y. (2017). A study on the correlation between the dewetting temperature of Ag film and SERS intensity. *Scientific Reports*, *7*(1), 14771. https://doi.org/10.1038/s41598-017-15372-y

Rahmani, M. B., Yaacob, M. H., & Sabri, Y. M. (2017). Hydrogen sensors based on 2D WO3 nanosheets prepared by anodization. *Sensors and Actuators B: Chemical*, *251*, 57–64. https://doi.org/10.1016/j.snb.2017.05.029

Rajeshwar, K., McConnell, R. D., & Licht, S. (Eds.). (2008). *Solar hydrogen generation: Toward a renewable energy future*. Springer.

Raka, Y. D., Karoliussen, H., Lien, K. M., & Burheim, O. S. (2020). Opportunities and challenges for thermally driven hydrogen production using reverse electrodialysis system. *International Journal of Hydrogen Energy*, *45*(2), 1212–1225. https://doi.org/10.1016/j.ijhydene.2019.05.126

Ram, J., Singh, R. G., Singh, F., Chauhan, V., Gupta, D., Kumar, V., Kumar, U., Yadav, B. C., & Kumar, R. (2020). Ion beam engineering in WO3-PEDOT: PSS hybrid nanocomposite thin films for gas sensing measurement at room temperature. *Inorganic Chemistry Communications*, *119*, 108000. https://doi.org/10.1016/j.inoche.2020.108000

Ramana, C. V., Utsunomiya, S., Ewing, R. C., Julien, C. M., & Becker, U. (2006). Structural Stability and Phase Transitions in WO_3 Thin Films. *The Journal of Physical Chemistry B*, *110*(21), 10430–10435. https://doi.org/10.1021/jp056664i

Reichelt, K., & Jiang, X. (1990). The preparation of thin films by physical vapour deposition methods. *Thin Solid Films*, *191*(1), 91–126. https://doi.org/10.1016/0040-6090(90)90277-K

Reimer, L. (1998). *Scanning Electron Microscopy: Physics of Image Formation and Microanalysis* (Vol. 45). Springer Berlin Heidelberg. https://doi.org/10.1007/978-3-540-38967-5

Remnev, G. E., Isakov, I. F., Opekounov, M. S., Matvienko, V. M., Ryzhkov, V. A., Struts, V. K., Grushin, I. I., Zakoutayev, A. N., Potyomkin, A. V., Tarbokov, V. A., Pushkaryov, A. N.,

Kutuzov, V. L., & Ovsyannikov, M. Yu. (1999). High intensity pulsed ion beam sources and their industrial applications. Surface and Coatings Technology, 114(2–3), 206–212. https://doi.org/10.1016/S0257-8972(99)00058-4

Righettoni, M., & Pratsinis, S. E. (2014). Annealing dynamics of WO 3 by in situ XRD. *Materials Research Bulletin*, *59*, 199–204. https://doi.org/10.1016/j.materresbull.2014.07.018

Roselló-Márquez, G., Fernández-Domene, R. M., Sánchez-Tovar, R., & García-Antón, J. (2020). Influence of annealing conditions on the photoelectrocatalytic performance of WO3 nanostructures. *Separation and Purification Technology*, *238*, 116417. https://doi.org/10.1016/j.seppur.2019.116417

Rosman, N. N., Yunus, R. M., Shah, N. R. A. M., Shah, R. M., Arifin, K., Minggu, L. J., & Ludin, N. A. (2022). An overview of co-catalysts on metal oxides for photocatalytic water splitting. *International Journal of Energy Research*, *46*(9), 11596–11619. https://doi.org/10.1002/er.8001

Samuel, E., Joshi, B., Kim, M.-W., Swihart, M. T., & Yoon, S. S. (2020). Morphology engineering of photoelectrodes for efficient photoelectrochemical water splitting. *Nano Energy*, *72*, 104648. https://doi.org/10.1016/j.nanoen.2020.104648

Sang, P., & Kim, J. H. (2022). Role of g-C3N4 in Fabrication of BiVO4/WO3 Z-scheme Heterojunction for high Photoelectrochemical Performances with Enhanced Light Harvesting. *International Journal of Precision Engineering and Manufacturing-Green Technology*. https://doi.org/10.1007/s40684-022-00478-0

Sankir, N. D & Sankir, M. (Eds.). (2018). *Photoelectrochemical Solar Cells*. John Wiley & Sons.

Santos, F. D., Ferreira, P. L., & Pedersen, J. S. T. (2022). The Climate Change Challenge: A Review of the Barriers and Solutions to Deliver a Paris Solution. *Climate*, *10*(5), 75. https://doi.org/10.3390/cli10050075

Sarkar, A., Chakraborty, A. K., & Bera, S. (2018). NiS/rGO nanohybrid: An excellent counter electrode for dye sensitized solar cell. *Solar Energy Materials and Solar Cells*, *182*, 314–320. https://doi.org/10.1016/j.solmat.2018.03.026

Sarnowska, M., Bienkowski, K., Barczuk, P. J., Solarska, R., & Augustynski, J. (2016). Highly Efficient and Stable Solar Water Splitting at (Na)WO_3 Photoanodes in Acidic Electrolyte Assisted by Non-Noble Metal Oxygen Evolution Catalyst. *Advanced Energy Materials*, *6*(14), 1600526. https://doi.org/10.1002/aenm.201600526

Sazali, N. (2020). Emerging technologies by hydrogen: A review. *International Journal of Hydrogen Energy*, *45*(38), 18753–18771. https://doi.org/10.1016/j.ijhydene.2020.05.021

Shabdan, Y., Markhabayeva, A., Bakranov, N., & Nuraje, N. (2020). Photoactive Tungsten-Oxide Nanomaterials for Water-Splitting. *Nanomaterials*, *10*(9), 1871. https://doi.org/10.3390/nano10091871

Shandilya, P., Sambyal, S., Sharma, R., Mandyal, P., & Fang, B. (2022). Properties, optimized morphologies, and advanced strategies for photocatalytic applications of WO3 based photocatalysts. *Journal of Hazardous Materials*, *428*, 128218. https://doi.org/10.1016/j.jhazmat.2022.128218

Shetty, C., & Priyam, A. (2022). A review on tidal energy technologies. *Materials Today: Proceedings*, *56*, 2774–2779. https://doi.org/10.1016/j.matpr.2021.10.020

Shin, S., Han, H. S., Kim, J. S., Park, I. J., Lee, M. H., Hong, K. S., & Cho, I. S. (2015). A tree-like nanoporous WO_3 photoanode with enhanced charge transport efficiency for photoelectrochemical water oxidation. *Journal of Materials Chemistry A*, *3*(24), 12920–12926. https://doi.org/10.1039/C5TA00823A

Shishkovsky, I. V., & Lebedev, P. N. (2011). Chemical and physical vapor deposition methods for nanocoatings. In *Nanocoatings and Ultra-Thin Films* (pp. 57–77). Elsevier. https://doi.org/10.1533/9780857094902.1.57

Sivakumar, R., Sanjeeviraja, C., Jayachandran, M., Gopalakrishnan, R., Sarangi, S. N., Paramanik, D., & Som, T. (2007). Modification of WO_3 thin films by MeV N^+-ion beam irradiation. *Journal of Physics: Condensed Matter*, *19*(18), 186204. https://doi.org/10.1088/0953-8984/19/18/186204

Solovan, M. M., Mostovyi, A. I., Aidarkhanov, D., Parkhomenko, H. P., Akhtanova, G., Schopp, N., Asare, E. A., Nauruzbayev, D., Kaikanov, M., Ng, A., & Brus, V. V. (2023). Extreme Radiation Resistance of Self-Powered High-Performance $Cs_{0.04}Rb_{0.04}(FA_{0.65}MA_{0.35})_{0.92}Pb(I_{0.85}Br_{0.14}Cl_{0.01})_3$ Perovskite Photodiodes. *Advanced Optical Materials*, *11*(10), 2203001. https://doi.org/10.1002/adom.202203001

Song, J., Huang, Z.-F., Pan, L., Zou, J.-J., Zhang, X., & Wang, L. (2015). Oxygen-Deficient Tungsten Oxide as Versatile and Efficient Hydrogenation Catalyst. *ACS Catalysis*, *5*(11), 6594–6599. https://doi.org/10.1021/acscatal.5b01522

Stepanov, A. D., Barnard, J. J., Friedman, A., Gilson, E. P., Grote, D. P., Ji, Q., Kaganovich, I. D., Persaud, A., Seidl, P. A., & Schenkel, T. (2018). Optimizing beam transport in rapidly compressing beams on the neutralized drift compression experiment-II. *Matter and Radiation at Extremes*, *3*(2), 78–84. https://doi.org/10.1016/j.mre.2018.01.001

Stober, I., & Bucher, K. (2021). *Geothermal Energy: From Theoretical Models to Exploration and Development*. Springer International Publishing. https://doi.org/10.1007/978-3-030-71685-1

Su, J., Guo, L., Bao, N., & Grimes, C. A. (2011). Nanostructured WO_3/$BiVO_4$ Heterojunction Films for Efficient Photoelectrochemical Water Splitting. *Nano Letters*, *11*(5), 1928–1933. https://doi.org/10.1021/nl2000743

Su, J., Zhang, T., & Wang, L. (2017). Engineered WO3 nanorods for conformal growth of WO3/BiVO4 core–shell heterojunction towards efficient photoelectrochemical water oxidation. *Journal of Materials Science: Materials in Electronics*, *28*(5), 4481–4491. https://doi.org/10.1007/s10854-016-6082-0

Svadkovski, I. V., Golosov, D. A., & Zavatskiy, S. M. (2002). Characterisation parameters for unbalanced magnetron sputtering systems. *Vacuum*, *68*(4), 283–290. https://doi.org/10.1016/S0042-207X(02)00385-8

Tamirat, A. G., Rick, J., Dubale, A. A., Su, W.-N., & Hwang, B.-J. (2016). Using hematite for photoelectrochemical water splitting: A review of current progress and challenges. *Nanoscale Horizons*, *1*(4), 243–267. https://doi.org/10.1039/C5NH00098J

Tan, H., Zhao, Z., Zhu, W., Coker, E. N., Li, B., Zheng, M., Yu, W., Fan, H., & Sun, Z. (2014). Oxygen Vacancy Enhanced Photocatalytic Activity of Pervoskite $SrTiO_3$. *ACS Applied Materials & Interfaces*, *6*(21), 19184–19190. https://doi.org/10.1021/am5051907

Tehri, N., Vashishth, A., Gahlaut, A., & Hooda, V. (2020). Biosynthesis, antimicrobial spectra and applications of silver nanoparticles: Current progress and future prospects. *Inorganic and Nano-Metal Chemistry*, 1–19. https://doi.org/10.1080/24701556.2020.1862212

Thompson, C. V. (2012). Solid-State Dewetting of Thin Films. *Annual Review of Materials Research*, *42*(1), 399–434. https://doi.org/10.1146/annurev-matsci-070511-155048

Tsai, M.-L., Tu, W.-C., Tang, L., Wei, T.-C., Wei, W.-R., Lau, S. P., Chen, L.-J., & He, J.-H. (2016). Efficiency Enhancement of Silicon Heterojunction Solar Cells via Photon Management Using Graphene Quantum Dot as Downconverters. *Nano Letters*, *16*(1), 309–313. https://doi.org/10.1021/acs.nanolett.5b03814

Uğurlu, E. (2022). Renewale Energy Sources and Climate Change Mitigation. In D. Kurochkin, M. J. Crawford, & E. V. Shabliy (Eds.), *Energy Policy Advancement* (pp. 69–92). Springer International Publishing. https://doi.org/10.1007/978-3-030-84993-1_4

Valerini, D., Hernández, S., Di Benedetto, F., Russo, N., Saracco, G., & Rizzo, A. (2016). Sputtered WO3 films for water splitting applications. *Materials Science in Semiconductor Processing*, *42*, 150–154. https://doi.org/10.1016/j.mssp.2015.09.013

Vemuri, R. S., Engelhard, M. H., & Ramana, C. V. (2012). Correlation between Surface Chemistry, Density, and Band Gap in Nanocrystalline WO_3 Thin Films. *ACS Applied Materials & Interfaces*, *4*(3), 1371–1377. https://doi.org/10.1021/am2016409

Wagner, H.-J., & Mathur, J. (2011). *Introduction to Hydro Energy Systems: Basics, Technology and Operation*. Springer Berlin Heidelberg. https://doi.org/10.1007/978-3-642-20709-9

Wang, L., Liu, Y., Han, G., & Zhao, H. (2023). Dual-band electrochromic film based on mesoporous h-WO3/o-WO3·H2O/r-TiO2 for high performance smart windows. *Solar Energy Materials and Solar Cells*, *250*, 112053. https://doi.org/10.1016/j.solmat.2022.112053

Wang, S., Fan, W., Liu, Z., Yu, A., & Jiang, X. (2018). Advances on tungsten oxide based photochromic materials: Strategies to improve their photochromic properties. *Journal of Materials Chemistry C*, *6*(2), 191–212. https://doi.org/10.1039/C7TC04189F

Wang, W., & Zhu, P. (2018). Red photoluminescent Eu^{3+} -doped Y_2O_3 nanospheres for LED-phosphor applications: Synthesis and characterization. *Optics Express*, *26*(26), 34820. https://doi.org/10.1364/OE.26.034820

Wang, X., Wan, W., Shen, S., Wu, H., Zhong, H., Jiang, C., & Ren, F. (2020). Application of ion beam technology in (photo)electrocatalytic materials for renewable energy. *Applied Physics Reviews*, *7*(4), 041303. https://doi.org/10.1063/5.0021322

Wang, Y., Shi, H., Cui, K., Zhang, L., Ge, S., & Yu, J. (2020). Reversible electron storage in tandem photoelectrochemical cell for light driven unassisted overall water splitting. *Applied Catalysis B: Environmental*, *275*, 119094. https://doi.org/10.1016/j.apcatb.2020.119094

Wang, Y., Tian, W., Chen, C., Xu, W., & Li, L. (2019). Tungsten Trioxide Nanostructures for Photoelectrochemical Water Splitting: Material Engineering and Charge Carrier Dynamic Manipulation. *Advanced Functional Materials*, *29*(23), 1809036. https://doi.org/10.1002/adfm.201809036

Wang, Y., Wang, Q., Zhan, X., Wang, F., Safdar, M., & He, J. (2013). Visible light driven type II heterostructures and their enhanced photocatalysis properties: A review. *Nanoscale*, *5*(18), 8326. https://doi.org/10.1039/c3nr01577g

Wang, Y., Yao, L., Xu, L., Wu, W., Lin, W., Zheng, C., Feng, Y., & Gao, X. (2021). One-step solvothermal synthesis of hierarchical WO3 hollow microspheres with excellent NO gas

sensing properties. *Materials Letters*, *302*, 130460. https://doi.org/10.1016/j.matlet.2021.130460

Watts, John F., and John Wolstenholme. (2019). *An introduction to surface analysis by XPS and AES.* John Wiley & Sons.

Woodward, P. M., Sleight, A. W., & Vogt, T. (1997). Ferroelectric Tungsten Trioxide. *Journal of Solid State Chemistry*, *131*(1), 9–17. https://doi.org/10.1006/jssc.1997.7268

Wu, S., Li, Y., Chen, X., Liu, J., Gao, J., & Li, G. (2019). Fabrication of WO3·2H2O nanoplatelet powder by breakdown anodization. *Electrochemistry Communications*, *104*, 106479. https://doi.org/10.1016/j.elecom.2019.106479

Xiang, X., He, Z., Rao, J., Fan, Z., Wang, X., & Chen, Y. (2021). Applications of Ion Beam Irradiation in Multifunctional Oxide Thin Films: A Review. *ACS Applied Electronic Materials*, *3*(3), 1031–1042. https://doi.org/10.1021/acsaelm.0c01071

Xie, F. Y., Gong, L., Liu, X., Tao, Y. T., Zhang, W. H., Chen, S. H., Meng, H., & Chen, J. (2012). XPS studies on surface reduction of tungsten oxide nanowire film by Ar+ bombardment. *Journal of Electron Spectroscopy and Related Phenomena*, *185*(3–4), 112–118. https://doi.org/10.1016/j.elspec.2012.01.004

Xu, J., Liu, J.-B., Liu, B.-X., Wang, J., & Huang, B. (2019). Defect Engineering of Grain Boundaries in Lead-Free Halide Double Perovskites for Better Optoelectronic Performance. *Advanced Functional Materials*, *29*(8), 1805870. https://doi.org/10.1002/adfm.201805870

Yamashita, H., Harada, M., Misaka, J., Takeuchi, M., Neppolian, B., & Anpo, M. (2003). Photocatalytic degradation of organic compounds diluted in water using visible light-responsive metal ion-implanted TiO2 catalysts: Fe ion-implanted TiO2. *Catalysis Today*, *84*(3–4), 191–196. https://doi.org/10.1016/S0920-5861(03)00273-6

Yan, J., Wang, T., Wu, G., Dai, W., Guan, N., Li, L., & Gong, J. (2015). Tungsten Oxide Single Crystal Nanosheets for Enhanced Multichannel Solar Light Harvesting. *Advanced Materials*, *27*(9), 1580–1586. https://doi.org/10.1002/adma.201404792

Yanagishita, T., Masuda, T., & Masuda, H. (2022). Pretexturing and Anodization of W for Fabricating Ordered Anodic Porous WO $_3$. *Journal of The Electrochemical Society*, *169*(7), 072504. https://doi.org/10.1149/1945-7111/ac7ef3

Yang, B., Miao, P., & Cui, J. (2020). Characteristics of amorphous WO3 thin films as anode materials for lithium-ion batteries. *Journal of Materials Science: Materials in Electronics*, *31*(14), 11071–11076. https://doi.org/10.1007/s10854-020-03656-5

Yang, H., Sun, H., Li, Q., Li, P., Song, K., Song, B., & Wang, L. (2019). Structural, electronic, optical and lattice dynamic properties of the different WO3 phases: First-principle calculation. *Vacuum*, *164*, 411–420. https://doi.org/10.1016/j.vacuum.2019.03.053

Yang, M., Li, J., Ke, G., Liu, B., Dong, F., Yang, L., He, H., & Zhou, Y. (2021). WO3 homojunction photoanode: Integrating the advantages of WO3 different facets for efficient water oxidation. *Journal of Energy Chemistry*, *56*, 37–45. https://doi.org/10.1016/j.jechem.2020.07.059

Yoon, S., Jo, C., Noh, S. Y., Lee, C. W., Song, J. H., & Lee, J. (2011). Development of a high-performance anode for lithium ion batteries using novel ordered mesoporous tungsten oxide materials with high electrical conductivity. *Physical Chemistry Chemical Physics*, *13*(23), 11060. https://doi.org/10.1039/c1cp20940j

Yu, H., Wang, M., Yan, J., Dang, H., Zhu, H., Liu, Y., Wen, M., Li, G., & Wu, L. (2022). Complete mineralization of phenolic compounds in visible-light-driven photocatalytic ozonation with single-crystal WO3 nanosheets: Performance and mechanism investigation. *Journal of Hazardous Materials*, *433*, 128811. https://doi.org/10.1016/j.jhazmat.2022.128811

Zhang, B.-T., Liu, J., Yue, S., Teng, Y., Wang, Z., Li, X., Qu, S., & Wang, Z. (2017). Hot electron injection: An efficacious approach to charge LaCoO3 for improving the water splitting efficiency. *Applied Catalysis B: Environmental*, *219*, 432–438. https://doi.org/10.1016/j.apcatb.2017.07.033

Zhang, C., Van Overschelde, O., Boudiba, A., Snyders, R., Olivier, M.-G., & Debliquy, M. (2012). Improvement of sensing characteristics of radio-frequency sputtered tungsten oxide films

through surface modification by laser irradiation. *Materials Chemistry and Physics*, *133*(2–3), 588–591. https://doi.org/10.1016/j.matchemphys.2012.01.116

Zhang, D., Fan, Y., Li, G., Ma, Z., Wang, X., Cheng, Z., & Xu, J. (2019). Highly sensitive BTEX sensors based on hexagonal WO3 nanosheets. *Sensors and Actuators B: Chemical*, *293*, 23–30. https://doi.org/10.1016/j.snb.2019.04.110

Zhang, J., Zhang, P., Wang, T., & Gong, J. (2015). Monoclinic WO3 nanomultilayers with preferentially exposed (002) facets for photoelectrochemical water splitting. *Nano Energy*, *11*, 189–195. https://doi.org/10.1016/j.nanoen.2014.10.021

Zhang, T., Paulose, M., Neupane, R., Schaffer, L. A., Rana, D. B., Su, J., Guo, L., & Varghese, O. K. (2020). Nanoporous WO3 films synthesized by tuning anodization conditions for photoelectrochemical water oxidation. *Solar Energy Materials and Solar Cells*, *209*, 110472. https://doi.org/10.1016/j.solmat.2020.110472

Zhang, Y., Afzal, N., Pan, L., Zhang, X., & Zou, J. (2019). Structure-Activity Relationship of Defective Metal-Based Photocatalysts for Water Splitting: Experimental and Theoretical Perspectives. *Advanced Science*, *6*(10), 1900053. https://doi.org/10.1002/advs.201900053

Zhao, L., Xi, X., Liu, Y., Ma, L., & Nie, Z. (2020). Growth mechanism and visible-light-driven photocatalysis of organic solvent dependent WO3 and nonstoichiometric WO3-x nanostructures. *Journal of the Taiwan Institute of Chemical Engineers*, *115*, 339–347. https://doi.org/10.1016/j.jtice.2020.10.031

Zhao, Y., Zhang, X., Li, W., Li, Z., Zhang, H., Chen, M., Sun, W., Xiao, Y., Zhao, J., & Li, Y. (2022). High-performance electrochromic WO3 film driven by controllable crystalline structure and its all-solid-state device. *Solar Energy Materials and Solar Cells*, *237*, 111564. https://doi.org/10.1016/j.solmat.2021.111564

Zheng, G., Wang, J., Liu, H., Murugadoss, V., Zu, G., Che, H., Lai, C., Li, H., Ding, T., Gao, Q., & Guo, Z. (2019). Tungsten oxide nanostructures and nanocomposites for

photoelectrochemical water splitting. *Nanoscale*, *11*(41), 18968–18994. https://doi.org/10.1039/C9NR03474A

Zheng, H., Ou, J. Z., Strano, M. S., Kaner, R. B., Mitchell, A., & Kalantar-zadeh, K. (2011). Nanostructured Tungsten Oxide—Properties, Synthesis, and Applications. *Advanced Functional Materials*, *21*(12), 2175–2196. https://doi.org/10.1002/adfm.201002477

Zheng, X. D. (2019). The influence of ion implantation-induced oxygen vacancy on electrical conductivity of WO3 thin films. *Vacuum*, *165*, 46–50. https://doi.org/10.1016/j.vacuum.2019.04.004

Zheng, X., Wu, L., & Ren, F. (2021). Oxygen vacancy enhanced room temperature ferromagnetism in Ar+ ion irradiated WO3 films. *Ceramics International*, *47*(4), 5091–5098. https://doi.org/10.1016/j.ceramint.2020.10.087

Zheng, X.-D., Ren, F., Wu, H.-Y., Qin, W.-J., & Jiang, C.-Z. (2018). Formation of tungsten oxide nanowires by ion irradiation and vacuum annealing. *Nanotechnology*, *29*(15), 155301. https://doi.org/10.1088/1361-6528/aaac09

Zhou, J., Lin, S., Chen, Y., & Gaskov, A. M. (2017). Facile morphology control of WO3 nanostructure arrays with enhanced photoelectrochemical performance. *Applied Surface Science*, *403*, 274–281. https://doi.org/10.1016/j.apsusc.2017.01.209

Zhu, T., Chong, M. N., & Chan, E. S. (2014). Nanostructured Tungsten Trioxide Thin Films Synthesized for Photoelectrocatalytic Water Oxidation: A review. *ChemSusChem*, *7*(11), 2974–2997. https://doi.org/10.1002/cssc.201402089

Zych, M., Syrek, K., Pisarek, M., & Sulka, G. D. (2022a). Anodic WO3 layers sensitized with hematite operating under the visible light spectrum. *Journal of Power Sources*, *541*, 231656. https://doi.org/10.1016/j.jpowsour.2022.231656

Zych, M., Syrek, K., Pisarek, M., & Sulka, G. D. (2022b). Synthesis and characterization of anodic WO3 layers in situ doped with C, N during anodization. *Electrochimica Acta*, *411*, 140061. https://doi.org/10.1016/j.electacta.2022.140061

Appendix A.

A1. Table showing deconvoluted peak positions and area calculations of core W4f and O1s of two-layer non-irradiated and irradiated WO_3 samples of Chapter 5.

W4f and O1s		**Irradiated**		**Non-irradiated**	
		Peaks (eV)	**Area (a.u.)**	**Peaks (eV)**	**Area (a.u.)**
O^L		530.69	2687379.85	531.24	2724055.15
O^V		531.75	2530902.99	532.29	2473908.51
W^{6+}	4f5/2	38.1	60114.73	38.43	99712.23
W^{6+}	4f7/2	35.72	259365.47	36.18	318516.13
W^{5+}	4f5/2	37.25	476045.96	37.73	398839.99
W^{5+}	4f7/2	34.73	49563.30	35.15	63994.14
W^{x+}		33.79	379755.18	34.02	390656.57
W^{x+}		31.52	149246.60	31.75	168194.68
Area ratio	**W^{5+} /W^{6+}**	**1.64**		**1.1**	

A2. EDS elemental analysis of sample WO-7 of Chapter 6.

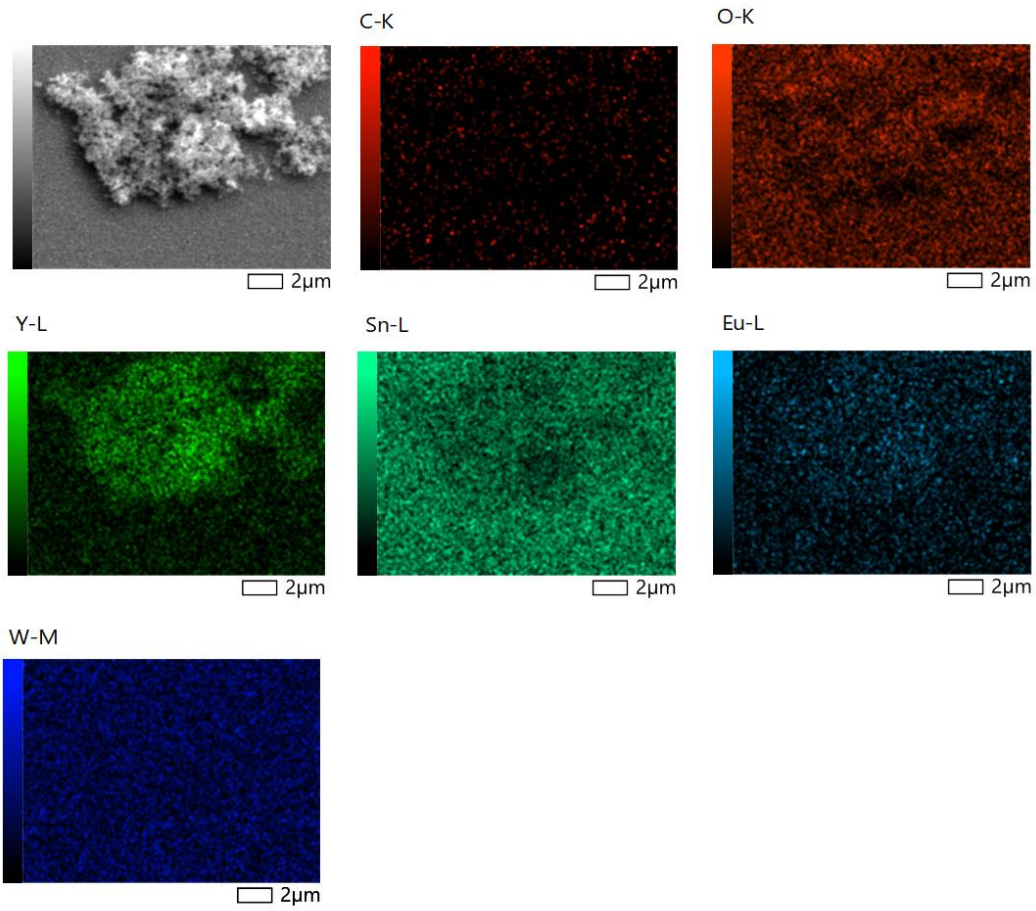

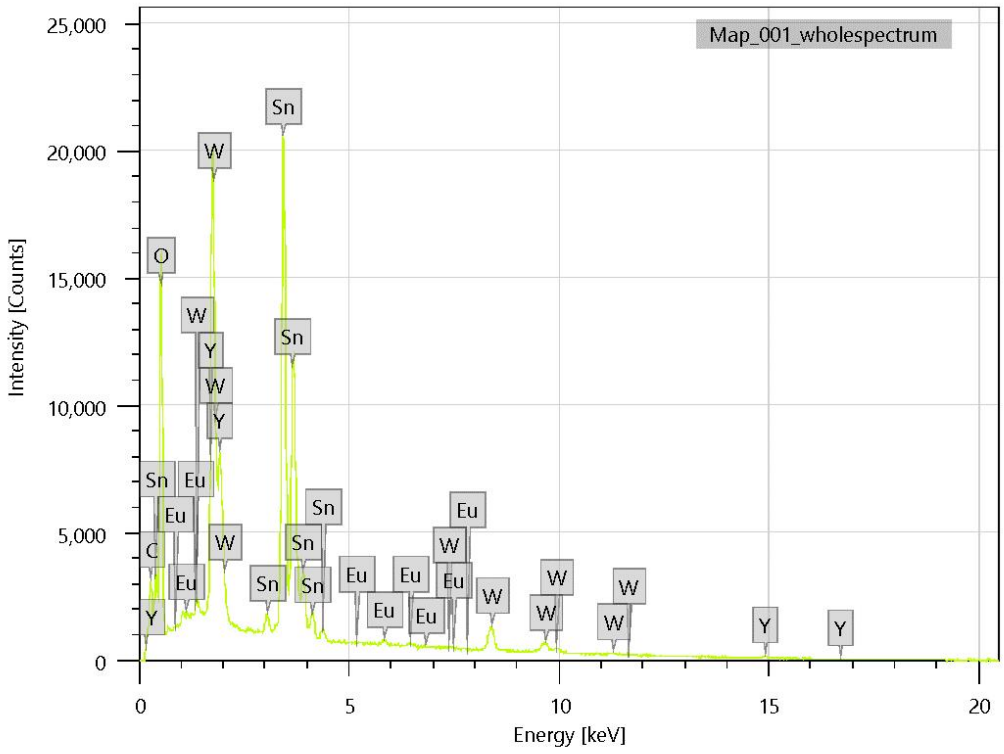

A3. Additional TEM images of sample WO-7 of Chapter 7. Dislocations are indicated with yellow arrow and grain boundaries indicated by green arrow.